



Delft University of Technology

Ducted wind turbines revisited

A computational study

Dighe, Vinit

DOI

[10.4233/uuid:56111690-faa8-4d98-9aba-d4a43fd5e160](https://doi.org/10.4233/uuid:56111690-faa8-4d98-9aba-d4a43fd5e160)

Publication date

2020

Document Version

Final published version

Citation (APA)

Dighe, V. (2020). *Ducted wind turbines revisited: A computational study*. [Dissertation (TU Delft), Delft University of Technology]. <https://doi.org/10.4233/uuid:56111690-faa8-4d98-9aba-d4a43fd5e160>

Important note

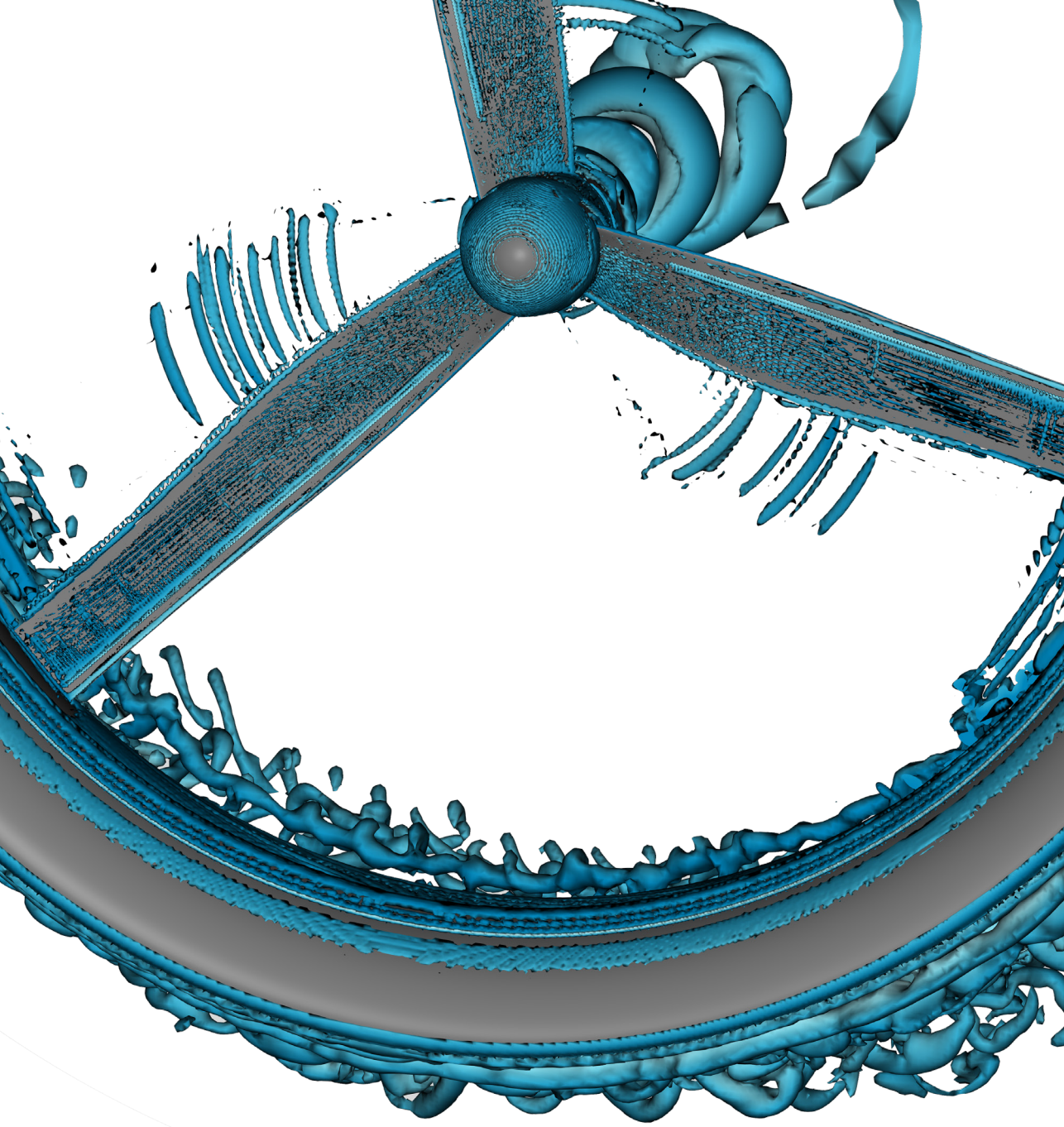
To cite this publication, please use the final published version (if applicable).
Please check the document version above.

Copyright

Other than for strictly personal use, it is not permitted to download, forward or distribute the text or part of it, without the consent of the author(s) and/or copyright holder(s), unless the work is under an open content license such as Creative Commons.

Takedown policy

Please contact us and provide details if you believe this document breaches copyrights.
We will remove access to the work immediately and investigate your claim.



DUCTED WIND TURBINES REVISITED

A computational study

VINIT V. DIGHE

Ducted wind turbines revisited

A computational study

Ducted wind turbines revisited

A computational study

Dissertation

for the purpose of obtaining a degree of doctor
at Delft University of Technology,
by the authority of the Rector Magnificus Prof. dr. ir. T. H. J. J. van der Hagen,
chair of the Board for Doctorates,
to be defended publicly on
Tuesday 26 May 2020 at 10:00 o'clock

by

Vinit V. Dighe

Master of Engineering (Hons) in Engineering Science,
The University of Auckland, New Zealand,
born in Mumbai, India.

This dissertation has been approved by the promotor.

Composition of the doctoral committee:

Rector Magnificus	chairperson
Prof. dr. G. J. W. van Bussel	Delft University of Technology, promotor
Dr. F. Avallone	Delft University of Technology, copromotor

Independent members:

Prof. dr. ing G. Eitelberg	Delft University of Technology
Prof. D. Wood	University of Calgary
Prof. M. O. Laver Hansen	Technical University of Denmark
Prof. K. Visser	Clarkson University
Dr. P. Jamieson	University of Strathclyde



Keywords: ducted wind turbine, CFD, aerodynamics, aeroacoustics

Printed by: ProefschriftMaken

Front & back: The front cover art captures the flow around a ducted wind turbine using LB-VLES simulation. The back cover presents a graphical illustration of wind energy illuminating our lives (by the author).

Copyright © 2020 by Vinit V. Dighe

ISBN 978-94-6380-816-3

An electronic version of this dissertation is available at

<http://repository.tudelft.nl/>.

*To my Aa**Ji**...*

Contents

List of Figures	ix
List of Tables	xi
Summary	xiii
Samenvatting	xv
1 Introduction	1
1.1 Historical development of DWT	4
1.2 Scope of the current study	8
1.3 Thesis outline	8
2 Numerical methodology	11
2.1 Aerodynamics of DWT	13
2.1.1 Flow past a bare wind turbine	13
2.1.2 Flow past a DWT	15
2.2 Computational fluid dynamics	20
2.2.1 Governing equations of fluid dynamics	20
2.2.2 Vortex panel method	23
2.2.3 RANS and URANS methods	26
2.2.4 LB-VLES method	31
3 Duct shape parametrization	37
3.1 Numerical validation	39
3.2 Duct shape parametrization	43
3.3 Aerodynamic performance coefficients	46
3.3.1 Duct force coefficient	47
3.3.2 Power coefficient	47
3.4 Flow-field analysis	47
3.5 Summary	50
4 Further augmentation techniques	55
4.1 Multi-element ducts	57
4.1.1 Numerical validation	58
4.1.2 Multi-element duct geometry	61
4.1.3 Duct force coefficient	62
4.1.4 Power augmentation	64
4.2 Gurney Flap	67
4.2.1 Experimental setup	67
4.2.2 Aerodynamic analysis	67

4.3	Summary	72
5	Effects of yawed inflow	75
5.1	Effects of yawed inflow: URANS study	77
5.1.1	Numerical validation	77
5.1.2	Aerodynamic performance	80
5.2	Effects of yawed inflow: LB-VLES study	84
5.2.1	Numerical setup	84
5.2.2	Numerical validation	85
5.2.3	Flow-field analysis	87
5.2.4	Aerodynamic performance	95
5.2.5	Noise estimation	96
5.3	Summary	99
6	Conclusions	101
6.1	On the effects of the shape of the duct	103
6.2	On the effects of further augmentation techniques	104
6.3	On the effects of yawed inflow	104
6.4	Recommendations	104
6.5	Final thought	106
	References	109
	Appendix A	117
	Appendix B	121
	Appendix C	123
	Curriculum Vitae	125
	List of Publications	127
	Acknowledgements	129

List of Figures

1.1	Schematic of mass flow augmentation through the DWT model . . .	6
1.2	Story-line of this thesis	9
2.1	Schematic of flow around an actuator disc model	14
2.2	Schematic of flow around a duct-actuator disc model	16
2.3	Schematic of flow around a duct-actuator disc model in yaw	18
2.4	Schematic of flow around a duct-actuator disc model with Gurney flap	19
2.5	Visual representation of fluid element in temporal space	21
2.6	Schematic for panel method representation	23
2.7	Panel distribution for duct shape	25
2.8	Computational domain for RANS and URANS simulations	30
2.9	Computational grid for RANS and URANS simulations	30
2.10	Representation of collision of fluid particles used in LBM approach	32
2.11	Computational domain used for the LB-VLES simulations	35
2.12	Volume resolution region used in LBM simulations	36
3.1	Experimental setup for DonQi DWT model at TU Delft	40
3.2	Representation of panel distribution	41
3.3	Mesh independence study	41
3.4	Comparison of computed velocity with experiments	42
3.5	Comparison of computed pressure distribution with experiments	42
3.6	Duct shape modification using CST parametrization	45
3.7	Schematic of duct profiles investigated	46
3.8	C_{TAD} vs. C_{TD} using panel method	48
3.9	C_{TAD} vs. C_{TD} using RANS method	48
3.10	C_{TAD} vs. C_P using panel method	49
3.11	C_{TAD} vs. C_P using RANS method	49
3.12	Flow field analysis using RANS results for D4 model	51
3.13	Flow field analysis using RANS results for D5 model	52
3.14	Flow field analysis using RANS results for D6 model	53
4.1	Flow around a multi-element DWT	58
4.2	Schematic of experimental setup	59
4.3	Velocity contours comparison for panel, RANS and URANS methods	60
4.4	Panel distribution for multi-element duct-AD model	61
4.5	Flap installation settings for multi-element duct-AD model	62
4.6	C_{TD} contours using panel method	63
4.7	C_{TD} contours using RANS method	63

4.8	Velocity contours using panel and RANS methods	65
4.9	C_p contours using panel method	66
4.10	C_p contours using panel method	66
4.11	Flow around DWT with Gurney Flap	67
4.12	Experimental setup of DonQi model with Gurney Flap	68
4.13	Velocity contours with 2% Gurney Flap	69
4.14	c_p comparison for DonQi without Gurney Flap	70
4.15	c_p comparison for DonQi with Gurney Flap	70
4.16	Center-line velocity comparison for DonQi without Gurney Flap	71
4.17	Radial plane velocity comparison for DonQi without Gurney Flap	71
5.1	Schematic and comparison of experimental findings with CFD	78
5.2	Velocity contours in y-z plane	78
5.3	Duct profiles used for the yaw study	80
5.4	α vs. C_{TD}	81
5.5	Velocity contours for DonQi model in yaw	82
5.6	Velocity contours for DonQi D5 model in yaw	83
5.7	α vs. C_p	84
5.8	Schematic of DWT models used for LB-VLES study	85
5.9	Front view of DonQi DWT model in experimental setup	86
5.10	Comparison of experimental c_p with LB-VLES results	87
5.11	Instantaneous flow-fields for DWT models in non-yawed condition	88
5.12	Instantaneous flow-fields for DWT models in yawed inflow condition	89
5.13	Velocity contours for DWT models in non-yawed condition	91
5.14	Velocity contours for DWT models in yawed inflow condition	92
5.15	Streamwise velocity contours for DonQi D5 DWT model in y-z plane	93
5.16	Radial velocity distribution for different inflow conditions	94
5.17	Schematic of microphone locations	96
5.18	OASPL for DWT models in different inflow conditions	97
5.19	Power Spectral Density vs. the Blade Passing Frequency	98
6.1	Artistic impression of Delft	107

List of Tables

- 3.1 Aerodynamic characteristics of duct profiles 46
- 4.1 Comparison of augmentation factor 59
- 4.2 Mesh independence study 62
- 4.3 Mesh independence study 68
- 5.1 Voxel statistics for LB-VLES study 86
- 5.2 Aerodynamic performance coefficients 96

Summary

Ducted Wind Turbines (DWTs) are one of the many concepts that have been proposed to improve the energy extraction from wind in comparison to bare wind turbines. In reviewing the DWT studies, investigations based on the combined use of theoretical, computational, and experimental techniques have been presented. Although indicated in these studies that the power output of wind turbines can be significantly increased by using surrounding ducts, the factors influencing this power increase, like the duct shape, augmentation add-on's and yawed inflow conditions, need further investigation. These topics have been addressed in this doctoral thesis.

The study presents a computational investigation of DWTs, employing two-dimensional and three-dimensional CFD simulations. To this intent, solutions obtained using panel, RANS, URANS and LB-VLES methods are shown. For reliable solution accuracy, verification and validation assessments are performed when possible. Through parametric investigation, it is found that the aerodynamic performance of the DWT can be improved by increasing the duct cross-section camber and a correct choice of turbine thrust force coefficient, whilst maintaining the same duct-exit-area ratio. The aerodynamic performance improvement for a DWT directly corresponds to the dimensionless duct thrust force coefficient. Flow analysis showed that flow separation when detected inside of the duct, reduces the duct thrust force coefficient and ultimately the aerodynamic performance of the DWT model.

In an effort to further improve on the aerodynamic performance of the DWT, the effect of multi-element ducts and Gurney flap on the existing DWT models are investigated. The aerodynamic performance improvement with multi-element ducts strongly depends on the installation settings of the secondary duct element with respect to the primary DWT geometry. On the other hand, a Gurney flap retrofitted at the trailing edge of the duct improves the aerodynamic performance of the DWT model by delaying inner duct wall flow separation, thus increasing the mass flow rate at the turbine.

Finally, the effects of yawed inflow condition on the aerodynamic and aeroacoustic performance of DWT models are studied in detail. The analysis showed that DWTs can demonstrate yaw insensitivity up to a specific yaw angle. The yaw insensitivity for the DWT model, however, strongly depends on the aerodynamic mutual interaction between the duct and turbine, which changes with the duct geometry, turbine configuration and yaw angle. While assessing the aeroacoustic performance of the DWT models, it is found that the DWT model

with highly cambered duct cross-section generates higher broadband noise levels, which results from the turbulent flow structures convecting along the surface of the duct.

Samenvatting

Een ommantelde windturbine (DWT) is één van de vele concepten met het doel de energie extractie uit de wind te vergroten ten opzichte van traditionele windturbines. In DWT studies worden combinaties van theoretische, numerieke en experimentele onderzoekstechnieken toegepast. Deze studies laten zien dat het geleverde vermogen van windturbines significant kan toenemen door het gebruik van een ringvormige mantel rond de rotor. Desondanks is er behoefte aan onderzoek naar de factoren die invloed hebben op deze toename zoals de vorm van de mantel, de diverse technieken gebruikt om vermogensvergroting te bevorderen en scheve instroomcondities. Deze factoren worden behandeld in dit proefschrift.

De studie omvat uitgebreid numeriek onderzoek naar DWT's, bestaande uit tweedimensionale en driedimensionale CFD simulaties. Door middel van panelencodes en RANS, URANS en LB-VLES simulaties zijn diverse resultaten verkregen. De nauwkeurigheid van deze voorspellingen zijn, waar mogelijk, geverifieerd en gevalideerd. Door middel van een parameterstudie is aangetoond dat de aerodynamische prestaties van de DWT verder verbeterd kunnen worden als de welving van het dwarsprofiel van de mantel wordt vergroot in combinatie met een correct gekozen stuwkrachtcoëfficiënt van de windturbine rotor. En dat bij gelijkblijvende uitlaatoppervlakte van de mantel. De verbetering van de aerodynamische prestatie van een DWT heeft een direct verband met de dimensieloze stuwkrachtcoëfficiënt van de turbine. Een uitgebreide stromingsanalyse toonde aan dat, wanneer stromingsloslating plaatsvindt binnen in de mantel, de stuwkrachtcoëfficiënt van de mantel reduceert en daarmee ook de aerodynamische prestatie van het onderzochte DWT model.

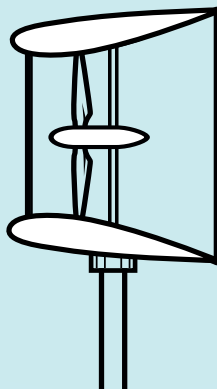
In een poging om de aerodynamische prestatie van de DWT nog verder te verbeteren, zijn de effecten onderzocht van een dwarsprofiel dat uit meerdere elementen bestaat, en het aanbrengen en het effect van een Gurney flap op de bestaande DWT modellen. De aerodynamische prestatie met multi-element profielen hangt sterk af van de positionering van het secundaire element ten opzichte van de primaire DWT geometrie. Een Gurney flap gepositioneerd aan de achterrand van de mantel kanaal daarentegen verbetert de aerodynamische prestaties van het DWT model door het uitstellen van de stromingsloslating langs de binnenste wand van de mantel. Dit resulteert in een toename van de massastroom in de turbine.

Ten slotte zijn de effecten van asymmetrische instroomcondities op de aerodynamische en aero-acoustische prestatie en DWT modellen in detail

bestudeerd. De analyse van deze resultaten wijst er op dat DWT's ongevoelig zijn voor scheve aanstroming tot een specifieke scheefstandshoek. De ongevoeligheid voor scheefstand van DWT modellen hangt sterk af van de aerodynamische interactie tussen de mantel en de turbine, welke op zijn beurt afhangt van de mantelgeometrie, de turbineconfiguratie en de scheefstandshoek. Tijdens de beoordeling van de aero-acoustische prestaties van de DWT modellen is naar voren gekomen dat het DWT model een zeer gewelfde doorsnede van de mantel meer breedbandige ruis genereert, als gevolg van de turbulente stromingsstructuren die langs de oppervlakte van het kanaal stromen.

1

Introduction



1.1	Historical development of DWT	4
1.2	Scope of the current study	8
1.3	Thesis outline	8

*If you can't explain it simply;
you don't understand it well enough.*

Albert Einstein

1

The global energy transition to renewable sources for electricity production is rising, and wind energy is a major force accommodating this transition [Barthelmie and Pryor, 2014]. The global wind power capacity quadrupled in less than a decade, reaching 597 Gigawatt by the end of 2018 compared to 120 Gigawatt in 2008 [Dupont et al., 2018]. During this period, the global weighted average capacity factor¹ increased from around 25% to 29% for onshore wind turbines and from 35% to 42% for offshore wind turbines [Dupont et al., 2018]. These accomplishments result from continuous innovation of wind turbine technology, support policies and the drive to address climate change.

The European Union (EU) is motivated to reduce greenhouse gas emissions to 80–95% below 1990 levels by 2050 [Fontaine et al., 2016]. To meet EU 2050 energy targets, exploitation of the full potential of wind energy is needed, not only offshore, but also onshore. A possible solution to increase the energy produced onshore is to use small wind turbines² that can be located close to urban environments [Fogaing et al., 2019]. Integration of wind turbines into urban environments is challenging. These challenges include but not limited³ to the following: lower wind speed, non-uniform inflow and larger turbulent⁴ fluctuations compared to the open fields. The lower wind speed and non-uniform inflow are due to the presence of buildings, trees and other surface discontinuities. The larger turbulent fluctuations result from wind interacting with the buildings and other obstacles. To address these challenges, design improvements of small wind turbines with respect to the existing technology is required.

A possible technological solution to extract wind energy in urban areas is represented by Ducted Wind Turbines (DWTs). DWTs are constituted of a turbine and a duct (also named as diffuser or shroud); the role of the latter is to increase

¹ As per the International Renewable Energy Agency (IRENA), the global weighted average capacity factor for wind turbines is the ratio of generated electrical energy output over a given period to the rated peak electrical energy output over that period.

² There are different definitions of small wind turbines, but the international small wind turbine design standard IEC 61400-2 defines them as wind turbines with a rotor-swept area less than 200 square metres

³ not limited is the term used to indicate other factors like technology integration, planning processes and economics.

⁴ In fluid dynamics, turbulence or turbulent flow is fluid motion characterized by chaotic changes in pressure and flow velocity.

the flow rate through the turbine relative to a bare wind turbine⁵ operating in the open atmosphere, thereby increasing the generated power [van Bussel, 2007]. This raised the current research questions:

Does the concept of DWT in fact increase the power output, and if so, by how much; what geometric form should it take; and finally, how will DWT perform under yawed inflow condition?

This thesis aims to answer these questions using a Computational Fluid Dynamics (CFD) approach. In this chapter, the motivation behind this thesis and the contents of the chapters that follow are presented. Moreover, this chapter is also intended to provide the reader a run-through of the development of the DWT concept from the very beginning.

1.1. Historical development of DWT

The first in-depth analysis of the DWT concept was performed by Lilley and Rainbird [1956] using one dimensional momentum⁶ and vortex⁷ theories. Their analysis suggested that a DWT can gain 65% more power output with respect to a bare wind turbine with the same diameter. They showed that, for a DWT, the gain in the power output is due to the increase in the axial velocity across the turbine and the reduction of turbine tip-losses.

Later, Kogan and Nissim [1962], Kogan and Seginer [1963], and Igra [1976, 1977, 1981], using one dimensional momentum theory and series of experiments, with the actuator disc (AD)⁸ models to represent the turbine, concluded that the augmentation factor, which is the ratio of the power output for a DWT to that of a bare wind turbine, is dependent on the generated thrust, duct exit-area-ratio (ratio of duct exit to duct nozzle) and the duct's static pressure recovery. They were the first to report that sub atmospheric pressure at the duct exit plane affects DWTs aerodynamic performance. In the second phase, a compact version of the initial duct was investigated. In order to increase the duct exit-area-ratio, three ring-shaped flaps were placed at the duct exit. With this setup, the overall length-to-diameter was nearly halved whilst maintaining the augmentation factor of approximately 2.8. The third phase witnessed a complete change in the duct and the flap geometry; the cross-section profiles were derived from NACA airfoils. Igra found that the addition of a airfoil-shaped flap improves the DWTs aerodynamic performance by 25% compared to a single duct configuration.

Following Igra's work, Gilbert and Foreman [1983] from Grumman Aerospace Corporation addressed the key issue for DWTs success: the cost reduction of the duct. The goal of the research was to reduce the size of the duct, thereby reducing

⁵In this thesis, bare wind turbine will refer to a horizontal axis wind turbine without a surrounding duct.

⁶In wind aerodynamics, momentum theory is a mathematical model to predict the performance of a wind turbine using conservation laws of fluid mechanics under some simplifying assumptions.

⁷Vortex method (for wind turbines) is a discrete representation of the wind vorticity field, which is built on the theory of ideal (potential) flow; it neglects the viscous effects.

⁸AD model represents a permeable disc that mimics the pressure drop across the wind turbine. AD models are typically used in the first stage design analysis of wind turbine models.

the manufacturing cost, whilst maintaining its performance. Grumman researchers identified the use of boundary layer⁹ control technique to manufacture compact ducts with a large exit-area-ratio. With this technique, flow separation delay is achieved by re-energizing the boundary layer flow along the inner walls of the duct, thus improving the overall performance. The optimal design for the baseline geometry was determined through a parametric study of exit-area-ratio, number of boundary layer slots, their position, size and geometry, as well as center-body configuration [Foreman and Gilbert, 1984]. The performance benefits, however, did not match the high costs incurred in the implementation of the flow control technology.

In the 1990s, Vortec, a company from New Zealand, attempted to commercialize a DWT design [Phillips et al., 1999]. The design was studied using wind tunnel experiments and CFD simulations. The project was abandoned when their seven meter prototype did not perform as well as expected. The Vortec turbine design required heavy support structures to withstand the high turbulent flow in storm conditions. Additionally, the power predicted during wind tunnel experiments and by the CFD simulations was significantly higher than that reached in the field test [Phillips et al., 2008]. The over-prediction during the wind tunnel experiments was attributed to a very high blockage correction factor¹⁰ used, while for the the CFD results, the discrepancy was attributed to the flow separation occurring inside the duct that was not captured computationally through the use of the chosen turbulence model.

Literature on DWT was sparse until 2000s when Hansen et al. [2000] studied the DWTs performance with a CFD-based method. They proved that the augmentation factor for a DWT is in fact proportional to the increased mass flow through the turbine, and not with the cube of the increased turbine plane velocity. There are more than one explanation why this occurs. The first explanation is that the duct forces an expansion of flow downstream of the turbine beyond what is attainable for a bare wind turbine. This provides a reduced pressure downstream of the turbine, thereby increasing the total mass flow through the turbine. A second explanation, as argued by de Vries [1979], is that if the sectional lift force of the duct is directed towards the turbine plane, then the associated circulation (see Figure 1.1) of the duct induces an increased mass flow through the turbine.

van Bussel [2007] developed an axial momentum theory (AMT) for DWT analogous with the AMT for bare wind turbines. He compared the results of his theory with the CFD predictions by Hansen et al. [2000], and also provided an extensive review and comparison with the experimental data available from Igra [1981], Gilbert and Foreman [1983], Phillips et al. [1999]. The conclusions of van Bussel were that the amount of energy extraction for a DWT is identical to that of a bare wind turbine, and a significant power augmentation for a DWT can be obtained with a strong reduction of the static pressure at the duct exit. Based on a

⁹In fluid mechanics, boundary layer refers to the layer of fluid in the immediate vicinity of a bounding surface where the effects of viscosity are significant.

¹⁰The blockage correction factor is the ratio of the frontal area of the experimental model to the cross section of the wind tunnel nozzle outlet.

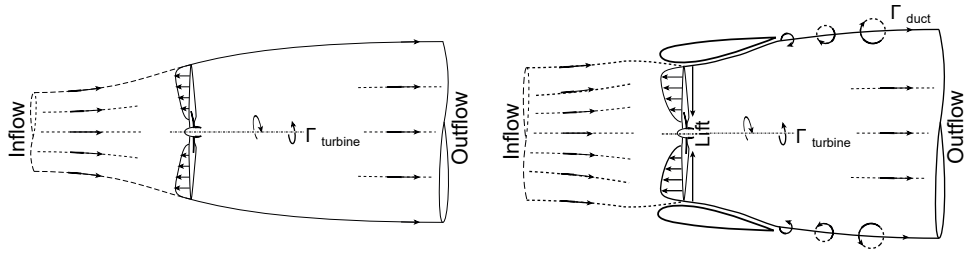


Figure 1.1: Schematic of mass flow augmentation through the DWT model. The bound circulation from the turbine blades and the duct surface is denoted by Γ .

similar approach, the model presented by Jamieson [2009] calculates an ideal zero-thrust induction factor at the turbine plane of an empty duct. He concluded that the amount of energy extraction for a DWT is linearly proportional to this induction factor. The models by van Bussel and Jamieson provide a useful extension of the standard AD theory to the ducted case, but do not take into account the viscous effects.

During the last decade, there is a renewed interest in the DWT research using CFD-based methods. Widnall [2009] proposed a potential-flow vortex method to analyse the incompressible flow field past a DWT. This method assumes a uniform change in the static and stagnation pressure across the AD under the influence of an axisymmetric duct represented using vortex panels. Afterwards, Bontempo and Manna [2013] developed a semi-analytical method to evaluate the performance of the DWT for a prescribed turbine load distribution and duct geometry. Unlike the potential-flow vortex method proposed by Widnall [2009], the semi-analytical method by Bontempo and Manna [2013] takes into account the wake¹¹ rotation and divergence. Due to the inviscid nature of the solutions, the methods can only handle ducts of general shapes without high camber and thickness distribution. In order to highlight the viscous effects on the DWT performance, Aranake et al. [2015] performed a three dimensional CFD analysis of a DWT configuration using Unsteady Reynolds Average Navier-Stokes (URANS) equations. They detected the unsteady flow behavior by looking at the vortex shedding on the inside of the duct and concluded that the flow separation is non-optimal for the overall DWT efficiency.

In reviewing research on DWTs to date, we may conclude that ducts can improve the power production of wind turbines in an unbounded flow. This is well established. Not disregarding the developments in the theoretical [Khamlaj and Rumpfkeil, 2018] and the experimental studies [Abe et al., 2005, Toshimitsu et al., 2008, Tang et al., 2018], CFD-based methods [Abe and Ohya, 2004, Grant et al., 2008, Wang and Chen, 2008, Chaudhari et al., 2013, Bontempo et al., 2014, Jafari and Kosasih, 2014, Roshan et al., 2015] clearly appears to be the most employed approach to analyse the performance of DWTs. The advances in CFD are closely related to the improvements in computer hardware; in particular, the storage and execution speed. In most of the mentioned literature, simulations were performed

¹¹Wake is the region of fluid that arises downstream of a wind turbine, where the wind speed is reduced.

by representing the turbine by a simplified AD model with an imposed pressure jump. Due to the complex aerodynamic interactions between the duct and the turbine, it is necessary to include aspects such as non-uniform blade loading, wake swirling and unsteady flow fluctuations for realizing the full potential benefits of the DWT concept in practice [van Bussel, 2015].

Since DWTs are installed in urban areas, they are subject to non-uniform flows caused by the presence of buildings or other surface discontinuities. Igra [1981] studied experimentally the effects of yaw on the aerodynamic performance of DWTs. Eight geometries were investigated using the duct-AD approach. The eight configurations differed in the duct exit-area-ratio. It was found that when the duct exit-area-ratio was less than 4.5, little or no difference in the power output was measured up to a yaw angle of $\pm 30^\circ$ while any further increase in yaw resulted in power reduction. On the other hand, when the duct exit-area-ratio was higher than 4.5, the generated power decreased even for small yaw angles. Igra explained that the yaw insensitivity, for the low duct exit-area-ratio configurations, is due to the lift force increase by the annular duct cross-section. The author did not provide any further explanation to clarify the physics behind performance drop for large duct exit-area-ratio. Later, researchers from Grumman Aerospace tested a bare wind turbine and two DWT models (named as Baseline DAWT and DAWT 45) varying the yaw angle up to 40° with increments of 10° [Gilbert and Foreman, 1983]. Both the Baseline DAWT and DAWT 45 models showed a negligible change in the power up to a yaw angle of 30° , and a drastic reduction in power at yaw angle of 40° . Surprisingly, the bare rotor also demonstrated no dependence on the yaw angle up to 30° . They stated that this was due to the long center-body configuration, similar in all the three designs, that helped channeling the incoming flow towards the upwind turbine blade and at the same time shielding the downwind turbine blade, thus offering an insensitivity to yaw. However, in a follow up paper [Foreman and Gilbert, 1983] they stated that these yaw tests were inconclusive whether the yaw insensitivity was due to the center-body effect or the duct geometry itself. More recently, Phillips et al. [2008] combined experimental and numerical analysis to study DWTs under yawed flow. They concluded that the power increase for a DWT in yawed flow can only be achieved with a slotted duct design, with the added mass flow of air through the slot increasing the boundary layer flow control and preventing flow separation over the suction side (inner surface) of the duct under severe yaw misalignment. The above literature, due to the contrasting nature of the conclusions, lacks clarity on the aerodynamics of DWTs in yawed flow, and particularly on the effect of the duct geometry on the aerodynamic performances. For this reason, the aerodynamic performance of DWTs in yawed inflow condition must be characterized.

In comparison to the aerodynamic studies on DWTs, literature on DWT aeroacoustics was sparse until recent times when the researchers from TU Delft published a series of studies on DWTs aeroacoustic performance using CFD-based methods and experiments [Anselmi, 2017, Avallone et al., 2020, Küçüksöğüt, 2019]. DWT installations in urban areas are also subject to noise regulations laid

by the local authorities. Having said that, there is a strong need to characterize the aeroacoustic performance of DWT depending on its geometrical parameters and operating conditions. This thesis work aims to make a contribution to this.

1.2. Scope of the current study

The current investigation will make use of CFD-based methods for the aerodynamic and aeroacoustics analysis of DWTs, while addressing the three main objectives.

Firstly, the aerodynamic flow-field around a DWT is highly sensitive to the geometric variation of the duct shape and the rotor configuration. Ducts with different geometric features have been used for the DWT models investigated up till now [Igra, 1977, Gilbert and Foreman, 1983, Abe and Ohya, 2004, Jafari and Kosasih, 2014, Kanya and Visser, 2018]. A detailed characterization of the aerodynamic flow-field based on the duct geometry and rotor configuration is missing in the literature. Through parametric investigations, the effects of the thickness and the camber of the duct cross-section, and the rotor loading on the aerodynamic performance of DWT will be studied in detail.

The second objective relates to the improvement of the aerodynamic performance of an existing DWT model using flow control techniques. This is studied to a very limited extent in the past [Igra, 1977, Gilbert and Foreman, 1983, Abe and Ohya, 2004]. The process can be achieved by re-energizing the flow outside the duct in order to increase the mass flow through the turbine. To this aim, the effects of multi-element ducts and Gurney flap on the aerodynamic performance of an existing DWT models will be investigated.

Finally, having attained a significant advancement in the DWT design, the question remains as to what are the effects of yawed inflow condition on DWTs aerodynamic performance. To this aim, unsteady simulations for the selected DWT models will be performed in two-dimensional and at full spatial scale. Moreover, the effects of yawed inflow condition on DWTs aeroacoustic performance will be studied.

1.3. Thesis outline

In this thesis, the work is divided into four core chapters that can, in one way or another, be read independently. Nevertheless, they are part of a bigger storyline, illustrated in Figure 1.2.

Chapter 2 is essential to develop a theoretical basis for understanding the DWT concept. Furthermore, the mathematical description of the numerical methods used is reported in this chapter. The effects of the duct cross-section geometry and the value of turbine loading on the aerodynamic performance of DWTs are discussed in chapter 3. Chapter 4 explores the augmentation techniques, more specifically multi-element ducts and Gurney flap, to further improve on the aerodynamic performance of the existing DWT models. Chapter 5 studies the aerodynamic and aeroacoustic performance of DWT models in yawed inflow condition. Finally, the most important findings and recommendations for future research are summarized in chapter 6.

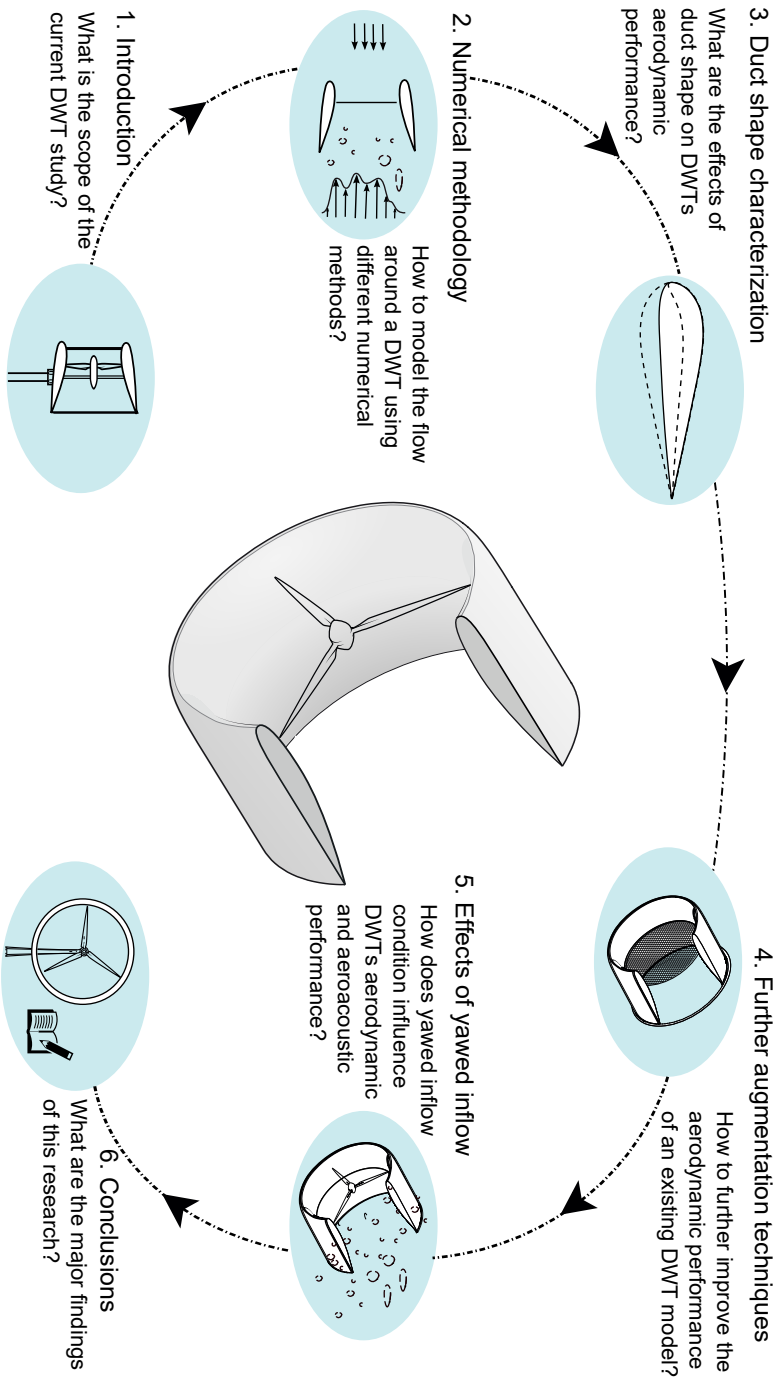
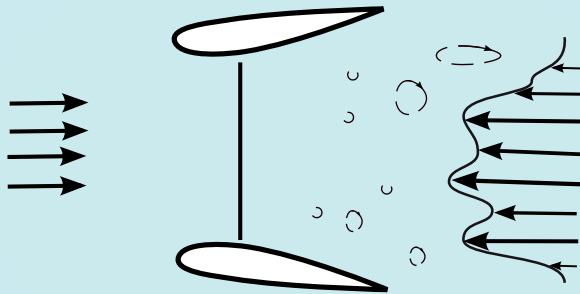


Figure 1.2: Story-line of this thesis highlighting the main research questions.

2

Numerical methodology



2.1	Aerodynamics of DWT	13
	Flow past a bare wind turbine	13
	Flow past a DWT	15
2.2	Computational fluid dynamics	20
	Governing equations of fluid dynamics	20
	Vortex panel method	23
	RANS and URANS methods	26
	LB-VLES method	31

*The science of today
is the technology of tomorrow.*

Edward Teller

The existing works in the context of DWTs was drawn in chapter 1. Based on the reviewed literature, the aerodynamic performance of DWT is dependent upon its geometric parameters, flow characteristics and operating conditions. To ensure that this thesis is approachable for readers from various scientific backgrounds, a theoretical basis to model the flow past a DWT is presented. This chapter is divided into two main sections. The equations governing the aerodynamic performance of the DWT are presented in section 2.1. Then, section 2.2 provides the mathematical description of the CFD-based methods before delving into the applications presented in chapters 3, 4 and 5.

2.1. Aerodynamics of DWT

Inspired by the seminal work of Betz [1920], the discussion starts with the flow past a bare wind turbine, following which, mathematical expressions for the flow past a DWT are reported. In addition to this, the mathematical expressions, including the effects of yawed inflow condition and the thrust augmenting devices, affecting DWTs aerodynamic performance, are presented.

2.1.1. Flow past a bare wind turbine

Based on the classical actuator disc (AD) theory by Rankine [1865] and Froude [1889], the flow past a bare wind turbine is represented substituting the rotor with an AD of infinitesimal width. Assuming uniform incompressible flow in steady-state conditions, it is possible to calculate the thrust and power extracted by the AD. Figure 2.1 shows a stream-tube model¹ constructed around the AD, along with the free-stream velocity U_∞ and the velocity in the wake U_w . As the AD extracts momentum and energy from the wind, the wind speed inside the stream-tube slows down. Consequently, the stream-tube expands in the wake region in order to satisfy mass conservation. The AD exerts a static pressure jump Δp_{AD} across the AD surface area S_{AD} to produce a uniform² thrust force T_{AD} . Then, the non-dimensional thrust force coefficient is:

¹The stream-tube model for AD analysis assumes a control volume in which the boundaries are the surface walls of a stream tube, and two cross-sections upstream and downstream of the AD.

²The assumption of uniform thrust force distribution across the AD radial plane is employed; the assumption is simplified and typically used in the first stage of design analysis of wind turbine models.

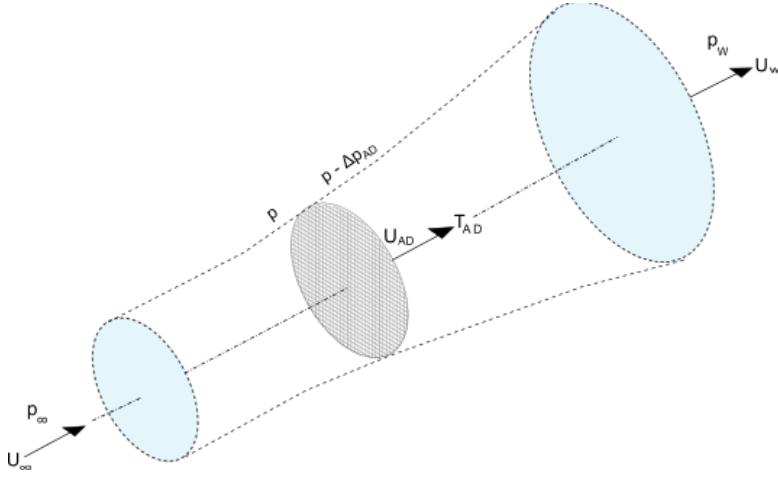


Figure 2.1: Schematic of flow around an actuator disc model using stream-tube showing pressure, velocity and thrust force at different locations.

$$C_{TAD} = \frac{T_{AD}}{\frac{1}{2}\rho U_{\infty}^2 S_{AD}} = \frac{\int_{S_{AD}} -\Delta p_{AD} dS_{AD}}{\frac{1}{2}\rho U_{\infty}^2}, \quad (2.1)$$

where ρ is the fluid density at standard sea-level conditions. Negative value of static pressure jump, Δp_{AD} , indicates that the energy is extracted (wind turbine mode)³.

Applying Bernoulli's theorem⁴ across the stream-tube volume leads to:

$$\begin{cases} p_{\infty} + \frac{1}{2}\rho U_{\infty}^2 &= p + \frac{1}{2}\rho U_{AD}^2 \\ (p - \Delta p_{AD}) + \frac{1}{2}\rho U_{AD}^2 &= p_w + \frac{1}{2}\rho U_w^2 \end{cases}, \quad (2.2)$$

where p and $p - \Delta p_{AD}$ are the static pressure upstream and downstream stations of the AD, respectively. Δp_{AD} is the pressure drop across the actuator disk. In equation 2.2, the subscript ∞ is adopted for pressure and velocities evaluated in the free-stream region far upstream from the AD, while subscript w is adopted for pressure and velocities evaluated in the wake region far downstream from the AD. The sum of the above expressions return:

$$-\Delta p_{AD} = \frac{1}{2}\rho U_{\infty}^2 \left(1 - \frac{U_w^2}{U_{\infty}^2}\right). \quad (2.3)$$

³The AD model is also employed to model the flow past a propeller, then the static pressure jump Δp is positive.

⁴Bernoulli's theorem states that, in incompressible state, fluids have to speed up when they reach a narrow constricted section in order to maintain a constant volume flow rate.

Rewriting equation 2.1 making use of equation 2.3, the thrust force coefficient for the bare AD reads:

$$C_{TAD} = 1 - \left(\frac{U_W}{U_\infty} \right)^2. \quad (2.4)$$

Although the assumption of uniform thrust force distribution T_{AD} along the AD surface is employed, the free-stream velocity at the AD plane cannot be regarded as radially uniform [Bontempo and Manna, 2013]. In order to account for the non-uniform flow along the AD surface, the mean AD velocity is defined by integrating the differential terms for the local axial velocity U_x in the streamwise direction along the AD radial plane:

$$U_{AD} = \frac{1}{S_{AD}} \int_{S_{AD}} U_x dS. \quad (2.5)$$

Then, the power coefficient for the bare AD, represented by subscript o , is given by:

$$C_{P_o} = \frac{P_o}{\frac{1}{2} \rho U_\infty^3 S_{AD}} = \frac{U_{AD}}{U_\infty} C_{TAD}. \quad (2.6)$$

The power coefficient is a dimensionless measure of the efficiency of a bare wind turbine in extracting the energy content in a wind stream. Betz, Lanchester and Joukowski established a theoretical maximum efficiency for a bare wind turbine equal to $\frac{16}{27}$, corresponding to the the Betz-Lanchester-Joukowski optimal AD thrust force coefficient of $\frac{8}{9}$ [van Kuik, 2007].

2.1.2. Flow past a DWT

A similar approach can be taken to represent the flow past a DWT using the same assumptions of an AD. The difference, however, is that the AD is surrounded by an airfoil cross-section⁴ duct as shown in Figure 2.2. As a result of the duct cross-section, the stream-tube model changes from tubular shape (as in Figure 2.1) to an hourglass shape. In presence of duct, additional thrust force exerted by the duct on the flow, or vice-versa⁵, appears. Then, the total thrust force T is the vectorial sum of the AD thrust force T_{AD} , and of the axial thrust force exerted by the duct T_D , written as:

$$T = T_{AD} + T_D. \quad (2.7)$$

⁴Based on the DWT literature, ducts can vary in cross-section. However, for the scope of the current study, airfoil cross-section ducts are investigated.

⁵Unless stated otherwise, force exerted by the flow on the duct.

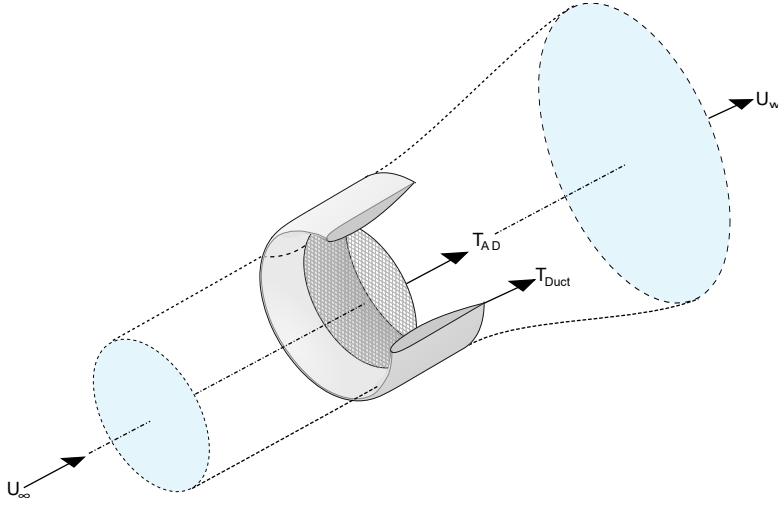


Figure 2.2: Schematic of flow around a duct-actuator disc model using stream-tube.

The total thrust force coefficient is then defined as:

$$C_T = C_{T_{AD}} + C_{T_D}, \quad (2.8)$$

where $C_{T_D} = \frac{T_D}{\frac{1}{2}\rho U_\infty^2 S_{AD}}$ ⁶. To highlight the relative contribution of the duct thrust force T_D and the AD thrust force T_{AD} on to the total thrust force T , a dimensionless thrust factor τ is introduced:

$$\tau = \frac{T_D}{T_{AD}} = \frac{C_{T_D}}{C_{T_{AD}}}, \quad (2.9)$$

so that the total thrust force coefficient in equation 2.8 can be written as:

$$C_T = (1 + \tau)C_{T_{AD}}. \quad (2.10)$$

Alternatively, from the momentum theory [Froude, 1889], the total thrust T can be expressed as:

$$T = T_{AD} + T_D = \dot{m}(U_\infty - U_w) \Rightarrow C_T = C_{T_{AD}} + C_{T_D} = 2 \frac{U_{AD}}{U_\infty} \left(1 - \frac{U_w}{U_\infty}\right), \quad (2.11)$$

⁶Note that the duct thrust coefficient is normalized with the AD area to facilitate direct addition to the AD thrust coefficient for calculating the total thrust coefficient.

where $\dot{m} = \rho U_{AD} S_{AD}$ is the mass flow processed, when calculated at the AD station. Combining equations 2.4 and 2.11, the normalized velocity at the AD station for a duct-AD configuration reads:

$$\frac{U_{AD}}{U_{\infty}} = \frac{1}{2} \left(1 + \frac{U_W}{U_{\infty}} \right) + \frac{C_{TD}}{2 \left(1 - \frac{U_W}{U_{\infty}} \right)}. \quad (2.12)$$

The normalized velocity, as in equation 2.12, can be expressed as a function of C_{TAD} and C_{TD} combining equations 2.4, 2.10 and 2.11:

$$\frac{U_{AD}}{U_{\infty}} = \frac{1 + \tau}{2} \left(1 + \sqrt{1 - C_{TAD}} \right). \quad (2.13)$$

With the help of equations 2.6 and 2.13, the power coefficient of the duct-AD model considering S_{AD} as the reference area can be written as:

$$C_P = \frac{1 + \tau}{2} \left(1 + \sqrt{1 - C_{TAD}} \right) C_{TAD}. \quad (2.14)$$

In equation 2.14, C_P indicates the power coefficient of the duct-AD model. The above relation is also valid for a simple AD model setting $\tau = 0$. Then, equation 2.6 can be alternatively expressed as:

$$C_{P_o} = \frac{1}{2} \left(1 + \sqrt{1 - C_{TAD}} \right) C_{TAD}. \quad (2.15)$$

It is worth mentioning that some studies adopt a different definition for power coefficient in which the reference area is taken at the duct exit section [van Bussel, 2007]. As a result, the power coefficient obtained is smaller than the one calculated using equation 2.14. So that, the difference in the power coefficients can be expressed as:

$$\frac{C_P}{C_{P_{exit}}} = \frac{S_{AD}}{S_{exit}}. \quad (2.16)$$

Equations 2.14 and 2.15 can be used to evaluate the contribution of the duct through a power augmentation factor r [Igra, 1976]:

$$r = \frac{C_P}{C_{P_o}} = 1 + \tau = 1 + \frac{C_{TD}}{C_{TAD}}. \quad (2.17)$$

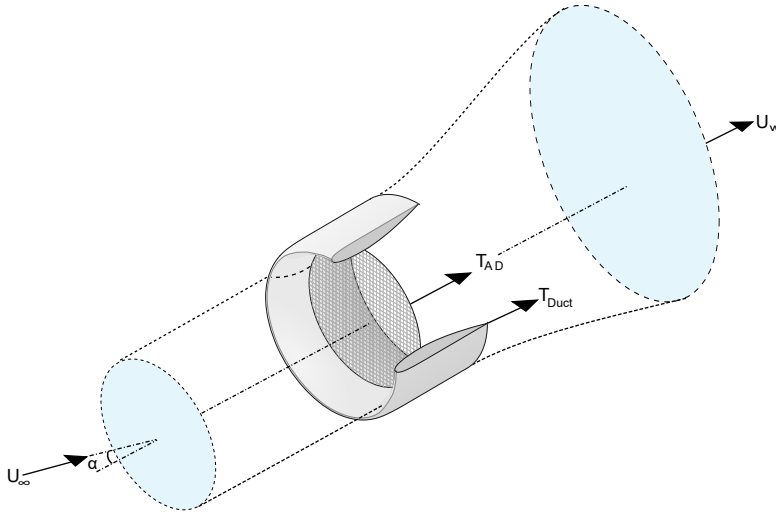


Figure 2.3: Schematic of flow around a duct-actuator disc model subject to yawed inflow condition.

Equation 2.17 states that τ for a duct-AD model is proportional to the ratio between the duct thrust force coefficient C_{TD} and the AD thrust force coefficient C_{TAD} . Thus, if $\tau > 0$, then a higher power coefficient can be obtained for a DWT in comparison to a bare wind turbine with the same turbine diameter.

The power coefficient expression for a DWT challenges the well-known Betz-Lanchester-Joukowski limit of $\frac{16}{27}$ for maximum power coefficient obtainable for bare wind turbine [van Bussel, 2007]. This should not appear like a surprising result, since, the mass flow of air swallowed by a DWT is greater due to the additional thrust force offered by the duct. Thus, in practice, if the duct thrust force is positive, then a higher power coefficient can be obtained for a DWT in comparison to a bare wind turbine with the same turbine diameter [Bontempo et al., 2014]

The above relations can be extended to include the effects of yawed inflow condition on the aerodynamic performance of a DWT. The effect of yaw angle α on the duct-AD stream-tube model is shown in Figure 2.3, where the flow convecting downstream is skewed in the direction normal to α . In contrast to the bare AD, which indicates a drop in C_{P_0} as a function of α [Glauert, 1926], $C_{P_{yaw}}$ for a duct-AD model depends on the mutual interaction between the duct and the AD, an interaction that changes the value of τ for different duct geometry, AD loading and inflow condition. Here, the subscript *yaw* has been adopted to indicate the quantities for the duct-AD model evaluated under yawed inflow condition. If C_{TAD} is assumed to be constant, recall from equation 2.14, then the following relations for a duct-AD model in yawed inflow condition can be employed:

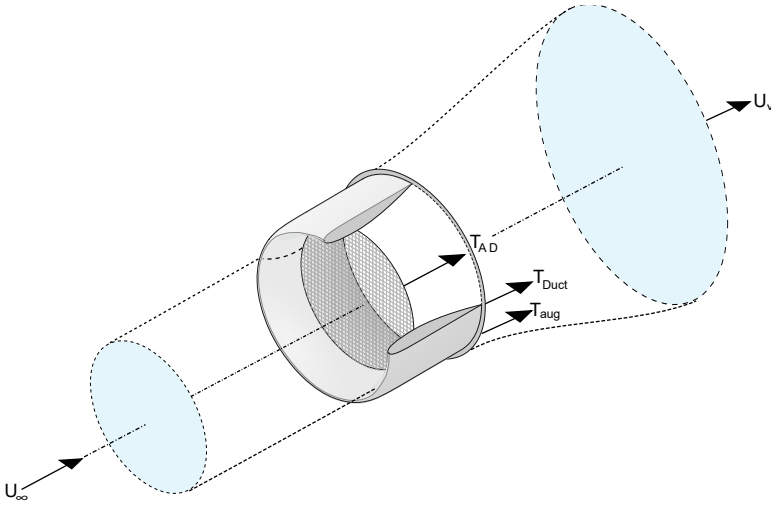


Figure 2.4: Schematic of flow around a duct-actuator disc model with a Gurney flap attached to the duct's trailing edge.

$$\begin{aligned} C_{P_{yaw}} &< C_P \quad \text{if} \quad \tau_{yaw} < \tau, \\ C_{P_{yaw}} &> C_P \quad \text{if} \quad \tau_{yaw} > \tau. \end{aligned} \quad (2.18)$$

Unlike bare wind turbines, DWTs can offer reduced sensitivity to yaw as a result of the channelling effect created by the duct. Igra [1981] and Gilbert and Foreman [1983] noted little or no variation in the DWTs aerodynamic performance for yaw angles up to $\pm 15^\circ$ and $\pm 10^\circ$, respectively.

The axial thrust force of the duct T_D , and ultimately the value of τ , can be increased further with the application of thrust augmenting devices⁸. In Figure 2.4, the thrust augmenting device is represented by a gurney flap located at the duct exit. The addition of gurney flap increases the duct downwind force for the existing duct-AD model. Then, the total thrust force, as in equation 2.7, can be re-written as:

$$T = T_{AD} + T_D + T_{aug} = T_{AD} + T_D^*, \quad (2.19)$$

where T_{aug} is the thrust force produced by the thrust augmenting device (here it is the gurney flap) and T_D^* is the resultant thrust force exerted by the duct supplemented with thrust augmenting device. In the above equation, and the

⁸Thrust augmenting devices refer, but not limited to gurney flaps, multi-element ducts, flange and vortex generators.

equations to follow, superscript $*$ is adopted to group together the quantities evaluated for the duct and the thrust augmenting device, so that they could be treated as a unit. Having said that, the thrust factor τ in equation 2.9 becomes:

$$\tau^* = \frac{T_D^*}{T_{AD}} = \frac{C_{TD}^*}{C_{TAD}}, \quad (2.20)$$

The contribution of τ^* to the power coefficient is expressed by combining equations 2.14 and 2.20:

$$C_P^* = \frac{1 + \tau^*}{2} \left(1 + \sqrt{1 - C_{TAD}}\right) C_{TAD}. \quad (2.21)$$

Then, the power augmentation factor r is given by:

$$r = \frac{C_P^*}{C_{P_o}} = 1 + \tau^* = 1 + \frac{C_{TD}^*}{C_{TAD}}. \quad (2.22)$$

The power coefficient of an existing DWT model can be increased with the combined use of duct and thrust augmenting device/devices. The power augmentation factor, however, depends on the geometry and the placement of the thrust augmenting device/devices with respect to the existing DWT configuration.

2.2. Computational fluid dynamics

What is CFD? To answer this question, recall the fundamental principles of fluid dynamics: mass, momentum and total energy are always conserved in a closed system⁹. These fundamental principles can be written in terms of mathematical equations, which in their most generic form are either integral equations or partial differential equations. CFD is a technique of replacing the integrals or the partial derivatives in these equations with discretized arithmetic forms, which are then solved to obtain the macroscopic properties¹⁰ of fluid at discrete points in the flow-field that are variable in time and/or space.

2.2.1. Governing equations of fluid dynamics

The governing equations of fluid dynamics expresses the conservation laws of mass, momentum and energy in a continuum state¹¹. There are two widely used models

⁹Basically, what comes in, must also go out somewhere else.

¹⁰for e.g. mass, pressure, time, velocity etc.

¹¹modelling fluid in continuum state assumes control volume elements distributed within a finite region of the flow. The fundamental principles of fluid dynamics are applied to the volume element as a whole, and ignoring the changes occurring inside the control volume elements (see Figure 2.5).

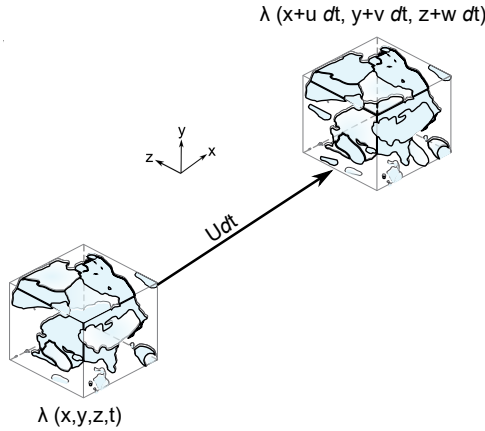


Figure 2.5: A visual representation of infinitesimal fluid element moving with the velocity U in spatial and temporal space. Under the continuum assumption, macroscopic flow variables are defined at volume elements (bounding box) and are averaged values of the molecular dynamics.

to represent the conservation equations: the Euler model and the Navier-Stokes-Fourier model.

For notational convenience in the equations to follow, it is imperative to explain the physical meaning of total derivative $\frac{D}{Dt}$ and divergence operator ∇ . Let's suppose that we have a generic fluid variable $\lambda(x, y, z, t)$. From the total time derivative of λ in Cartesian coordinates, we have:

$$\frac{D\lambda}{Dt} = \frac{d\lambda}{dt} + u \frac{d\lambda}{dx} + v \frac{d\lambda}{dy} + w \frac{d\lambda}{dz} = \frac{d\lambda}{dt} + (\nabla \cdot \lambda U). \quad (2.23)$$

$\frac{D\lambda}{Dt}$ represents the time rate of change of λ following a moving fluid element (see Figure 2.5) as it moves through a three dimensional space. $\frac{d\lambda}{dt}$ is the local derivative, which measures the time rate of change of λ at a fixed point; while $(\nabla \cdot U)$ is the convective derivative, which is physically the time rate of change due to the movement of the fluid element in a Cartesian space. The Cartesian coordinate system, with axis lines x , y and z , shown in Figure 2.5, is adopted throughout this thesis.

The Euler model is named after a Swiss mathematician Leonhard Euler, who first derived the mass, momentum and energy conservation equations [Anderson and Wendt, 1995]:

The Euler equations (Non-conservation form)

$$\frac{D\rho}{Dt} + \rho \nabla \cdot U = 0, \quad (2.24)$$

$$\rho \frac{DU}{Dt} = -\nabla p + F, \quad (2.25)$$

$$\rho \frac{De}{Dt} = -p \nabla \cdot U, \quad (2.26)$$

where $\rho = \rho(x, y, z, t)$ is the fluid density, $U = U(u, v, w, t)$ is the fluid velocity, $p = p(x, y, z, t)$ is the pressure and $e = e(x, y, z, t)$ is the internal energy variable in three dimensional space (x, y, z) and time t .

The continuity equation, as in equation 2.24, describes the time rate of change of fluid density at a point and the net mass flux at that point.

The momentum equation, as in equation 2.25, describes the rate of change of velocity under the influence external body force F and pressure differences as it moves through the fluid.

The energy equation, as in equation 2.26, describes how the internal energy is either decreased by expansion (the fluid particle pushing on the surrounding particles), or increased by compression (the surrounding particles pushing on the fluid particle).

The equations of the Navier-Stokes-Fourier model are very similar to the equations of the Euler model. The difference is the addition of the deviatoric stress tensor τ to take into account the effects of internal friction (viscosity) and heat flux in the fluid.

The Navier-Stokes-Fourier equations (Non-conservation form)

$$\frac{D\rho}{Dt} + \rho \nabla \cdot U = 0, \quad (2.27)$$

$$\rho \frac{DU}{Dt} = -\nabla p + \nabla \tau + F, \quad (2.28)$$

$$\rho \frac{De}{Dt} = (-p + \tau) \nabla \cdot U - \nabla q, \quad (2.29)$$

In the momentum equation 2.28, the deviatoric stress tensor term τ represents the friction between the different fluid elements moving with different velocities. τ also occurs in the energy equation 2.29, representing the energy increase due to frictional heating. The heat flux q represents the heat flow between the adjacent fluid particles with different temperatures.

The deviatoric stress tensor τ for incompressible viscous fluid, which was first determined by Stokes [1880], can be stated as:

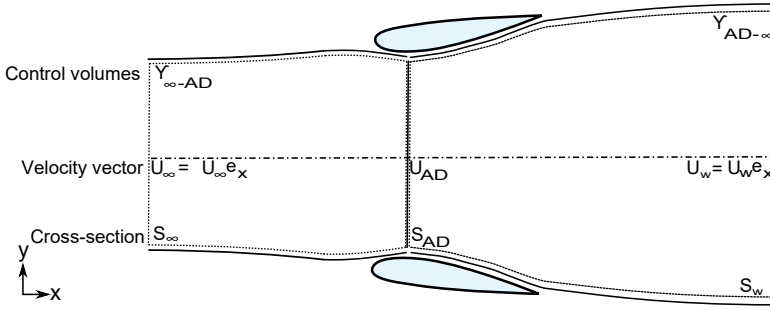


Figure 2.6: Two-dimensional panel method setup and the partition of control volumes for a duct-AD flow model.

$$\tau = \mu(\nabla U + (\nabla \bar{U})), \quad (2.30)$$

and the heat flux is assumed to be given by Fourier's law,

$$q = -\kappa \nabla T. \quad (2.31)$$

Equations 2.30 and 2.31 include the diagonal element of the tensor $\nabla \bar{U}$, dynamic shear viscosity μ , fluid temperature T and thermal conductivity κ (this is treated as constant).

Many, if not most, problems in CFD reduce to solving the above equations with appropriate boundary conditions, approximations and equations of state. The physical origins of the numerical methods listed hereinafter assumes the accurateness of the governing fluid dynamics equations, unless proved otherwise¹².

2.2.2. Vortex panel method

A two dimensional potential flow vortex panel method is used to model the steady, incompressible and inviscid flow around a DWT following the deduction of [de Vries \[1979\]](#). A detailed description of the method is given by [De Oliveira Andrade \[2019\]](#). The study setup is represented in Figure 2.6. The governing flow equations are the steady incompressible variant¹³ of the Euler equations 2.24 and 2.25, given by¹⁴:

$$\rho \nabla \cdot U = 0, \quad (2.32)$$

¹² Navier–Stokes existence and smoothness solution is the subject of the Millennium Prize problem

¹³ Incompressible flow returns the total derivative of density to zero

¹⁴ The process is considered isothermal, and neglects the thermal effects, thus energy conservation equation is not stated.

$$\rho \frac{DU}{Dt} = -\nabla p + F. \quad (2.33)$$

It consists of a free-stream with an AD representing the turbine, and a symmetric pair of duct surfaces. The center-line is aligned with the free-stream direction x . The AD surface exerts a uniform distribution of forces along the radial plane, while duct surfaces can be represented as arbitrary, and potentially, disjoint shapes. The AD exerts no azimuthal forces. The choice ensures the absence of wake swirl, so that the static enthalpy h in the wake region returns to free-stream values ($h = h_\infty = h_W$) as the distance to the AD and the duct locations grows down-stream.

The derivation of aerodynamic coefficients for the duct-AD model starts by integrating the continuity equation (2.32) to obtain mass balance:

$$\left. \begin{aligned} \int \rho \nabla \cdot U dY_{\infty-AD} &= \dot{m}_\infty - \dot{m}_{AD} = 0 \\ \int \rho \nabla \cdot U dY_{AD-W} &= \dot{m}_{AD} - \dot{m}_W = 0 \end{aligned} \right\} \Rightarrow \rho S_\infty U_\infty = \rho S_{AD} U_{AD} = \rho S_W U_W, \quad (2.34)$$

where $Y_{\infty-AD}$ and Y_{AD-W} are the control volumes that partition the stream-tube.

The momentum balance is achieved by integrating the momentum equation (2.33) in the free-stream direction e_x over the control volume $Y_{\infty-W} = (Y_{\infty-AD} \cup Y_{AD-W})$:

$$\int \left(\rho \frac{DU}{Dt} \right) \cdot e_x dY_{\infty-W} = - \int (\rho \nabla h) \cdot e_x dY_{\infty-W} + \int (F) \cdot e_x dY_{\infty-W}. \quad (2.35)$$

where pressure force is represented in terms of static enthalpy ($h = \frac{p}{\rho}$). The total derivative term is easily integrated into an algebraic expression:

$$\int \left(\rho \frac{DU}{Dt} \right) \cdot e_x dY_{\infty-W} = \rho S_W U_W^2 - \rho S_\infty U_\infty^2 = \rho S_{AD} U_{AD} (U_W - U_\infty), \quad (2.36)$$

where S_∞ , S_{AD} and S_W are used to define stream-tube areas at inlet, AD and outlet respectively.

The external force term F is integrated by denoting the AD loading density per unit area as:

$$\int (F) \cdot e_x dY_{\infty-W} = T_{AD} = -dp \times S_{AD}. \quad (2.37)$$

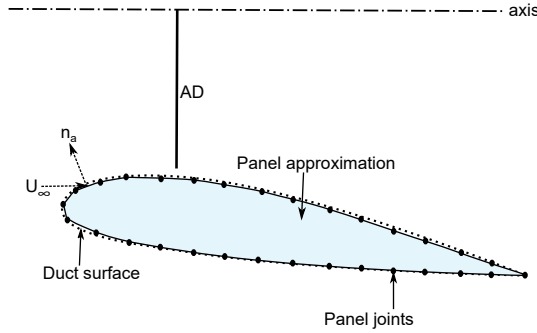


Figure 2.7: Panel distribution to approximate the duct shape for pressure force calculation.

The static enthalpy integral in equation 2.35 does not return a closed algebraic expression. The expression is denoted by T_D and corresponds to the free-stream component of total thrust force exerted by the duct surfaces. The simplification is executed with a few algebraic steps. In essence, the duct surfaces are defined using a distribution of vortex panels (see Figure 2.7) with the local slope tangential to the duct surface such as to reproduce the desired duct cross-section shape¹⁵. A uniform distribution of vorticity on the duct panels is assigned by assuming the Kutta condition. The Kutta condition enforces the flow to leave the sharp trailing edge of the duct smoothly. The sum of all pressure forces, acting in the normal direction n_a on the duct panels, can be written as:

$$\begin{aligned} T_D &= \oint (\rho \nabla h) \cdot e_x dY_{\infty-W} = \oint (\nabla p) \cdot e_x dY_{\infty-W} \\ &= \oint (pn_a) \cdot e_x dY_{\infty-W} \end{aligned} \quad (2.38)$$

Rewriting equation 2.35 using equations 2.36-2.38 transforms momentum conservation into an expression describing the total thrust force T_{AD} exerted by the AD:

$$T_{AD} = \rho S_{AD} U_{AD} (U_W - U_{\infty}) + T_D. \quad (2.39)$$

Total AD thrust force can also be expressed in terms of energy conservation. This is done by integrating Crocco's equation [Greitzer et al., 2007] along the stream-tube:

$$T_{AD} = \frac{1}{2} \rho S_{AD} (U_W^2 - U_{\infty}^2) + \rho S_{AD} (h_W - h_{\infty}) = \frac{1}{2} \rho S_{AD} (U_W^2 - U_{\infty}^2). \quad (2.40)$$

¹⁵A detailed description of the panel strength distribution involves several intermediate steps that were deemed outside the scope of the current contribution. For a detailed description, the reader can refer to De Oliveira Andrade [2019]

Reworking equation 2.39 with equation 2.40 gives the average flow across the AD surface:

$$U_{AD} = \frac{1}{2}(U_W + U_\infty) + \frac{T_D}{\rho S_{AD}(U_W - U_\infty)}. \quad (2.41)$$

The rate of energy transfer across the AD surface corresponds to the product of mass flow \dot{m} with the total enthalpy jump ($h_W - h_\infty$), which is written from the power perspective:

$$P = \dot{m}(h_W - h_\infty) = \frac{1}{2}\rho S_{AD}U_{AD}(U_W^2 - U_\infty^2). \quad (2.42)$$

To highlight the relative contribution of the duct thrust force T_D , it is convenient to recast equations 2.34-2.41 into dimensionless terms:

$$C_{TAD} = \frac{T_{AD}}{\frac{1}{2}\rho S_{AD}U_\infty^2}, \quad C_{TD} = \frac{T_D}{\frac{1}{2}\rho S_{AD}U_\infty^2}, \quad U_{AD} = \frac{1}{2}(U_W + 1) + \frac{1}{2} \frac{1}{U_W - 1} C_{TD}. \quad (2.43)$$

Power coefficient C_P for a duct-AD model is then expressed as:

$$C_P = \frac{P}{\frac{1}{2}\rho S_{AD}U_\infty^3} = U_{AD}(U_W^2 - 1) = \frac{1}{2}(U_W + 1)((U_W^2 - 1) + C_{TD}). \quad (2.44)$$

A typical converged panel method solution is obtained in roughly 0.05 hour on a multi-core work-station desktop computer. Numerical predictions of C_P , as in equation 2.14, are obtained for different values of C_{TAD} and C_{TD} (different duct cross-section shapes) by post-processing reconstructed velocity fields.

The vortex panel method represents a simplification of flow physics and does not consider flow separation even for larger pressure gradients on the duct surfaces. Due to the non-linear nature of solutions obtained, the panel method, in any case, should be considered to obtain higher accuracy in comparison to the analytical models used for the analysis of DWT. The vortex panel method is particularly appealing for repeated analysis design arrangements due to its short execution time.

2.2.3. RANS and URANS methods

A commercial CFD solver ANSYS Fluent is used for complete viscous solutions of steady and unsteady incompressible flow around a DWT using a simplified duct-AD model. The solver employs a finite-volume approach to solve the governing equations for continuity (equation 2.27) and momentum (equation 2.28) based on

the knowledge of flow turbulence¹⁶ to give approximate solutions to the Navier Stokes equations. In this method, the computational domain is discretized into mesh elements of control volumes using co-located mesh approach. To this aim, ANSYS ICEM is used for the mesh generation. The governing flow equations in their integral form for each mesh elements are reconstructed into set of algebraic equations to determine flow variables like velocities, pressure, temperature and conserved¹⁷ scalars. Linearization of the discrete set of equations is used to update the values of dependent variables on the individual mesh elements; integrating further yields the overall solution for the computational domain under consideration.

RANS and URANS equations

Reynolds [1895] introduced the Reynolds-averaged Navier-Stokes (RANS) equations which rely on the time averaging concept. In order to transform the Navier-Stokes equations (equations 2.28 and 2.29) into RANS equations, it is assumed that a time varying quantity (for example velocity U) is split into two parts, a mean component and a fluctuating component. The splitting operator is generally termed as Reynolds decomposition. As an example, the Reynolds decomposition of U is:

$$U(\chi, t) = \bar{U} + U'(\chi, t) \quad (2.45)$$

where $\chi = (x, y, z)$ is the position vector. Applying the Reynolds decomposition to the velocity and pressure followed by time-averaging (indicated by an over-bar) yields the RANS equations for incompressible fluid:

RANS equations

$$\rho \nabla \cdot \bar{U} = 0 \quad (2.46)$$

$$\rho \frac{D\bar{U}}{Dt} = \nabla \bar{p} + \nabla \bar{\tau} + \bar{F}. \quad (2.47)$$

The URANS are similar to RANS equations as in equation 2.47, except for the local derivative $\frac{d}{dt}$ (recall from equation 2.23) is retained during computation. Then the URANS equations are given by:

¹⁶As stated by G.I.Taylor: "Turbulence is an irregular motion which in general makes its appearance in fluids, gaseous or liquid, when they flow past solid surfaces or even when neighboring streams of the same fluid flow past or over one another."

¹⁷A conserved scalar concept simplifies the flow field solution by treating the scalar values as constant along each trajectory of the fluid system.

URANS equations

$$\rho \nabla \cdot \bar{\mathbf{U}} = 0, \quad (2.48)$$

$$\rho \frac{D\langle \bar{\mathbf{U}} \rangle}{Dt} = \nabla \bar{p} + \nabla \bar{\tau} + \bar{\mathbf{F}}, \quad (2.49)$$

where $\langle \bar{\mathbf{U}} \rangle$ represents the time resolved mean velocity.

The left hand side of equations 2.47 and 2.49 represents the change in mean momentum of fluid element due to the unsteadiness in the mean flow. This change is balanced by the mean pressure field, mean viscous stresses and the mean body force, generally referred to as Reynolds stress. This nonlinear Reynolds stress term requires additional modelling to produce a closed system of equations, and has led to the creation of many different turbulence models [Pope, 2001].

Second-order closure model

Second-order closure model refers to a class of RANS models for which the second moments (Reynolds stress term) are modelled, usually as solutions to partial differential equations. Detailed discussions on turbulence closure in CFD can be found in Pope [2001]. In the following, the second-order closure model used in the present study is discussed.

The second-order closure model chosen for this study is the $k - \omega$ shear-stress transport (SST) model, an adaptation of the $k - \omega$ model introduced by Wilcox [1998]. Apsley and Leschziner [2000] investigated the ability of various second-order closure models to predict separated flows in a duct and compared them to experimental data. $k - \omega$ SST model returns better predictions than the other second-order closure models with regards to approximating the reversed flow in the velocity profiles of the duct. Moreover, Shives and Crawford [2012] investigated the application of different closure models for modelling ducted turbine flows. It was concluded that $k - \omega$ SST model outperforms the other first and second-order closure models. The first variable, k , determines the level of kinetic energy in the turbulence. The second variable, ω , determines the specific dissipation rate of the turbulent kinetic energy. The $k - \omega$ SST model, written in conservation form, is given by the following:

$$\frac{d}{dt}(\rho k) + \frac{d}{dx_i}(\rho k u_i) = \frac{d}{dx_j} \left(\Gamma_k \frac{dk}{dx_j} \right) + G_k - Y_k + S_k, \quad (2.50)$$

$$\frac{d}{dt}(\rho \omega) + \frac{d}{dx_i}(\rho \omega u_i) + \frac{d}{dx_j} \left(\Gamma_\omega \frac{d\omega}{dx_j} \right) + G_\omega - Y_\omega + D_\omega + S_\omega, \quad (2.51)$$

where G_k is the turbulence kinetic energy due to mean velocity gradients. G_ω represents the generation of ω calculated using the Reynolds number correction. Γ_k and Γ_ω represent the effective diffusivity of k and ω respectively. Y_k and Y_ω

are the dissipation of k and ω due to turbulence calculated using the equations for turbulence dissipation. S_k and S_ω are user defined source terms, and D_ω represents the cross-diffusion term.

The physical interpretation of the terms in $k - \omega$ SST model, as presented in [ANSYS Fluent 18.0 \[2018\]](#), can be summarized as follows. The turbulent energy k is given by:

$$k = \frac{3}{2}(UI)^2. \quad (2.52)$$

The turbulence intensity I gives the level of turbulence and can be estimated from an empirical correlation written as:

$$I = 0.16(Re)^{-1/8}, \quad (2.53)$$

where Re is the flow Reynolds number. The specific turbulent dissipation rate ω is given by:

$$\omega = C_\mu \frac{\frac{-1}{4}\sqrt{k}}{l}, \quad (2.54)$$

where C_μ is the turbulence model constant and takes the value of 0.09. The turbulence length scale l is a physical quantity describing the size of eddies containing energy, in turbulent flows, given by:

$$l = 0.07L, \quad (2.55)$$

where L is regarded as the duct chord length for the specific duct-AD model.

Computational settings and parameters

The 2D computational domain is shown in Figure 2.8. The domain distances are normalized with the duct chord length c . The distances from the AD location to domain inlet and outlet are $12c$ and $24c$ respectively. Boundary conditions are: a uniform velocity inlet, zero gauge static pressure outlet and no-slip walls for duct surface [[Zhao and Yang, 2010](#), [Hafien and Mbarek, 2019](#)]. Symmetry boundary condition is applied to the center-line axis. The influence of AD is included into the domain as an additional body force, \bar{F} in equations 2.47 and 2.49, acting opposite to the direction of flow. This is achieved using a reverse fan boundary condition bearing finite thickness t . For a uniform thrust loading, the force term \bar{F} is given by:

$$\bar{F} = \frac{C_{TAD}\rho U_\infty^2}{2t}, \quad (2.56)$$

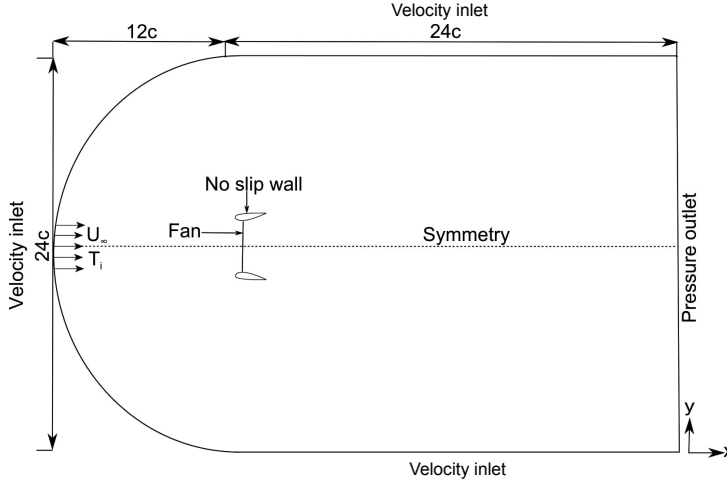


Figure 2.8: Computational domain showing the boundary conditions employed. The length are indicated in terms of duct chord length c (representative, not to scale).

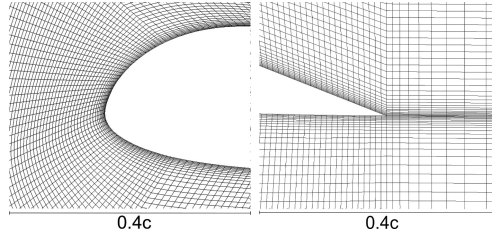


Figure 2.9: Two-dimensional computational grid along the leading and trailing edge of the duct used for RANS and URANS simulations.

where C_{TAD} is calculated from a semi-empirical relation of pressure drop curve and the velocity at the AD obtained from wind tunnel experiments [Tang et al., 2016]. The fluid is air with fluid density $\rho = 1.276 \frac{kg}{m^3}$ and dynamic viscosity $\mu = 1.722 \times 10^{-5} Pa \cdot s$. Values of free-stream velocity U_∞ and turbulence intensity I are chosen for consistency with the wind tunnel experiments.

The computational mesh consists of quadrilateral cells with maximum y^+ value of 1 on the duct walls. y^+ is the non-dimensional distance from the wall to the first node from the wall. A C-mesh structured zonal approach is chosen, which proved advantageous in the case of a curved boundary (see Figure 2.9). The C-shaped loop terminates in the wake region. Bi-geometric bunching law is applied along the edges of the curved boundary, which generates a finer mesh resolution along the duct's leading and trailing edge regions. The recommendation of ANSYS Fluent 18.0 [2018] states to use at least 10 mesh cells within the boundary layer in order to capture the boundary layer flow using this strategy. There are typically 20 or

more mesh cells employed within the boundary layer for the simulations presented. A close-up view of the boundary layer mesh is reported in Figure 2.9. To ensure mesh independent solutions, the effect of mesh refinement on the values of C_{TD} is studied; this will be detailed in the relevant sections of the following chapters.

For modelling incompressible flow, a pressure-based approach is chosen of the two solvers (a pressure-based solver and a density-based solver) available in ANSYS Fluent. The pressure-based solver was developed for low-speed incompressible flows, while the density-based solver for high-speed compressible flows. The pressure-based solver employs the projection method, which solves the pressure correction equation by combining the continuity and the momentum equation [ANSYS Fluent 18.0, 2018]. The pressure equation is obtained from the continuity and momentum equations in such a way that the velocity field, corrected by pressure, satisfies continuity. An iterative process is involved to solve the governing equations, which are coupled and non-linear, until the solution converges.

The RANS solutions are obtained using the coupled algorithm [Wilcox, 1998]; it offers robustness and faster convergence for steady solutions in comparison to the segregated solution schemes. As recommended [ANSYS Fluent 18.0, 2018], PISO algorithm is used for URANS calculations. A least-squares cell-based method is used to evaluate the pressure gradient, with continuity and momentum equations solved using a second order upwind differential scheme. The convergence criteria is set to 10^{-6} for all the residuals.

A typical converged RANS and URANS solution with approximately 0.1 million mesh elements is obtained in roughly 0.4 and 1 hour respectively on a multi-core work-station desktop computer. Flow variables are extracted by considering conservation of linear momentum across the control volume of the fluid. The resultant thrust force over the surface of the duct and the AD is calculated as the integral of pressure and viscous forces.

RANS and URANS methods are considerably more reliable and accurate than the panel method solution, but at the expense of computational cost. RANS and URANS solutions show better accuracy, when the viscous effects and possibly flow separation at the duct surface occur.

2.2.4. LB-VLES method

A Lattice Boltzmann method using Very Large Eddy Simulation model is chosen to take into account the eddies²¹ in the flow above a threshold length scale defined during RANS and URANS computations (see equation 2.55). Eddies smaller than this threshold are modelled using a sub-grid scale (SGS) model. The approach builds on the conceptualization of Richardson [1992]:

Big whorls have little whorls,
which feed on their velocity;

²¹There is no precise definition of *eddy* in fluid dynamics. The author prefers the description by Kundu et al. [2008]: "Identifiable structures in a turbulent flow, particularly those that spin are called eddies."

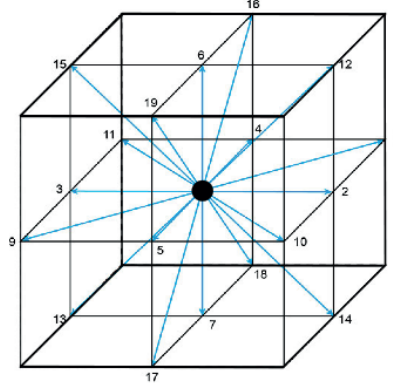


Figure 2.10: A schematic representation of collision of fluid particles within a control volume. LBM approach incorporates simplified kinetic models to capture mesoscopic molecular dynamics, yet the averaged macroscopic quantities satisfy the desired conservation equations.

And little whorls have lesser whorls,
And so on to viscosity.

This reflects the physical notion that the turbulence energy spectrum may be viewed as an energy cascade in which the energy is transferred from large length scale turbulence through to smaller scale eddies, and then dissipated by the fluid viscosity as heat. A commercial LB-VLES solver 3DS Simulia PowerFLOW is used. The software solves the discrete Lattice Boltzmann (LB) equations for a finite number of directions. The lattice Boltzmann equations, which evolved from its predecessor lattice-gas automata, incorporates simplified kinetic models to capture the flow physics at mesoscopic²² scale (see Figure 2.10), yet the averaged quantities satisfy the desired macroscopic flow equations. The description of the LB equations will somewhat be limited to the scope of the current study. For a detailed description, the reader can refer to [Chen and Doolen \[1998a\]](#) and [Succi \[2001\]](#). For an incompressible fluid in isothermal conditions, the governing equations of fluid dynamics (continuity and momentum equations) can be derived from the LB equations, see [Appendix A](#). Statistically, the LB equations describe the particle motion at a position x in the i -th direction at time t . The macroscopic flow variables, such as density and velocity, are determined by taking summation over the set of discrete directions of the particle distribution function given by:

$$\Omega(f) = U \cdot \nabla f + \frac{F}{\rho} \cdot \nabla_U f + \frac{df}{dt}. \quad (2.57)$$

The particle distribution function $\Omega(f)$ is solved by means of the Boltzmann equation on a mesh composed of cubic volumetric elements (voxels) and surface

²²Mesoscopic scale, in the context of fluid dynamics, addresses the fluid variables when the macroscopic scale is miniaturized.

elements (surfels), known as lattice. A Very Large Eddy Simulation (VLES) model is implemented to take into account the unresolved scales of turbulence. A two equation $k - \epsilon$ Renormalization Group (RNG) is used to compute the turbulent relaxation time that is added to the viscous relaxation time. This VLES methodology is implemented as standard turbulence model in 3DS Simulia PowerFLOW.

The physical time step Δt , corresponding to a Courant–Friedrichs–Lewy (CFL) number [Courant et al., 1967] of 1 in the finest mesh refined regions is 7.27×10^{-7} s. A pressure-gradient-extended wall-model (PGE-WM) is used to approximate the no-slip boundary condition on solid walls [Teixeira, 1998]. The model is based on the extension of the generalized law-of-the-wall model [Launder and Sharma, 1974] to take into account the effect of pressure gradient, given by the following analytical expression:

$$u^+ = \frac{1}{\kappa} \ln\left(\frac{y^+}{A}\right) + B, \quad (2.58)$$

where u^+ and y^+ are the boundary-layer velocity and the non-dimensional wall distance, respectively. $\kappa = 0.41$ is the von Karman constant and $B = 5.2$ is the log-law constant. A is a function of pressure gradient. It captures the physical consequence that the velocity profile slows down and so expands, due to the presence of the pressure gradient, at least at the early stage of the development. The expression for A is:

$$A = 1 + \frac{f \left| \frac{dp}{ds} \right|}{\tau_w}, \quad \hat{u}_s \cdot \frac{dp}{ds} = 0, \quad (2.59)$$

$$A = 1, \quad \text{otherwise.} \quad (2.60)$$

In the equations, τ_w is the wall shear stress, $\frac{dp}{ds}$ is the stream-wise pressure gradient, \hat{u}_s is the unit vector of the local slip velocity and f is the length scale equal to the size the unresolved near-wall region. These equations are iteratively solved from the first mesh cell close to the wall in order to specify the boundary conditions of the turbulence model. For this purpose, a slip algorithm [Chen and Doolen, 1998b], obtained as generalization of a bounce-back and specular reflection process, is used.

The transient nature of the LB-VLES solutions allow the extraction of acoustic pressure in the near-field up to a cut-off frequency corresponding to approximately 15 voxels per acoustic wavelength. The acoustic pressure in the far-field is computed by using the Ffowcs Williams-Hawkings (FWH) analogy.²³ The formulation 1A developed by Farassat and Succi [1980] with advanced-time

²³For the reader's convenience, acoustic variables important for the current discussion are included in Appendix B

marching scheme, extended to a convective wave equation, is used in this study. Unsteady pressure is recorded on the surface mesh provided by the transient LBM simulations. In PowerFLOW, this surface mesh can be defined either as a solid surface corresponding to a solid body or as a permeable wall surface surrounding the solid body. In the present study, the solid formulation is chosen with pressure information sampled as an integral quantity. Due to the solid surface methodology adopted, acoustic dipole sources L_i are the only source term for the current analogy [Curle, 1955], defined as:

$$L_i = (p - p_0)n_i \quad (2.61)$$

where $p - p_0$ is the fluctuating pressure on the solid surface and n_i is the surface normal in the i th direction. To determine the far field pressure spectra, the distance between the observer (x_1) and the source position (y_1), R needs to be defined. It can be written as:

$$R = \frac{-M_0(x_1 - y_1) + R^*}{\beta^2}, \quad (2.62)$$

with

$$R^* = \sqrt{(x_1 - y_1)^2 + \beta^2[(x_2 - y_2)^2 + (x_3 - y_3)^2]}, \quad (2.63)$$

and

$$\beta = \sqrt{1 - M_0^2}. \quad (2.64)$$

M_0 is the Mach number, which is a dimensionless quantity representing the ratio of flow velocity U_∞ to the local speed of sound c . R represents the effective acoustic distance, different from the geometric distance between the source and the observer, in terms of time delay between emission and reception. The unit radiation vector is then given by:

$$\hat{R} = \left[\frac{-M_0 R^* + (x_1 - y_1)}{\beta^2 R}, \frac{x_2 - y_2}{R}, \frac{x_3 - y_3}{R} \right]. \quad (2.65)$$

Having defined the source term L_i and the observer distance from the source R , the following integral relation is solved [Brès et al., 2010]:

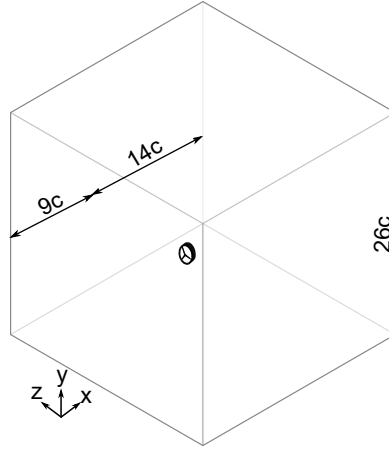


Figure 2.11: Computational domain used for the LB-VLES simulations. The length are indicated in terms of duct chord length c (representative, not to scale).

$$\begin{aligned}
 4\pi p'_{aa}(x, t) = & \frac{1}{a_0} \int_{g=0} \left[\frac{L_i \hat{R}_i}{R(1 - M_i \hat{R}_i)^2} \right]_{ret} dS \\
 & + \int_{g=0} \left[\frac{L_i \hat{R}_i - L_i M_i}{R^2(1 - M_i \hat{R}_i)^2} \right]_{ret} dS \quad . \quad (2.66) \\
 & + \int_{g=0} \left[\frac{L_i \hat{R}_i (M_i \hat{R}_i - M^2)}{R^2(1 - M_i \hat{R}_i)^3} \right]_{ret} dS
 \end{aligned}$$

The subscript *ret* denotes the evaluation of the integrand at the time of emission, i.e. the retarded time. The acoustic probes are equally distributed in a circle, described later in chapter 5, at 1.5 chords away from the DWT model.

Numerical setup

The simulation domain is a rectangular box equal to $23c$ in the free-stream direction x , and $26c$ in the $y - z$ plane perpendicular to the flow. see Figure 2.11. A three-dimensional DWT model is located $9c$ downstream of the inlet. Free-stream velocity boundary conditions are applied at $x = -9c$ while pressure outlet boundary conditions are applied at $x = 14c$. The side walls are defined using slip boundary conditions. In total, approximately 284 million voxels and 52 million surfels are used to discretize a single case. A total of 11 mesh refinement regions, named as VR (volume resolution), with resolution factor equal to 2 are employed, see Figure 2.12. For simulating the rotating turbine blades within the fixed duct geometry, the three dimensional computational domain is divided into an inner and an outer domain. The inner domain has a mesh fixed with the turbine, which is specified as sliding mesh. The outer domain forms a ground-fixed domain, which does not have relative motion. The inner and outer domains are connected by a closed, zero-thickness, transparent interface.

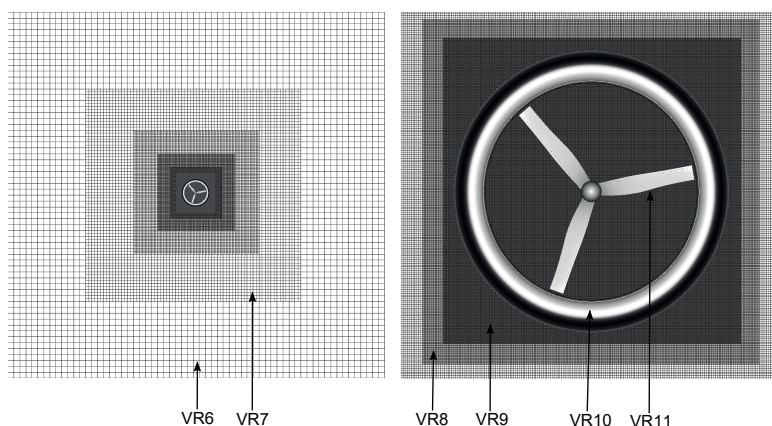


Figure 2.12: Volume resolution (VR) region distribution used to discretize the DWT models showing the front view (left) and zoomed-in view (right) for the DWT model.

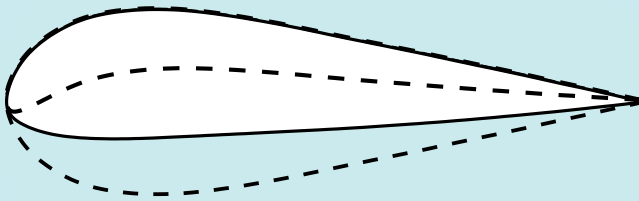
Additional details on the numerical implementation of sliding mesh, and validation examples, are given by [Perot et al. \[2012\]](#). A mesh independent study will be detailed in the relevant section of chapter 5.

The data of this CFD modelling effort is approximately 2 Terabyte for a single case study. The VLES solver, 3DS Simulia PowerFLOW, is designed to periodically output the transient data for different flow quantities. Transient data is then binned into time segments to calculate the time-averaged statistics of the flow. The instantaneous values of velocities and surface forces are recorded during seventh to ninth turbine rotations after the flow quantities becomes quasi-steady.

LB-VLES method solutions capture the unsteady aerodynamic interactions between the duct and the turbine blades at the expense of very high computational and memory costs. LB-VLES method is particularly appealing for the final stages of DWT design analysis due to its higher order of numerical fidelity in comparison to the panel, RANS and URANS methods.

3

Duct shape parametrization



3.1	Numerical validation	39
3.2	Duct shape parametrization	43
3.3	Aerodynamic performance coefficients	46
	Duct force coefficient	47
	Power coefficient	47
3.4	Flow-field analysis	47
3.5	Summary	50

This chapter is part of the following publication:

V. V. Dighe., G. de Oliveira., F. Avallone., & G. J. W. van Bussel., (2019). Characterization of aerodynamic performance of ducted wind turbines: A numerical study. *Wind Energy*.

*Design is not just what it looks like and feels like;
design is how it works.*

Steve Jobs

In leading up to this chapter, considerable amount of research undertaken into the designs of ducts for DWT application has been reviewed. The reader is referred to the work of Phillips et al. [2008] in particular for understanding the evolution of ducts for DWT designs. The existing literature, however, misses out a detailed parametric study on the effects duct cross-section shape affecting DWTs aerodynamic performance. The goal of this chapter lies in the characterization of the aerodynamic performance of the DWT based on duct shape parametrization, in particular the effects of the camber and the thickness of the duct cross-section. To this intent, numerical calculations using panel method and RANS method are shown. The DonQi[®] duct from a commercial DWT model is used as the reference case. The rotor is modelled as an AD with radially uniform thrust coefficient.

First, section 3.1 starts with verification and validation of the numerical methods against experimental findings. The duct shape modification is carried out using the class-shape transformation (CST) method and is discussed in section 3.2. The effects of the duct cross-section geometry on the aerodynamic performance coefficients are discussed in section 3.3, followed by flow analysis in section 3.4.

3.1. Numerical validation

Experimental data reported by Tang et al. [2016] are used for the numerical validation study. Experiments were carried out in the closed-loop open-jet (OJF) wind tunnel facility at the Delft University of Technology. The wind tunnel nozzle exit measures 2.85 m × 2.85m. The tunnel can operate at maximum speed of 35 m/s. The free-stream flow at the measurement location has a turbulent intensity of approximately 0.21% [Lignarolo et al., 2016]. The flow temperature is kept constant at 20°C, which is achieved by a 350 kW heat exchanger.

The duct geometry used is taken from a commercial 'DonQi[®] Urban Windmill 1.5' DWT model, see Figure 3.1. It was designed with support from the Nederlands Lucht-en Ruimtevaartcentrum (NLR) and the prototype was made available in the context of the DUCT4U project (STW grant number 12728). A 0.002 m thick wire mesh screen with porosity $\phi = 70\%$ is used to mimic the rotor. It results in an equivalent thrust coefficient, $C_{TAD} = 0.65$. The duct chord c measures 1 m. For all calculations, the lengths are normalized with the duct chord length c . The AD



Figure 3.1: Pictures showing the experimental setup with hot-wire anemometer placed on the traversing system (left) and pressure taps located along the duct surface (right).

diameter measures $y/c = 1.5$, which is located at $x/c = 0.28$. The tip clearance between the AD tip and the duct nozzle surface is $2.0\%c$. Free-stream velocity $U_\infty = 5\text{m/s}$ resulting in Reynolds number $Re = 4.5 \times 10^5$. Forces on the AD and the duct surface were measured using a six-component balance system. Velocimetry measurements were recorded using a constant temperature hot-wire anemometer installed on a traversing system. Surface pressure measurements on the duct walls were carried out using 52 pressure taps arranged along the duct chord length. Velocimetry data and pressure measurements are used for the numerical validation.

For the current investigation, two numerical methods are used: two-dimensional panel method described in section 2.2.2, and two-dimensional steady RANS method described in section 2.2.3.

The duct surface discretization, using the panel method, is based on the gradient-based spacing approach. The streamwise discretization is non-uniform, with initial panel length equal to $1.0\%c$ just behind the AD, and increasing gradually in length as the wake expansion settles further downstream, see Figure 3.2. This approach allows to capture the solutions of interest and also to reduce the overall computational costs.

A mesh independence analysis for the RANS simulations has been carried out using three mesh sizes where the refinement factor in each direction is approximately 1.5. The decay of the axial velocity distribution across the AD in the wake region, from the AD location to the outlet of the computational domain, is taken as reference. The results of the mesh independence study are shown in Figure 3.3. The medium refined mesh, consisting of approximately 137,600 mesh elements, is selected for the rest of the study.

A validation study has been performed where the CFD results, obtained from the 2D panel method and the 2D RANS method, are compared against the experimental data by Tang et al. [2016]. In order to assess the validity of the 2D axisymmetric approach, a 3D RANS simulation is performed and compared in this section. The 3D mesh is obtained by extruding the 2D mesh along the frame of rotation. The numerical settings for 3D RANS simulation are identical to the one discussed in section 2.2.3.

Firstly, the comparison of center-line axial velocity distribution inside of the

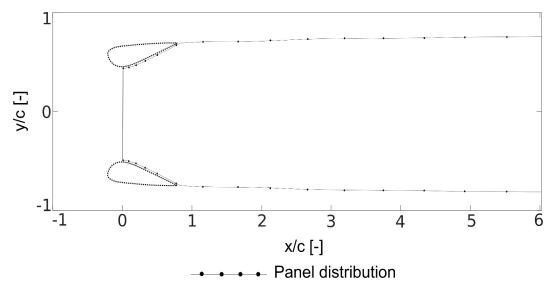


Figure 3.2: Panel distribution along the duct surface and the wake region used for the panel method calculations.

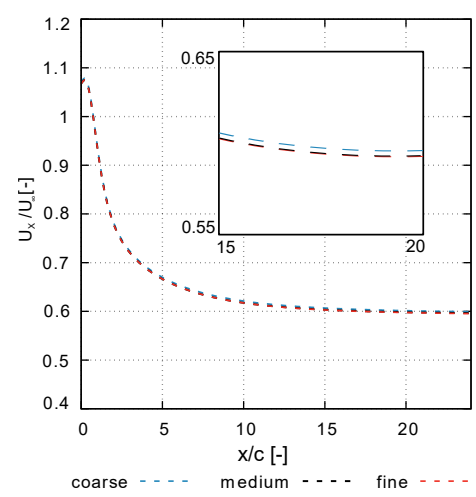


Figure 3.3: Mesh independence study showing decay of centerline axial velocity measured across the computational domain.

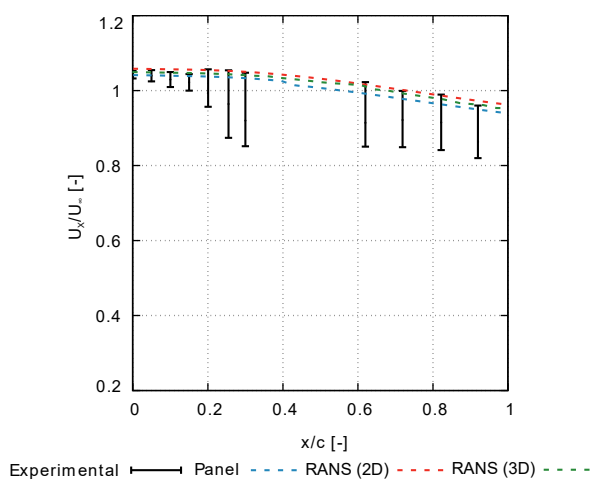


Figure 3.4: Comparison of the CFD results with the experiments. The measurements indicate the axial velocity in the streamwise direction inside of the duct. Error bars indicate the fluctuations in readings from several steady measurements.

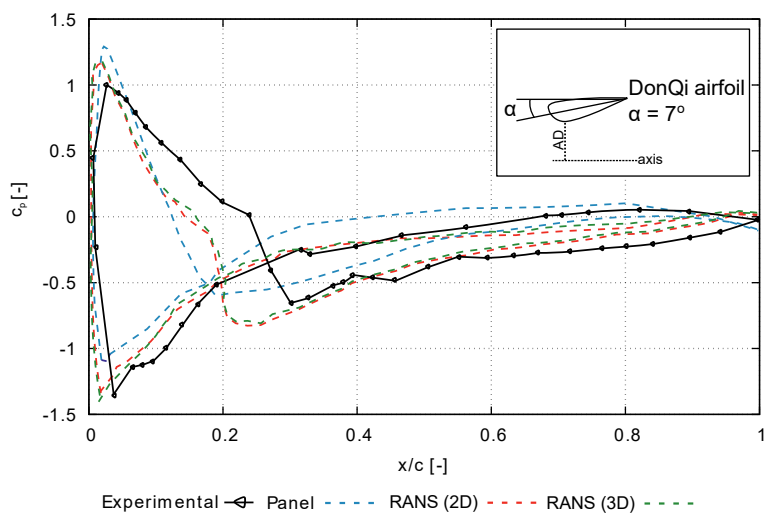


Figure 3.5: Comparison of the numerical surface pressure coefficient c_p with the experiments ($C_{TAD} = 0.65$).

duct is reported in Figure 3.4. Error bars represent the fluctuations in readings from several steady measurements. The velocimetry measurements, especially in the region just upstream and just downstream of the AD, fluctuates because of the fact that the meshed screen simulating the AD is intrinsically non-uniform, thus leading to flow unsteadiness. The deviation of the numerical results from the experiment is 1.8-14.7% and 8.2-9.5% for the upstream and downstream locations (comparing the mean values from the experimental data), respectively. The reason is likely due to the blockage effect of the wind tunnel, which results in an increased velocity decay rate at the measurement locations. Further explanations for the observed deviation and wind tunnel blockage correction methods are comprehensively presented in Tang et al. [2016].

Secondly, Figure 3.5 shows the comparison of wall pressure coefficients c_p measured along the surface of the duct in the chord-wise direction. The effect of AD is present at the suction side as a pressure jump at AD location; this is the region where the curves intersect. The off-set in the intersection locations of the AD between experiment and computations causes the differences in the location of the pressure jump. The AD position during the experimental setup is not at the nozzle plane of the duct but at $x/c = 0.28$ due to the design limitations. Differently, in the computations, the AD is placed at the nozzle plane ($x/c = 0.2$); the nozzle plane where the highest velocity within the duct cross-section is found [van Bussel, 2007]. Evidently, the AD location influences the quality of the validation, however, the overall computed c_p shows trends in good agreement with the experiment. The differences in the 2D RANS and 3D RANS solutions, as observed in Figures 3.4 and 3.5, are negligible when comparing the global trends of center-line axial velocity distribution and duct wall pressure coefficients. The computing cost issued by going from 2D RANS to 3D RANS increases by a factor of five and does not justify the scope of the study, where the effects of distributed AD loading, wake rotation and divergence are totally ignored.

3.2. Duct shape parametrization

The duct shapes, in topological space, represent one-dimensional manifolds whose complete description requires large number of parameters. The manifolds, however, share peculiar features: cross-sections always consist of a closed curve forming a smooth leading edge and a cusped trailing edge. These features are common with airfoil cross-sections, so the design space of all possible duct cross-sections can be approximated with airfoil parametrization techniques.

Several methods for parameterizing airfoil shapes have been documented [Hicks and Henne, 1977, Sobieczky, 1988, Kulfan and Bussoletti, 2006, Xiaoqiang et al., 2018]. Amongst these, the class-shape transformation (CST) method [Brenda and Bussoletti, 2006, Brenda, 2007] is known to provide nearly complete coverage of the design space [Masters et al., 2017]. Furthermore, it allows progressive design refinement [de Oliveira, 2011] and does not suffer from surface-waviness issues observed in spline based methods [Fuglsang et al., 2004]. This section represents the DonQi[®] reference duct with CST parameters and

explains the duct shape modifications in the resulting parametric space.²

The CST representation of the duct describes the relative thickness ($\eta = y/c$) of its sides (suction and pressure) as functions of chord-wise distance ($\xi = x/c$) that depend on $i = 0 \dots M$ shape parameters ($A_i^{suction}$ and $A_i^{pressure}$):

$$\begin{cases} \eta_{(\xi)}^{pressure} = C_{(\xi)} S_{(\xi, A_i^{pressure})} \\ \eta_{(\xi)}^{suction} = -C_{(\xi)} S_{(\xi, A_i^{suction})} \end{cases} \quad \text{with} \quad C_{(\xi)} = (1 - \xi) \sqrt{\xi}. \quad (3.1)$$

3

Class functions (C) provide basic topological features, viz., round leading edge and cusped trailing edge, while shape functions (S) represent the specificities of each design.

Shape parameters for existing duct designs are obtained by solving a regression problem with duct coordinates $\{\eta_{ref}^{pressure}, \eta_{ref}^{suction}\}$. A N -th order shape function corresponds to the linear combination of a complete Bernstein basis of degree M with $N = M + 1$ shape parameters. Convexity is not established for this problem, so it is useful to start by formulating a linear guess ($A_i^{0,ref}$) of the solution:

$$A_i^{0,ref} : M_{ij} A_j^{0,ref} = B_i \quad \text{with} \quad \begin{cases} M_{ij} = C_{(\xi_j)} S_{(\xi_j)}^{iM} \\ \xi_j = \frac{j}{M} \\ B_i = (\eta_{ref})_{\xi=\xi_i} \\ i, j = 1 \dots M \end{cases}, \quad (3.2)$$

and then proceed to solve the full non-linear problem with a Levenberg-Marquart algorithm [More, 1977]. Solutions (A_i^{ref}) for each side are obtained separately with a simple least squares norm (\mathcal{L}):

$$A_i^{ref} : \mathcal{L}_{(A_i^{ref}, \eta_{ref})} = \min_{A_i} L_{(A_i, \eta_{ref})} \\ \mathcal{L}_{(A_i, \eta_{ref})} = \int_0^1 (C_{(\xi)} S_{(\xi, A_i)} - \eta_{ref})^2 d\xi. \quad (3.3)$$

Equations 3.2 and 3.3 are solved to fit coordinates of the DonQi[®] reference duct with 16 parameters per side. The resulting 15th degree polynomials match the reference cross-section with a maximum normal offset smaller than 3×10^{-4} chords, which is well below practical manufacturing tolerances [Ernst et al., 2012].

The parametrization procedure for duct shapes in the current analysis should preserve the following features: leading edge position (which defines the inlet-area-ratio), trailing edge position (which defines the exit-area-ratio) and inner side thickness (which defines AD diameter and tip clearance). This makes it ideal to

²In the preliminary stages of the research, the author performed a brute-force approach for duct shape selection, see for example [Dighe et al., 2018]

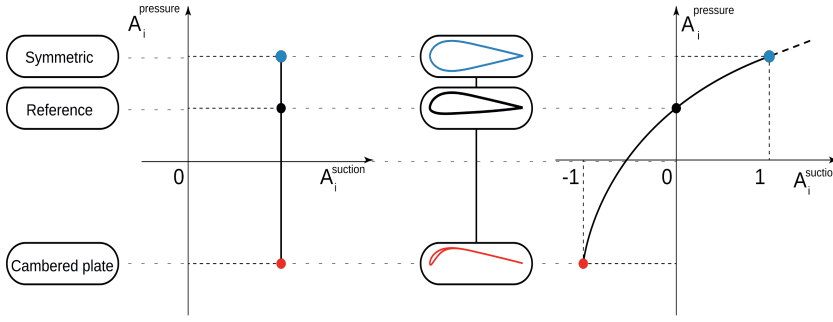


Figure 3.6: A schematic representing the procedure for duct shape modification in CST parameter space.

3

isolate the effect of camber on the overall performance.³ The DonQi[®] duct airfoil (A_i^{ref}) is chosen as the reference shape. In effect of duct shape parametrization, the camber of the DonQi[®] duct profile is varied by changing its pressure side while leaving its suction side untouched. First, the two extreme variants of the reference shape corresponding to cambered plate profile (A_i^{plt}) and symmetric profile (A_i^{sym}) are defined, see Figure 3.6,

$$\begin{cases} A_i^{plt,suction} = A_i^{ref,suction} & i = 0 \dots M \\ A_i^{plt,pressure} = -A_i^{ref,suction} & i = 1 \dots M \\ A_i^{plt,pressure} = A_i^{ref,pressure} & i = 0 \\ A_i^{sym,suction} = A_i^{ref,suction} & i = 0 \dots M \\ A_i^{sym,pressure} = A_i^{ref,suction} & i = 0 \dots M \end{cases} \quad (3.4)$$

The second step consists in obtaining shape parameters for the modified duct profiles (A_i^{mod}) by interpolating between design variants. This is achieved with a quadratic interpolant of a single variable (γ):

$$A_i^{mod} = a_i \gamma^2 + b_i \gamma + c_i \quad \begin{cases} a_i = \frac{1}{2} (A_i^{sym} + A_i^{plt}) - A_i^{ref} \\ b_i = \frac{1}{2} (A_i^{sym} - A_i^{plt}) \\ c_i = A_i^{ref} \end{cases} \quad (3.5)$$

The reference DonQi[®] duct is recovered by setting $\gamma = 0$, while values of $\gamma = 1$ and $\gamma = -1$ produce symmetric and cambered plate variants, respectively. Equation 3.5 provides parameters for any design with γ greater than -1 , and duct profile coordinates can be reconstructed from parameters with equation 3.1.

³In the paper from Bontempo and Manna [2016], the duct camber was varied by bending the rear part of the duct profile in the outward direction by 5 and 10 degrees. In this way, the effective duct rotor to duct exit-area-ratio was also varied, and therefore the performance improvement attributed to the change of the duct camber only, creates confusion when the power coefficient is calculated using the duct exit section.

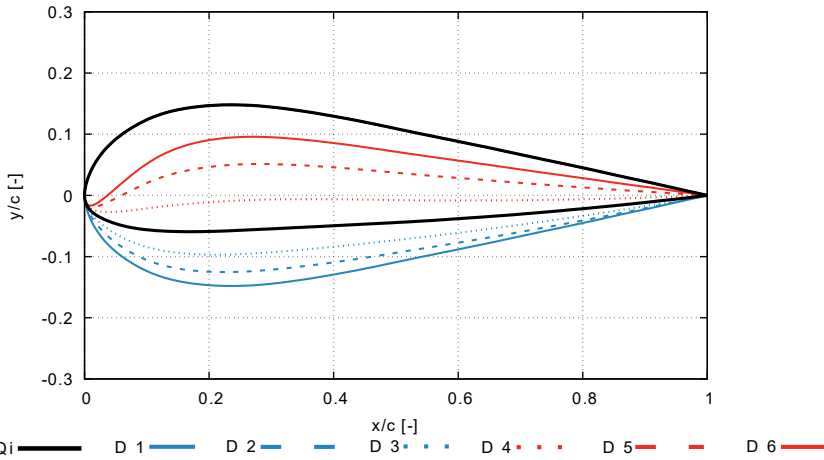


Figure 3.7: Duct profiles with different camber and thickness distribution used in the numerical study.

Table 3.1: Aerodynamic characteristics of the duct profiles with different relative thickness values.

Profile	γ value	Maximum thickness (%c)	C_L at $\alpha = 0^\circ$
D1	+0.9	29.60%	0.002
D2	+0.6	27.32%	0.124
D3	+0.3	24.46%	0.198
DonQi	0	20.60%	0.312
D4	-0.3	15.79%	0.524
D5	-0.6	10.36%	0.703
D6	-0.8	8.03%	0.809

3.3. Aerodynamic performance coefficients

This section provides an extensive analysis of the effects of the duct shape on the duct thrust force coefficient C_{T_D} and power coefficient C_p under different values of AD loading $C_{T_{AD}}$. To this aim, seven duct geometries, shown in Figure 3.7, are adopted.⁴ The aerodynamic characteristics, in terms of the lift coefficient C_L , of the duct profiles is shown in Table 3.1. The C_L values are shown for $Re = 4.5 \times 10^5$, as in the experiment described in section 3.1. For all the calculations, hereinafter, the duct chord c measures 1 m. The AD measures $y/c = 1$, and is located at the duct nozzle plane, $x/c = 0.22$. The tip clearance between the AD tip and the duct nozzle surface is $2.0\%c$.

⁴It is important to note that the geometric variations in the duct profiles are achieved by preserving the inner duct surface, and thereby fixing the duct exit-area-ratio, and varying the camber by changing the outer side of the duct surface

3.3.1. Duct force coefficient

Figures 3.8 and 3.9 illustrate the correlation between the duct thrust force coefficient C_{TD} and the AD thrust force coefficient C_{TAD} obtained using the panel and RANS methods, respectively. In general, for lower AD loadings ($C_{TAD} \leq 0.6$), the C_{TD} value increases with the increasing C_{TAD} . Subsequently, a local C_{TD} maximum for the individual duct airfoils appears. The value of C_{TD} decreases for C_{TAD} beyond the local maximum. Furthermore, the magnitude of C_{TD} increases with the duct cross-section camber. A good agreement is achieved between the panel and the RANS solutions, with two noticeable exceptions. Firstly, the magnitude of C_{TD} calculated using the panel method is lower than the one calculated with the RANS method across the entire C_{TAD} range. Secondly, unlike the panel method solutions, the trend-lines for duct profiles *D4*, *D5* and *D6* obtained using the RANS method intersect at higher AD loadings ($C_{TAD} \geq 0.6$). In fact, the value of the local maximum attained for duct *D6* using RANS calculations is lower than the one attained for duct *D5*. The main cause of the differences is the viscous interaction between the duct surface and the AD accounted for by RANS solutions only. To this aim, physical insights on the local flow changes due to the duct camber will be discussed in section 3.4. Nevertheless, the comparison of the C_{TD} predictions by both the numerical methods indicate that the mutual interaction between the duct and the AD is non-linear, and this interaction needs to be taken into account for the design of DWT systems.

3.3.2. Power coefficient

Figures 3.10 and 3.11 show the power coefficients C_p , using the panel and RANS solutions respectively, as a function of variable AD loading C_{TAD} . By analogy, the C_p trend appears as a characteristic corollary of the duct force coefficient C_{TD} . The larger the C_{TD} (see Figures 3.8 and 3.9), the higher the C_p , and vice-versa. Similar to C_{TD} solutions, the C_p trend-lines for duct profiles *D4*, *D5* and *D6* obtained using the RANS method begin to intersect at higher AD thrust coefficients ($C_{TAD} \geq 0.6$). In the absence of viscous mutual interaction, as in the panel method solutions, the magnitude of C_{TD} and ultimately the C_p increases with the duct cross-section camber for the same value of C_{TAD} . Contrarily, for the RANS solution, the effect of camber on the C_p displays an upper limit. Then, the maximum $C_p \approx 0.82$ is obtained for *D5* for $C_{TAD} \approx 0.75$. Moreover, present results show that the maximum C_p is obtained for a C_{TAD} value, which is lower than 8/9, unlike the linearized method used for the analysis of DWT [van Bussel, 2007].

3.4. Flow-field analysis

In order to highlight the effects of the duct shape and the viscous interactions onto the performance coefficients of the duct-AD model, shown in subsections 3.3.1 and 3.3.2, a flow field analysis using RANS solutions is carried out. Velocity contours colored with normalized free stream velocity $\frac{U_x}{U_\infty}$ are shown in Figures 3.12, 3.13 and 3.14. For the current analysis, duct profiles *D4*, *D5* and *D6* for $C_{TAD} = 0.6$, 0.7, 0.8 and 0.9 are considered to have a closer look at the best performing options

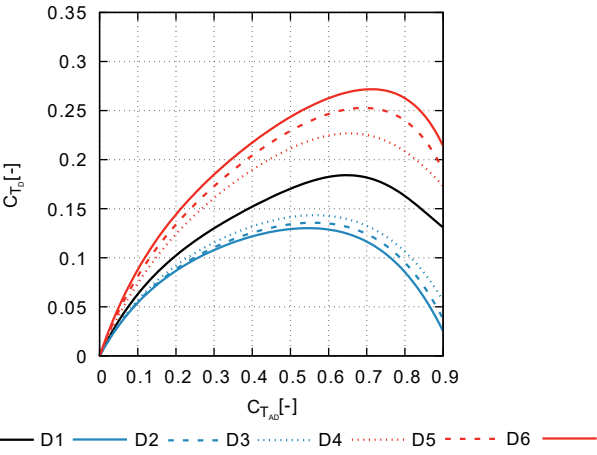


Figure 3.8: Effect of variable AD loading on duct thrust force coefficient using panel method solution.

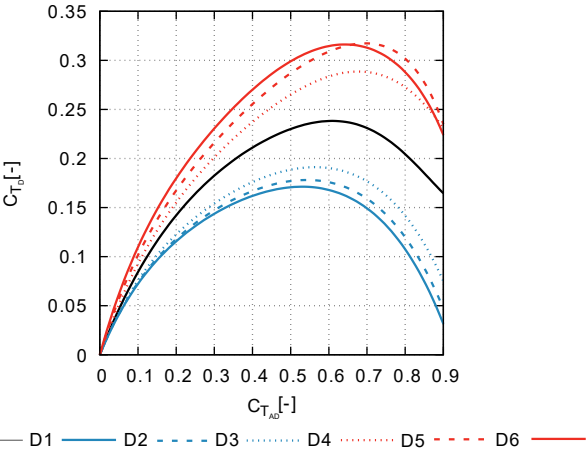


Figure 3.9: Effect of variable AD loading on duct thrust force coefficient using RANS method solution.

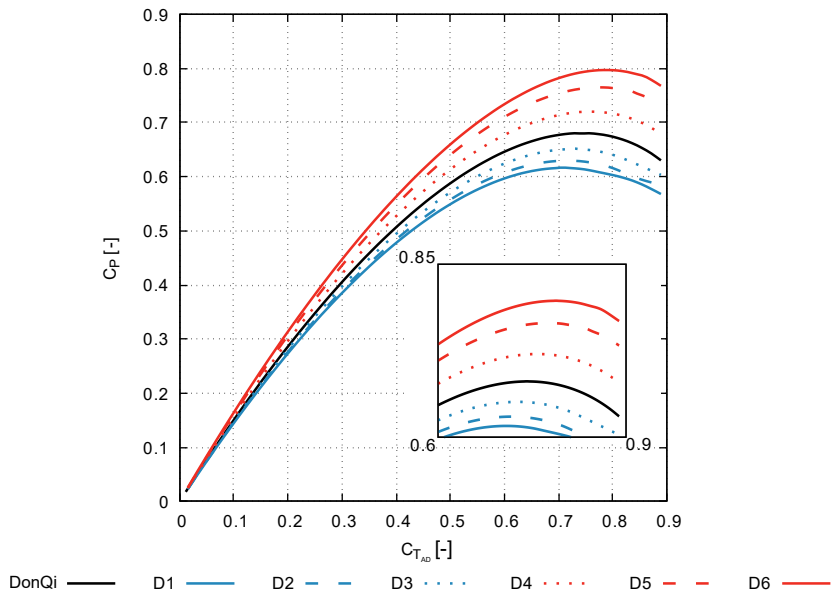


Figure 3.10: Effect of variable AD loading on power coefficient using panel method solution.

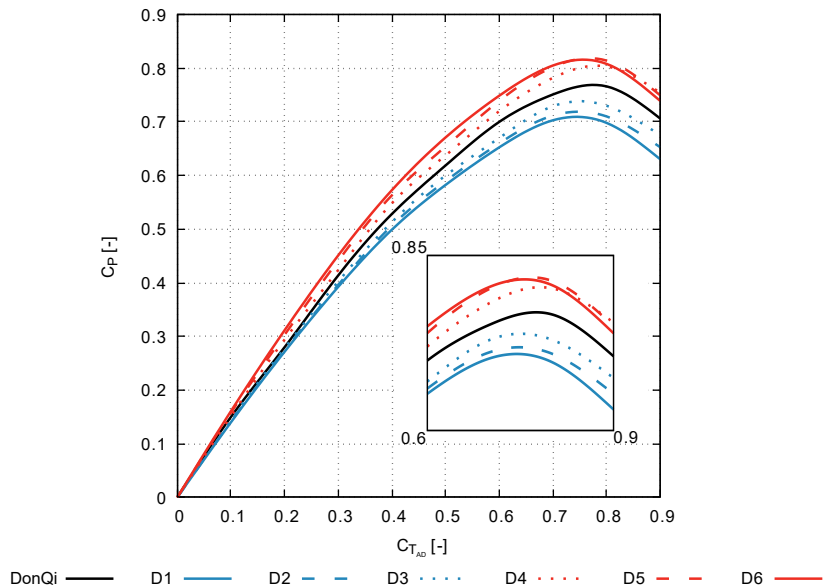


Figure 3.11: Effect of variable AD loading on power coefficient using RANS method solution.

and to explain the intersecting region in the performance trend-lines, as in Figures 3.9 and 3.11. It is convenient to start with duct profile $D4$ as a function of C_{TAD} in Figure 3.12. The velocity contours show that, with the increasing value of C_{TAD} , the leading edge stagnation point traverses further up along the suction side of the duct. Consequently, the magnitude of velocity at the suction side of the duct decreases and the magnitude of velocity at the pressure side of the duct starts to increase significantly. This means that the lift force on the airfoil shaped duct reduces with increasing C_{TAD} . This phenomenon, occurring at the surface of the duct, determines the steep reduction of C_{TD} at high values of C_{TAD} as in Figures 3.8 and 3.9. Furthermore, if $\frac{U_{AD}}{U_{\infty}}$ decreases quickly as a consequence of the reduced effectiveness of the duct, C_p also falls for high values of C_{TAD} . The above description of flow phenomena occurring along the duct surface with variation of the AD loading, ultimately governing the global performance of the duct-AD model, also applies to ducts $D5$ (see Figure 3.13) and $D6$ (see Figure 3.14), be it for slightly higher C_{TAD} .

Another very important phenomenon, which also affects the global performance of the duct-AD model, are the viscous effects creating flow recirculation region along the pressure side of the duct, especially for the highly cambered duct profile. Obviously, the viscous effects exists for RANS solutions only, and thereby exhibiting the intersection of performance trend-lines as in Figures 3.9 and 3.11. At high values of C_{TAD} , the recirculation region traverses from the pressure side of the duct to the suction side of the duct. Evidences of this are witnessed through velocity contours of $D5$ and $D6$, which exhibits flow separation along the trailing edge suction side of the duct for $C_{TAD} = 0.8$ and 0.9 , respectively. The onset of suction-side flow separation, which is earlier for duct $D6$ than $D5$, reduces the C_{TD} and ultimately the C_p of the prescribed duct-AD configuration.

3.5. Summary

In order to deepen the design principles of DWT, the effects of the duct shape onto the aerodynamic performance of DWTs are investigated. An improved duct shape parametrization using CST method is proposed. The analysis has shown the possibility to significantly increase the DWT performance by increasing the duct profile camber and a correct choice of rotor loading, whilst maintaining the same duct exit area ratio. In more detail, the overall performance improvement directly corresponds to the dimensionless duct thrust force coefficient. To better highlight the differences between the RANS and the panel codes, solutions for C_{TD} and C_p as a function of C_{TAD} are shown. The RANS solutions, however, exhibit an upper limit of the camber extent for maximum achievable performance. This phenomenon is characterized by a rapid reduction of C_{TD} and ultimately the C_p , for highly cambered duct profiles. The analysis highlights the limitations of the panel method when applied to highly cambered duct profiles for DWT analysis. A detailed flow analysis using RANS method shows that highly cambered duct profiles are prone to boundary layer flow separation, which is considered non-optimal for the overall aerodynamic performance.

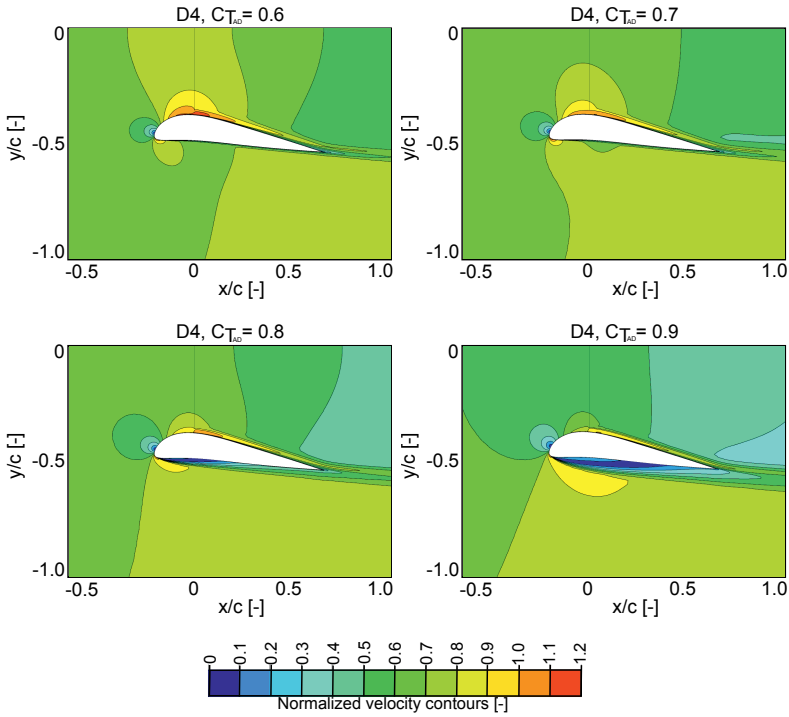


Figure 3.12: Velocity contours colored with normalized free-stream velocity $\frac{U_x}{U_\infty}$ around DonQi[®] duct-AD model with different values of C_{TAD}

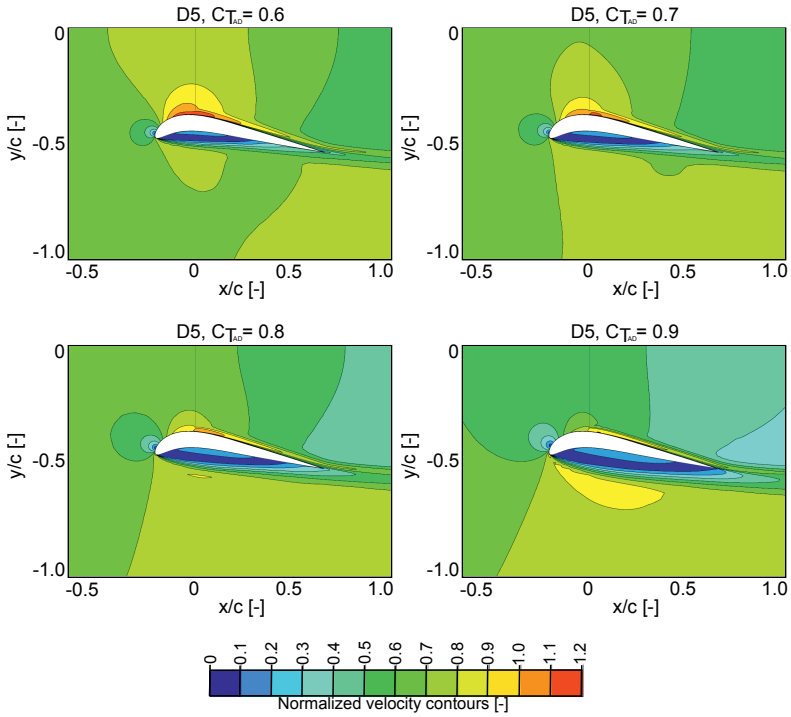


Figure 3.13: Velocity contours colored with normalized free-stream velocity $\frac{U_x}{U_\infty}$ around D5 duct-AD model with different values of $C_{T,AD}$

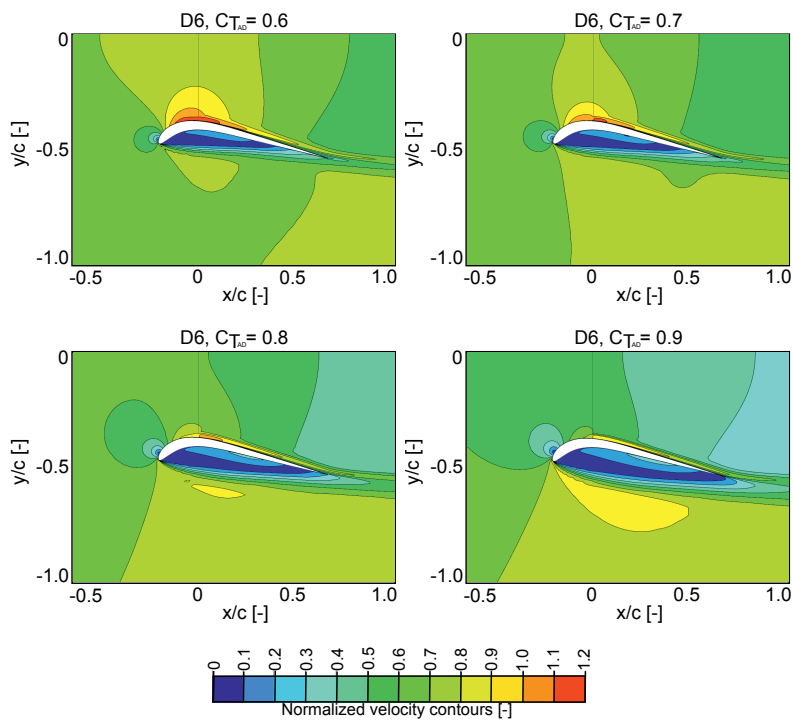
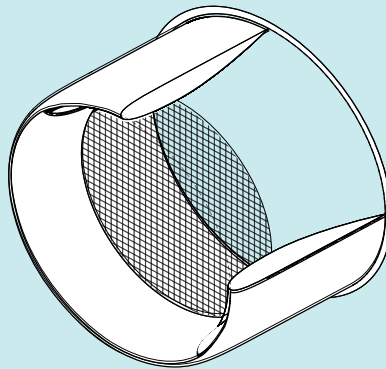


Figure 3.14: Velocity contours colored with normalized free-stream velocity $\frac{U_x}{U_\infty}$ around D6 duct-AD model with different values of $C_{T,AD}$

4

Further augmentation techniques



4.1	Multi-element ducts	57
	Numerical validation	58
	Multi-element duct geometry	61
	Duct force coefficient	62
	Power augmentation	64
4.2	Gurney Flap	67
	Experimental setup	67
	Aerodynamic analysis	67
4.3	Summary	72

This chapter is part of the following publications:

V. V. Dighe., F. Avallone., O. Igra, & G.J.W. van Bussel., (2019). Multi-element ducts for ducted wind turbines: a numerical study. *Wind Energy Science*, 4(3), 439-449.

V. V. Dighe., F. Avallone., J. Tang., & G.J.W. van Bussel., (2017). Effects of Gurney Flaps on the Performance of Diffuser Augmented Wind Turbine. *AIAA proceeding - 35th Wind Energy Symposium* (p. 1382).

*A good scientist is a person with original ideas.
A good engineer is a person who makes a design that works
with as few original ideas as possible.
There are no prima donnas in engineering.*

Freeman Dyson

In leading up to this chapter, the investigation has shown the possibility to increase the DWTs aerodynamic performance by increasing the duct profile camber and a correct choice of rotor loading. The next step is to ask the question as to how this performance can be further improved. The aerodynamic phenomenon related to DWT, which has only been investigated to a limited extent, is based upon the extraction of energy from the air flowing outside the duct. The process can be achieved by re-energizing the wake behind the duct in order to increase the mass flow through the turbine. As identified, different principles are considered to enhance the re-energization process: boundary layer suction and blowing [Gilbert and Foreman, 1983, Foreman and Gilbert, 1984], multi-element ducts [Igra, 1981], flanged diffuser [Abe et al., 2005, Toshimitsu et al., 2008] and vortex generators [Ten Hoopen, 2009]. On both practical and economic grounds, suction and blowing proved infeasible for DWTs due to the active system and its installation.

It would not be possible to cover all of the above phenomena in any great depth during the course of the current investigation. Within the scope of the current research, the effects of multi-element ducts in section 4.1 and Gurney Flap in section 4.2 on the aerodynamic performance of DWT are studied in detail.

4.1. Multi-element ducts

Multi-element ducts for DWT applications consists of a duct with Flap/Flaps. The Flap is realized as a secondary duct with a small chord airfoil cross-section mimicking high-lift devices for aircraft wings (see Figure 4.1). The first theoretical and experimental analysis of DWTs with a Flap was carried out by Igra [1981] and Gilbert and Foreman [1983]. Igra found that the addition of a Flap improves the DWTs aerodynamic performance by 25% with respect to a single duct. Gilbert and Foreman identified that the Flap inhibits flow separation along the inner duct wall, thus being beneficial for the aerodynamic performances of the DWT. The literature, however, misses out a detailed parametric study that investigates the effect of Flap's installation settings, i.e. the radial location and its angle of attack, onto the total power generated by a DWT.

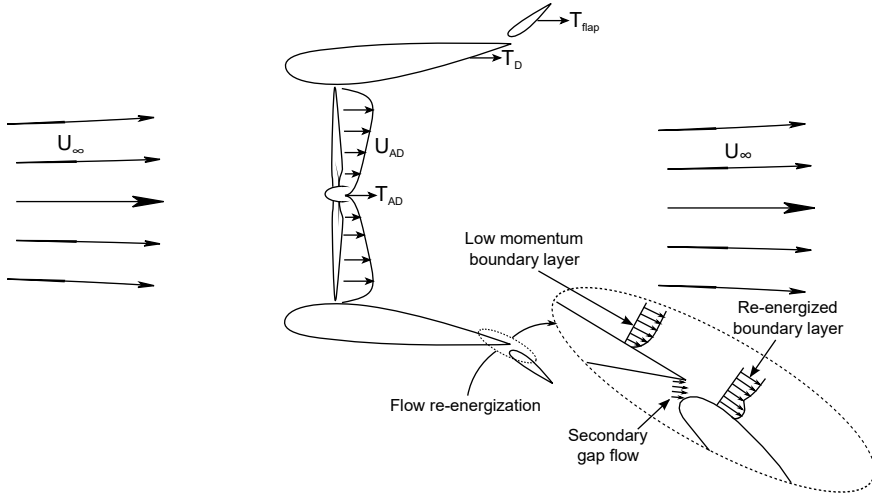


Figure 4.1: Schematic of flow around a multi-element ducted wind turbine.

Goal of the current investigation is to conduct a parametric study to account for the effect of the installation settings of the Flap on the aerodynamic performance of a multi-element DWT. To this aim, a reference multi-element duct is selected and the rotor is simulated by a uniformly loaded actuator disc (AD) model. The verification and validation of the numerical methods against experimental findings are reported in subsection 4.1.1. The details of the DWT model and the geometric parameters of the Flap installation settings are given in subsection 4.1.2. The dependence of the aerodynamic coefficients on the Flap's installation settings are discussed in subsections 4.1.3 and 4.1.4, followed by the most relevant conclusions summarized in 4.3.

4.1.1. Numerical validation

For validating the numerical methods, experiments reported by Igra [1981] were simulated. Igra's experiments were conducted in the subsonic wind tunnel of the Israel Aerospace Industries (formerly known as Israel Aircraft Industry); this tunnel has a large test section and it measures $3.6 \text{ m} \times 2.6 \text{ m}$.

Eight different geometries were investigated experimentally, but only two geometries are used for the validation study. The two geometries are: a duct-AD model with $C_{TAD} = 0.434$ (named as Model B) and a multi-element duct-AD model with $C_{TAD} = 0.550$ (named as Model C (ii) + Flap). A schematic of the cross-sections of the two geometries is shown in Figure 4.2. The longitudinal cross-section of the duct and of the Flap is a NACA 4412 airfoil. The leading edge of both duct geometries are identical. For Model C (ii) + Flap, the trailing edge of the duct is radially stretched resulting in a duct exit-area-ratio $\frac{S_{exit}}{S_{AD}} = 1.84$, this ratio is 1.71 for model B. The Flap chord measures 35% of the duct chord length c , and the deflection angle $\theta = 30^\circ$ with respect to the free-stream direction. The

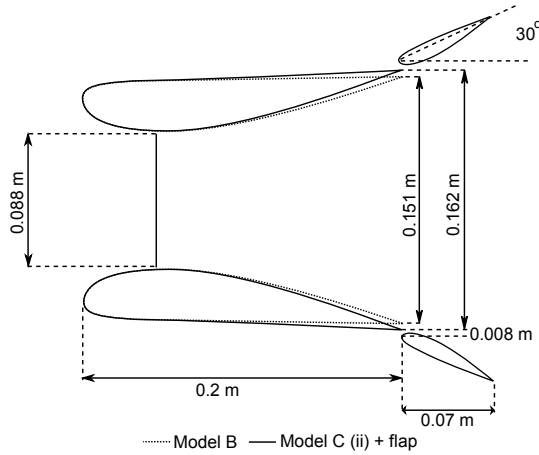


Figure 4.2: A schematic cross-section layout of the three dimensional experimental model [Igra, 1981] used for the numerical validation study.

Table 4.1: Comparison of power augmentation factor r calculated using experiments, panel method, RANS method and URANS method for two different duct configurations.

Model	Experiments	Panel	RANS	URANS
Model B	1.21	1.2056	1.2014	1.2033
Model C (ii) + Flap	2.02	2.0641	1.9821	1.9981

experimental dataset consists of: static pressure distribution at different axial and radial positions, and forces generated by the duct and the Flap surfaces. During the experiments, the free-stream velocity was set at $U_\infty = 32$ m/s corresponding to $Re \approx 4.5 \times 10^5$. Following Igra [1981], the wall interference and blockage correction can be ignored.

The panel method, RANS method and URANS method are used for the numerical validation study. In Table 4.1, the results of power augmentation factor r calculated, as in equation 2.17, are shown. A very good agreement between the CFD simulations and the experimental findings is found for Model B and Model C (ii) + Flap, where the maximum deviation of the CFD results from the experimental data is 0.55% and 2.13% for Model B and Model C (ii) + Flap, respectively.

The differences in the CFD results can be explained by looking at the flow-field. Figure 4.3 shows the contours of non-dimensional axial velocity $\frac{u_x}{U_\infty}$ computed with the three numerical methods for Model C (ii) + Flap. Velocity contour from the panel method is plotted on the top, steady RANS in the middle, and URANS on the bottom. A clear difference in the flow-field between the panel and the RANS (steady and unsteady) methods could be identified from the contour plots. Neglecting viscosity, as in the panel method solution, the flow remains attached over the surface of the duct. As a result, the magnitude of velocity on the suction side, and ultimately

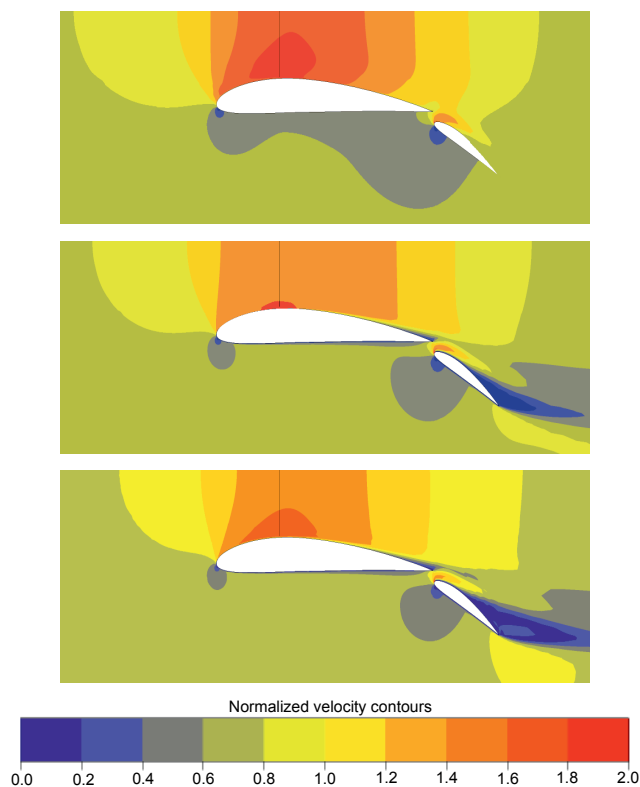


Figure 4.3: Velocity contours colored with normalized free stream velocity obtained using: (top) panel method, (center) RANS method and (bottom) URANS method for Model C (ii) + Flap

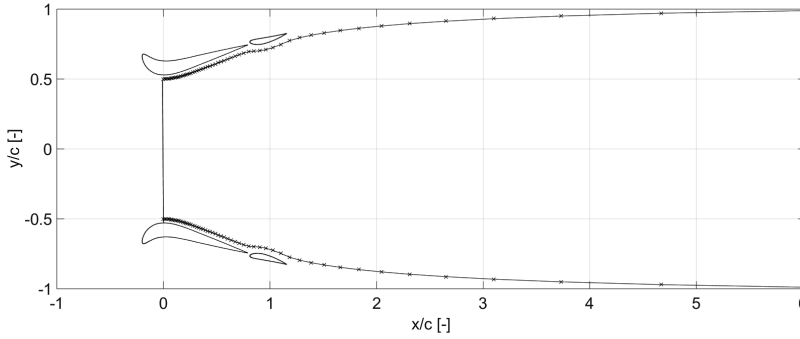


Figure 4.4: Panel distribution along the multi-element duct surface and the wake region used for the inviscid panel method calculations.

the value of r (Table 4.1), is larger for panel method solution in comparison to the RANS (steady and unsteady) method solutions. On the other hand, the flow field obtained using steady and unsteady RANS methods are almost identical. Both the steady and unsteady RANS solutions show flow separation along the inner walls of the Flap. Subtle differences appear in the flow separation region, where the velocity contour patterns differ slightly in their spatial organization. In URANS solution, the turbulent flow structures, which evolve in time and space, are explicitly computed. These flow structures are temporally averaged in the RANS solution. The net result of such different formulations explains the difference in the value of r in Table 4.1 calculated using steady and unsteady RANS methods.

Although URANS simulations increase the level of description of the unsteady flow due to the multi-element duct-AD interaction, the computing cost issued by going from RANS to URANS does not justify the scope of the current study, where the effects of distributed AD loading, wake rotation and divergence are totally ignored.

The duct surface discretization (section 3.1), using the panel method, is modified to take into account the Flap geometry (see Figure 4.4). RANS solutions are sensitive to the discretization of the computational domain. A mesh independence study has been carried out using three grid sizes, where the refinement factor in each direction is approximately 1.5. The multi-element duct thrust force coefficient C_{TD}^* , is taken as reference for the convergence analysis. The results of the grid independence study are shown in Table 4.2. Convergence is reached for the medium refined grid, and used for the RANS simulations shown, hereinafter.

4.1.2. Multi-element duct geometry

The multi-element duct-AD configuration investigated in the present work is shown in Figure 4.5. The longitudinal cross-section of the duct is DonQi D5 airfoil; the profile is chosen based on the duct shape parametrization study conducted in chapter 3. For the DonQi D5 duct an optimal $C_{TAD} = 0.7$ was obtained; inner duct

Table 4.2: Mesh statistics for mesh independence study of the reference case.

Mesh type	Number of cells	C_{TD}^*
Coarse	85890	0.17830
Medium	148380	0.18233
Fine	229300	0.18231

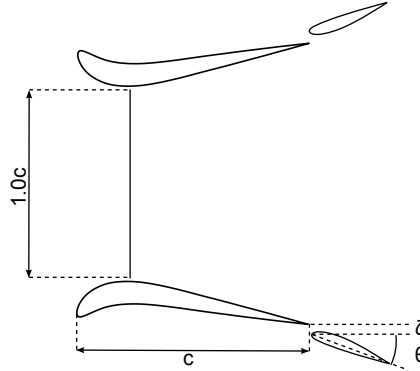


Figure 4.5: A schematic cross-section of the multi-element duct-AD model with the variable Flap parameters used for the Flap installation study.

wall flow separation was observed for $C_{TAD} > 0.7$ and thereby reducing the overall performance. For this reason, $C_{TAD} = 0.7$ is employed throughout the present discussion. Following the discussion in section 3.3, the duct chord measures 1 m. The AD measures $y/c = 1$, and is located at $x/c = 0.2$. The tip clearance between the AD tip and the duct nozzle surface is $0.02c$ (2% of duct chord length). A NACA 4412 longitudinal cross-section, measuring $0.35c$, is chosen for the Flap following Igra [1981]. The Flap installation settings are: the radial gap ζ and the deflection angle θ . The radial gap ζ , indicated as percentage of duct chord length c , is defined as the distance from the trailing edge of the duct to the leading edge of the Flap. A positive value of radial gap ($\zeta > 0$) indicates that leading edge of the Flap is positioned below the trailing edge of the duct. A positive deflection angle ($\theta > 0$) corresponds to a downward Flap deflection, where the angle is defined relative to the free-stream direction. The axial gap between the trailing edge of the duct and the leading edge of the Flap is zero based on the findings of Igra [1981]. The numerical study is performed at a fixed $Re = 4.5 \times 10^5$ as in the experiments.

4.1.3. Duct force coefficient

Contours of duct thrust force coefficient C_{TD}^* , as in equation 2.20, obtained from panel and RANS methods, are shown in Figures 4.6 and 4.7. C_{TD}^* as a function of the radial gap ζ and the deflection angle θ are reported. The figures show that C_{TD}^* increases for larger ζ . Conversely, C_{TD}^* decreases with the increasing θ . The

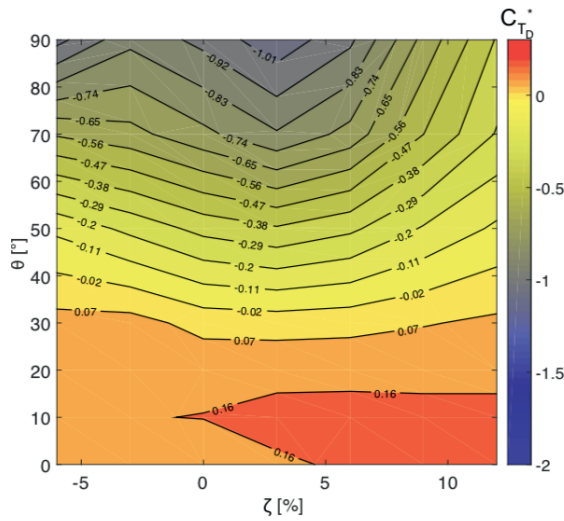


Figure 4.6: Effect of variable radial gap and deflection angle of the Flap on the duct thrust force coefficient using panel method.

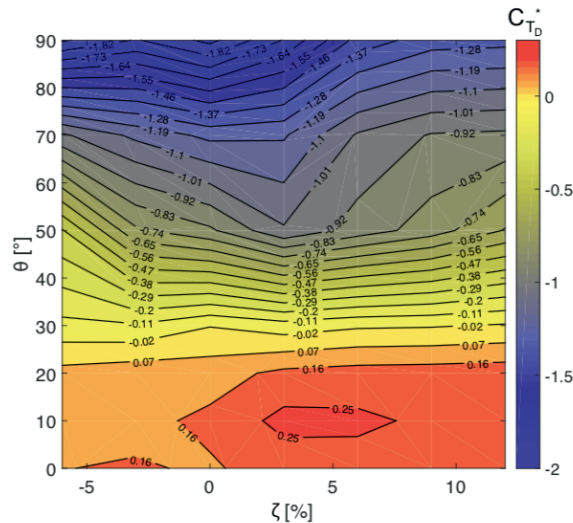


Figure 4.7: Effect of variable radial gap and deflection angle of the Flap on the duct thrust force coefficient using RANS method.

maximum C_{TD}^* obtained from both the numerical methods lie in the same region, i.e. $\zeta \approx 5\%$ and $\theta \approx 10^\circ$. The differences between results obtained using the panel and RANS methods increases for $\theta \geq 60^\circ$.

The differences can be explained by looking at the flow field. Contours of non-dimensional axial velocity $\frac{U_x}{U_\infty}$ from both methods are reported in Figures 4.8 (a)-(f). Results from the panel method are plotted on the left while the ones from RANS method on the right. Contours for no-Flap configuration are shown in Figures 4.8 (a) and (b). Two Flap settings, in order to explain the aerodynamics behind the trends obtained in Figures 4.6 and 4.7, are shown: $\zeta = 5\%$ and $\theta = 10^\circ$ in Figures 4.8 (c) and (d) and $\zeta = 5\%$ and $\theta = 70^\circ$ in Figures 4.8 (e) and (f).

Contour plots show a higher velocity at the AD plane for the configuration with Flap in comparison with no-Flap configuration. This is due to the additional aerodynamic thrust force generated by the Flap. The presence of a radial gap between the duct and the Flap accelerates the flow over the Flap. This reduces the pressure recovery demands on multi-element duct, thereby reducing flow separation. Obviously, flow separation is seen for RANS contours only. The overall integral contribution of the viscous forces increases the C_{TD}^* magnitude in the RANS solutions relative to the panel solutions; a trend that can be clearly observed by comparing Figures 4.6 and 4.7. For the Flap configuration with $\zeta = 5\%$ and $\theta = 70^\circ$, as in Figure 4.8 (f), the flow over the Flap's inner walls separates completely. The separation along the inner walls of the multi-element duct reduces the C_{TD}^* , which rapidly becomes large and negative at higher Flap deflection angles as seen in Figure 4.7. For panel method solutions, however, the drop in the C_{TD}^* magnitude for higher Flap deflection angles is gradual (see Figure 4.6) because viscous effects are neglected (see Figure 4.8 (e)).

4.1.4. Power augmentation

Figures 4.9 and 4.10 represents contours of power augmentation factor r , using the panel and RANS solutions respectively, as a function of radial gap ζ and deflection angle θ . Recall, from equation 2.22, that a r gain for a multi-element duct-AD model can be attained by increasing the C_{TD}^* magnitude for a constant $C_{T,AD}$. Evidence of this is provided in Figures 4.9 and 4.10, which exhibits the maximum r in the same region of maximum C_{TD}^* , as in Figures 4.6 and 4.7. Then, the maximum power augmentation factor $r_{max} = 1.25$ and 1.38 , obtained for panel and RANS calculations respectively, corresponds to $\zeta \approx 5\%$ and $\theta \approx 10^\circ$.¹

¹A comparison of r_{max} obtained from CFD simulations with the one-dimensional axial momentum theory is carried out, see Appendix D

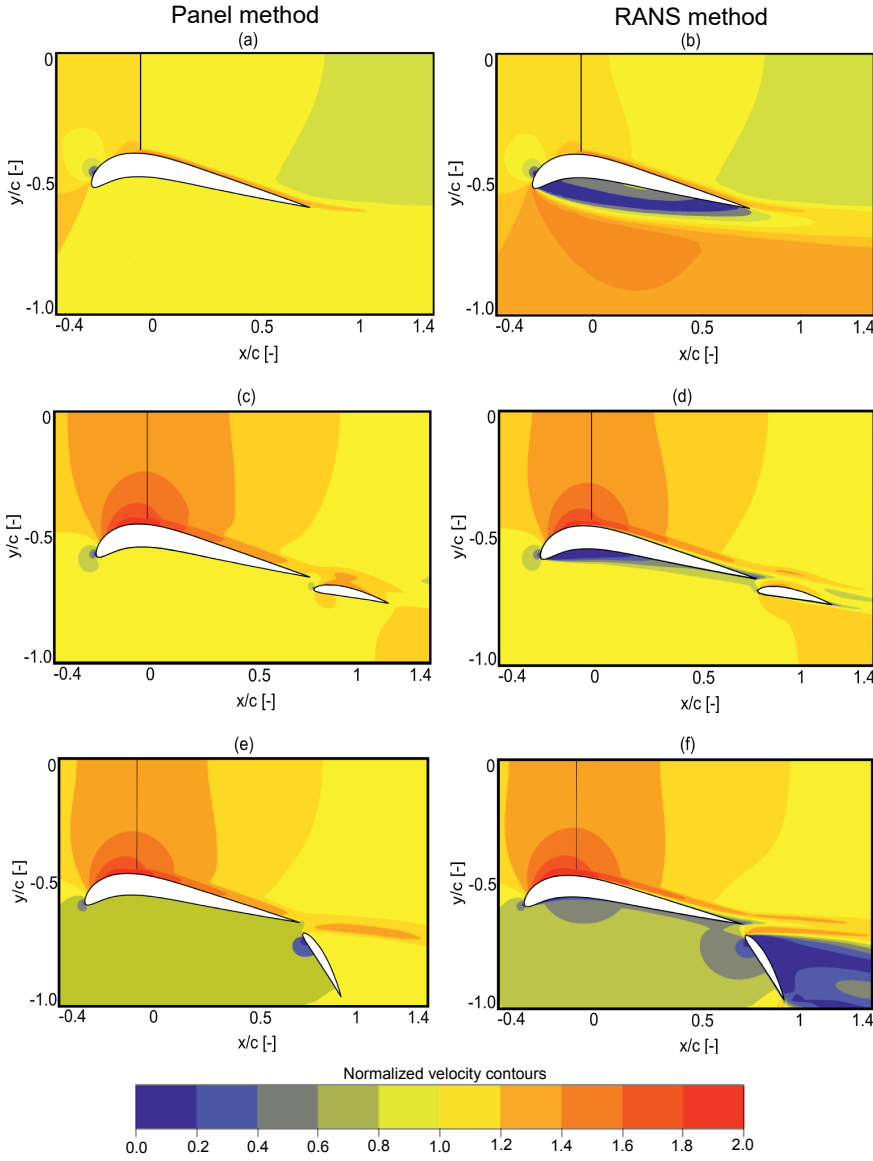


Figure 4.8: Velocity contours colored with normalized free-stream velocity obtained using: (a) panel method; no Flap, (b) RANS method; no Flap, (c) panel method; $\zeta = 5\%$ and $\theta = 10^\circ$, (d) RANS method; $\zeta = 5\%$ and $\theta = 10^\circ$, (e) panel method; $\zeta = 5\%$ and $\theta = 70^\circ$, and (f) RANS method; $\zeta = 5\%$ and $\theta = 70^\circ$.

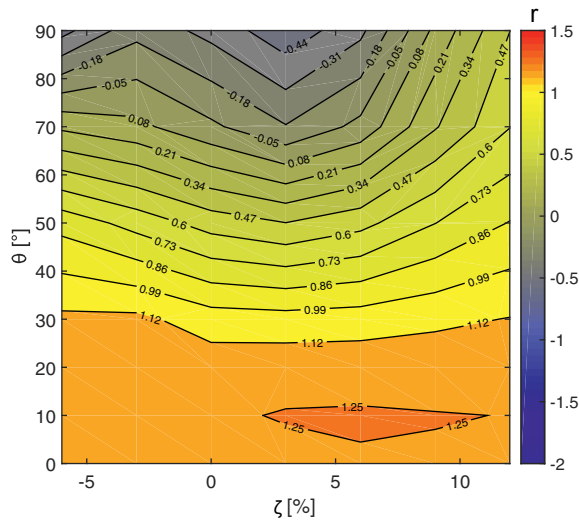


Figure 4.9: Effect of variable radial gap and the Flap deflection angle on the power augmentation factor using the panel method.

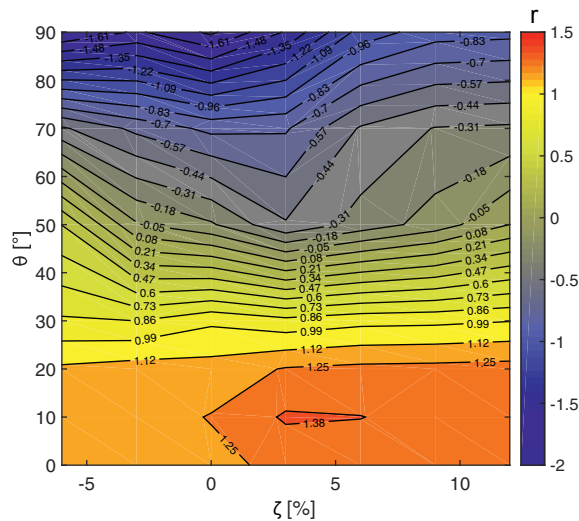


Figure 4.10: Effect of variable radial gap and the Flap deflection angle on the power augmentation factor using the RANS method.

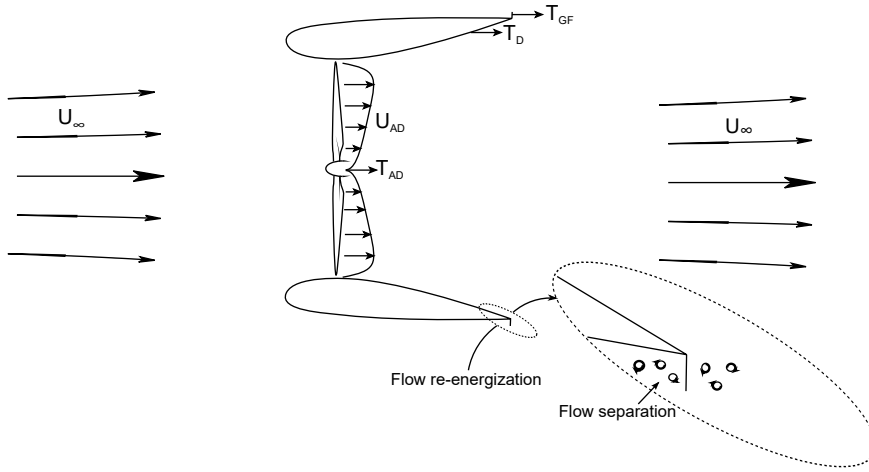


Figure 4.11: Schematic of flow around a DWT with a Gurney Flap attached to the duct trailing edge.

4.2. Gurney Flap

The aerodynamic analysis of DWT, hitherto, has clearly shown that duct thrust force coefficient C_{TD}^* is the major driver in improving the DWTs aerodynamic performance. To this aim, the effects of a Gurney Flap on the aerodynamic performance is studied. A Gurney Flap is a micro-tab retrofitted to the duct near the trailing edge on its pressure side as shown in Figure 4.11.

Goal of the current investigation is to study the characteristics of flow through and around an existing DWT model equipped with Gurney Flap. To this aim, DonQi[®] DWT model is used as the reference case. The rotor is modelled as an AD with radially uniform thrust coefficient C_{TAD} .

4.2.1. Experimental setup

A second experimental campaign was carried by Tang et al. [2016] following the one discussed in section 3.1. Gurney Flap measuring $2\%c$ is glued to the outer surface of the DonQi[®] duct using structural adhesives as shown in Figure 4.11 (c). Velocimetry data and pressure measurements, calculated without and with Gurney Flap, are used as reference. As stated in section 3.1, the AD position during the experimental setup is at $x/c = 0.28$ due to the design limitations. Differently, in the numerical setup, the AD is placed at the nozzle plane ($x/c = 0.2$).

4.2.2. Aerodynamic analysis

RANS method is chosen for the current analysis. A mesh independence study for the RANS method has been conducted considering three mesh sizes, where the refinement factor in each direction is approximately 1.5. In all cases, higher mesh density is defined in the region close to the surface of the Gurney Flap. The center-line axial velocity $\frac{U_X}{U_\infty}$ at a point location $12c$ downstream of the AD is taken as

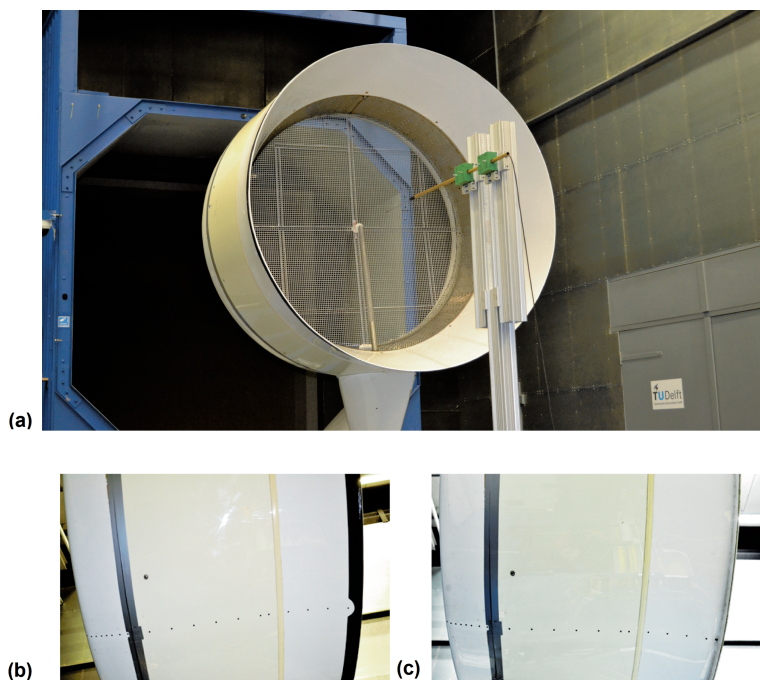


Figure 4.12: Pictures showing the experimental setup. (a) View of the entire setup with hot-wire anemometer placed on the traversing system. (b) and (c) show the duct without and with Gurney Flap respectively.

Table 4.3: Mesh statistics for mesh independence study of the DonQi[®] duct-AD model with 2% Gurney Flap.

Grid	Number of cells	$\frac{U_x}{U_\infty}$
Coarse	72539	0.6733
Medium	117709	0.6731
Fine	164322	0.6731

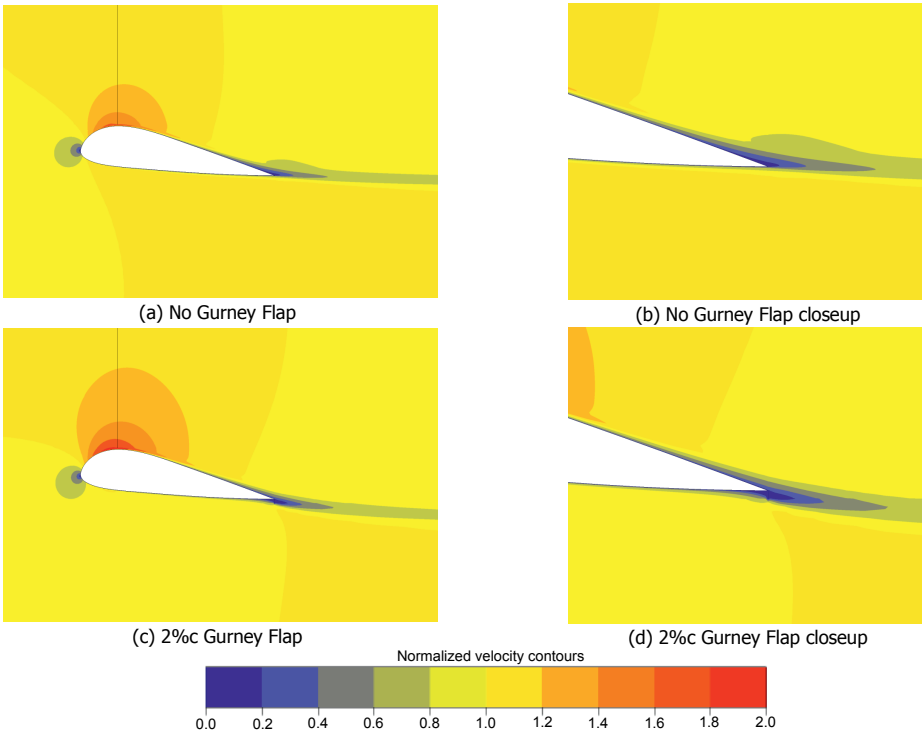


Figure 4.13: Velocity contours colored with normalized free-stream velocity around the duct-AD model with no Gurney Flap installed (a) and (b), and with 2%c Gurney Flap installed (c) and (d).

reference. The results of the mesh independence study are shown in Table 4.3. Convergence is reached for the medium refined mesh, and used for the simulations presented, hereinafter.

The effects of Gurney Flap on the flow field can be observed in Figures 4.13 (a)-(d), where contours of normalized free-stream velocity $\frac{U_x}{U_\infty}$ are reported. Results for the duct configuration without Gurney Flap are reported in Figures 4.13 (a) and (b), while the ones with Gurney Flap in Figures 4.13 (c) and (d). The interaction of the flow on the pressure side of the duct, as in Figures 4.13 (c) and (d), results in a visible flow separation region behind the Gurney Flap. For this case, it can be observed that, the velocity at AD plane is higher than the velocity found for the duct-AD model without Gurney Flap installed, as in Figures 4.13 (a) and (b). Furthermore, installation of Gurney Flap delays flow separation within the inner wall of the duct, thus being beneficial for the mass-flow rate increase through the AD.

Figures 4.14 and 4.15 shows the comparison of duct surface pressure coefficients c_p , for the duct configuration without and with Gurney Flap, respectively. The computed c_p shows trends in agreement with the experiments. The effect of the Gurney Flap on the duct wall c_p is visible both upstream and downstream of the AD. Most visible is the effect on the pressure side for x/c

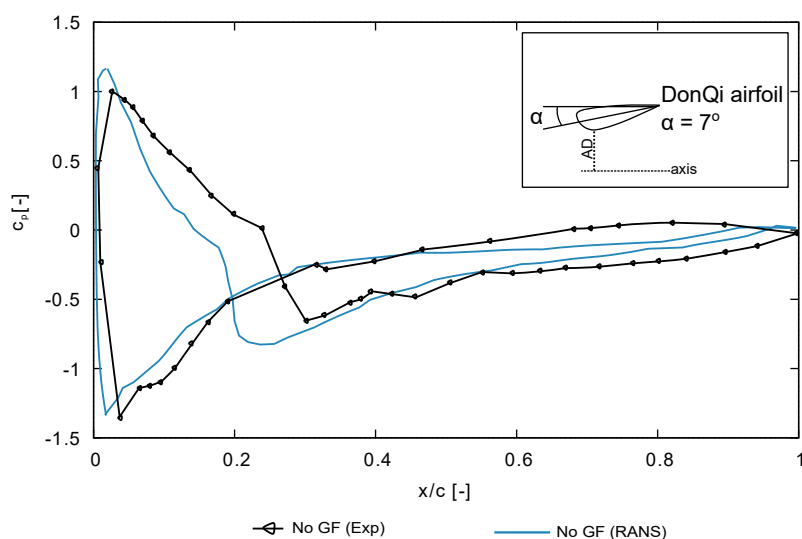


Figure 4.14: Comparison of duct wall pressure coefficients for duct without Gurney Flap.

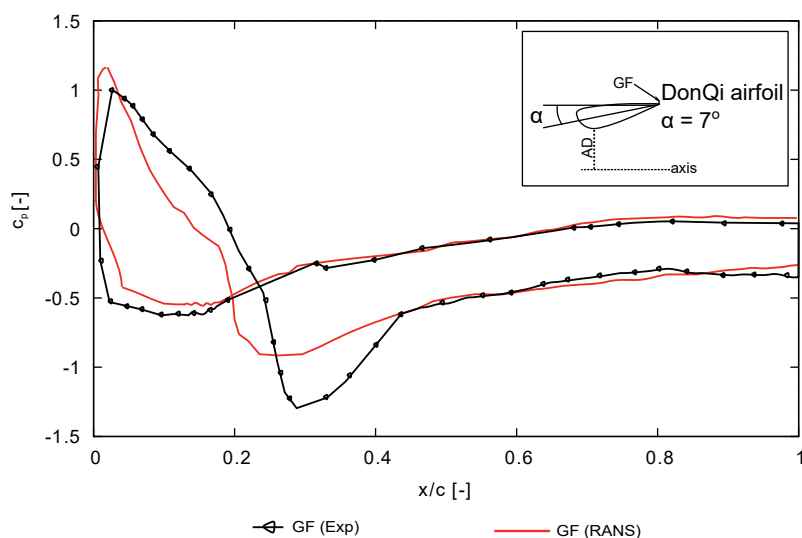


Figure 4.15: Comparison of duct wall pressure coefficients for duct with 2%c Gurney Flap.

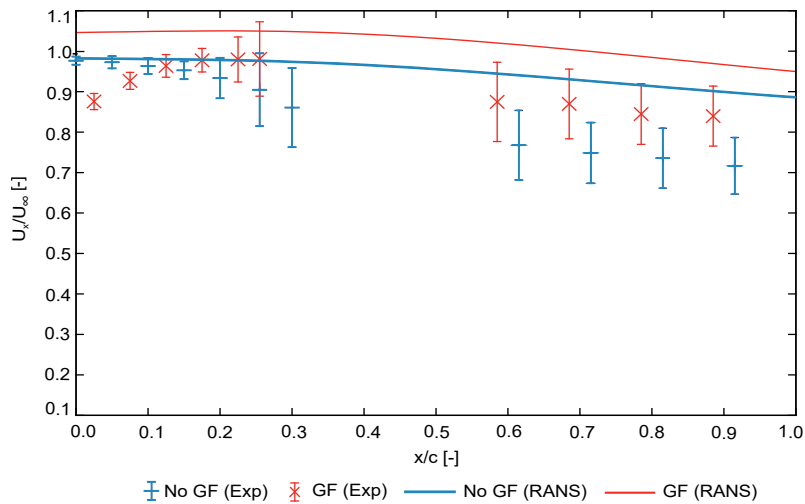


Figure 4.16: Comparison between CFD and experimental free-stream velocity distribution along the center-line for the duct-AD models.

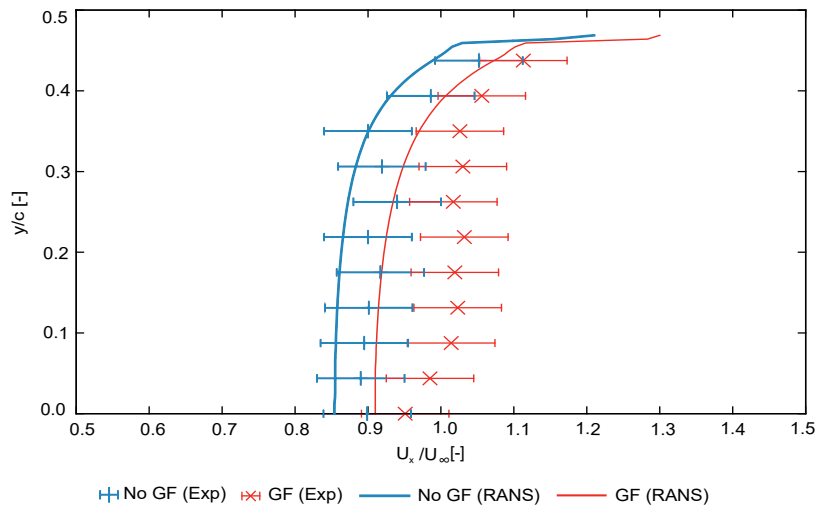


Figure 4.17: Comparison between CFD and experimental free-stream velocity distribution along the radial AD plane for the duct-AD models.

between 0.7 and 1, where the c_p rapidly become larger in the presence of Gurney Flap. Then the integral contribution of c_p , for the same airfoil angle of attack $\alpha = 7^\circ$, returns a higher duct thrust force coefficient C_{TD}^* (as in equation 2.20) for the DonQi[®] duct with Gurney Flap installed.

In Fig. 4.16 and 4.17, the comparison of the CFD results with the experimental data is reported in terms of axial and radial $\frac{u_x}{u_\infty}$ distribution, respectively. Error bars represent fluctuations measured during the experiments. The velocimetry measurements, especially in the region just upstream and downstream of the AD fluctuate because of the flow porous medium. CFD results in Figure 4.16 agree fairly with the experimental data where the maximum deviation of the CFD results from the experiments is 9% and 10.5% for the duct configuration without and with Gurney Flap, respectively. Similarly, velocity profiles along radial direction in Fig. 4.17 show a similar agreement with maximum deviation of 4% and 7% for the duct configuration without and with Gurney Flap, respectively. It is believed that the difference in AD location accounts to a significant extent for the deviation in the solutions comparison. Moreover, three-dimensional flow effects were not accounted in the two dimensional simulations. Nevertheless, the overall computed velocity trends are in good agreement with the experiment.

The increase in C_{TD}^* value with Gurney Flap installation, ultimately increasing the $\frac{u_x}{u_\infty}$ distribution in the AD radial plane, increases the C_p^* (see equation 2.21). Then, as per equation 2.17 and 2.22, the power augmentation factor $r = 0.99$ and 1.08, obtained for duct-AD model without and with Gurney Flap respectively.

4.3. Summary

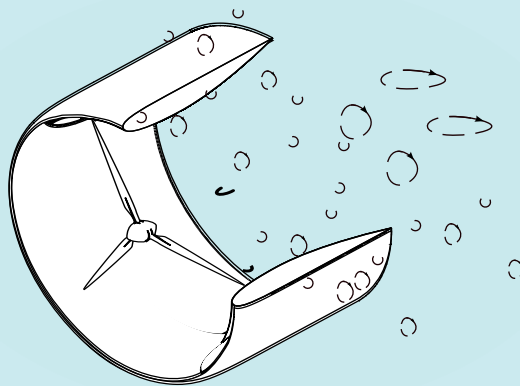
In this chapter, the effects multi-element duct and Gurney Flap on the aerodynamic performance of DWT are studied in detail. Based on the parametrization study presented in chapter 3 and recommendations from Igra [1981], the multi-element duct geometry consists of a DonQi D5 airfoil and a NACA 4415 airfoil for the duct and the Flap cross-sections, respectively. To validate the numerical methods, the present simulations are compared with experiments. In order to deepen the design principles of multi-element ducts, the effects of radial gap ζ and the Flap deflection angle θ on the global performance of DWT are investigated. Clear trends of the duct thrust force coefficients C_{TD}^* and the power augmentation factor r are observed across a range of multi-element duct configurations. An increase in the Flap deflection angle θ results in a decrease in C_{TD}^* , whereas, increase in the radial gap ζ shows an increase in C_{TD}^* . The analysis of flow field shows that flow separation in the multi-element duct inner wall increases for higher values of θ . This phenomenon determines the reduction in C_{TD}^* , and ultimately the augmentation factor r . As expected, the RANS method is more suitable for representing solutions for highly deflected Flap configurations. The viscous effects become stronger at higher Flap deflection angles, and the panel method is inherently incapable to take account for it.

Later, the effects of a Gurney Flap on the aerodynamic performance of the existing DonQi[®] duct-AD model are investigated using experiments and the RANS

approach. The RANS method is able to replicate the flow field through and around the duct-AD model. Trends obtained from RANS CFD agree well with the experimental data. Minor discrepancies in the values between RANS CFD and experiments are attributed to the different location of the AD and the three-dimensional flow effects not accounted in two-dimensional simulations. The analysis has shown the possibility to improve the existing DWTs aerodynamic performance with the addition of Gurney Flap retrofitted to the duct's trailing edge. Flow visualization using velocity contours shows that the Gurney Flap delay flow separation along the inner duct walls, and thereby increasing the DWTs aerodynamic performance. Comparing the two duct configurations, r is 8.5% higher with the application of Gurney Flap measuring $2\%c$ in comparison to the baseline DonQi[®] duct-AD model.

5

Effects of yawed inflow



5.1	Effects of yawed inflow: URANS study	77
	Numerical validation	77
	Aerodynamic performance	80
5.2	Effects of yawed inflow: LB-VLES study	84
	Numerical setup	84
	Numerical validation	85
	Flow field analysis	87
	Aerodynamic performance	95
	Noise estimation	96
5.3	Summary	99

This chapter is part of the following publications:

V. V. Dighe., D. Suri., F. Avallone., & G.J.W. van Bussel., Ducted wind turbines in yawed flow: A numerical study. *Manuscript submitted for publication in Wind Energy Science*.

V. V. Dighe., F. Avallone., & G.J.W. van Bussel., (2020) Effects of yawed inflow on the aerodynamic and aeroacoustic performance of ducted wind turbines. *Journal of Wind Engineering and Industrial Aerodynamics*, 201, 104174.

*Design is a process for making things right,
for shaping what people need.*

Ralph Caplan

5

The investigation, hitherto, has made significant advancements in improving the aerodynamic performance of the DWT. Since DWTs are installed close to urban areas, they are subject to non-uniform flows caused by the presence of buildings or other surface discontinuities. For this reason, the aerodynamic performance of DWTs in yawed inflow condition must be characterized. This chapter aims to make a significant contribution to this.

Integration of DWTs into urban environments would necessitate the reduction or the mitigation of noise from these devices. For this reason, an estimate of the aeroacoustic noise from DWT models is quantified using the Ffowcs Williams-Hawkings (FWH) acoustic analogy.

The chapter examines in two parts the effects of yawed inflow condition on the aerodynamic and aeroacoustic performance of two DWT models. In section 5.1, aerodynamic calculations are shown using two-dimensional URANS simulations. Later, in section 5.2, aerodynamic and aeroacoustic calculations of three dimensional DWT models are presented using LB-VLES simulations. Finally, the most relevant results are summarized in section 5.3.

5.1. Effects of yawed inflow: URANS study

In the following section, the effects of yawed inflow condition on the aerodynamic performance of the DWT is investigated. As identified earlier [Igra, 1981], asymmetric and unsteady flow effects become dominant in yawed inflow and hence URANS method, described in section 2.2.3, is chosen for the current investigation. Section 5.1.1 reports the validation of the numerical method with the experimental data. Insights on the aerodynamic performance coefficients under yawed inflow is discussed in section 5.1.2, together with flow analysis.

5.1.1. Numerical validation

For validating the numerical approach, the experiments reported by Igra [1981] are simulated. Igra's experiments were conducted in the subsonic wind tunnel of the Israel Aerospace Industry (formerly Israel Aircraft Industry); this tunnel has a large test section and it measures 3.6 m (length) \times 2.6 m (breadth).

A schematic of the cross-section geometry is shown in Figure 5.1(a). The longitudinal cross-section of the duct is a NACA 4412 airfoil. The leading edge of

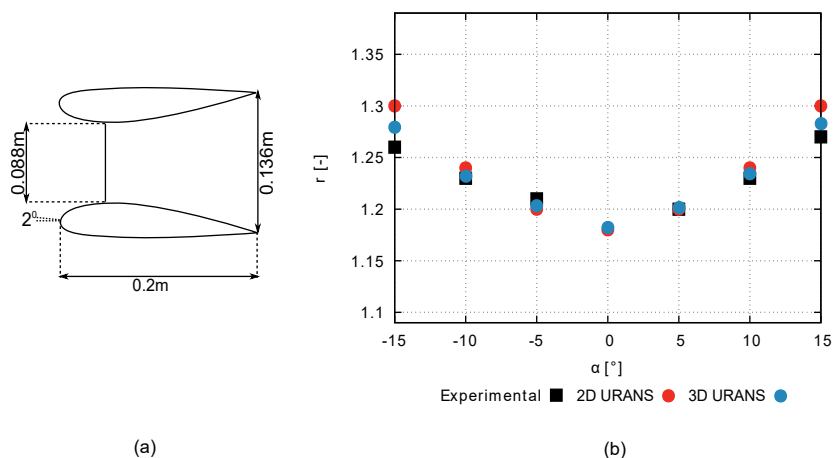


Figure 5.1: A schematic cross-section layout of the three dimensional experimental model used for the numerical validation study (a), and comparison between experimental findings [Igra, 1981] and the CFD results (b).

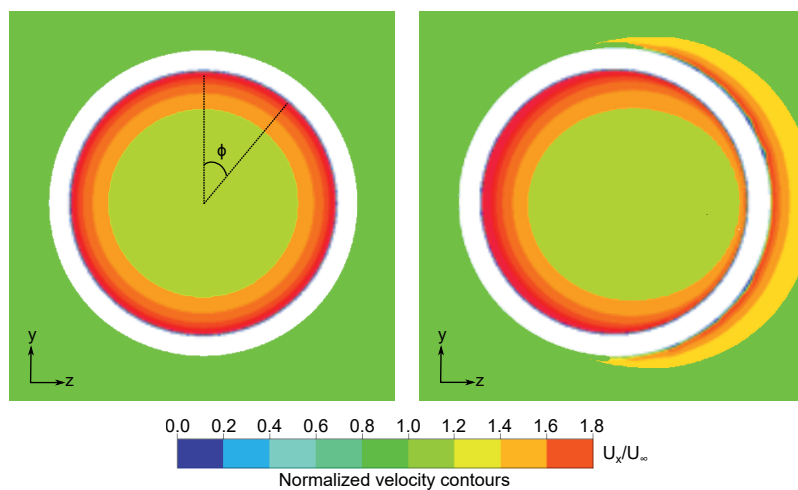


Figure 5.2: Contours of time-averaged non-dimensional free-stream velocity U_x/U_∞ computed at the AD location located in the $y-z$ plane for Model B in (left) non-yawed inflow and (right) yawed inflow, $\alpha = 10^\circ$.

the duct is rotated by 2° with respect to the free-stream direction, resulting in a duct exit-area-ratio $\frac{S_{exit}}{S_{AD}} = 1.54$. A uniformly loaded AD model with $C_{TAD} = 0.434$ is used to represent the turbine. The experimental data set consists of static pressure distributions at different axial and radial positions, and forces generated on the duct surface for a range of flow angles. As a matter of fact, the yawed inflow condition for the DWT model is achieved by rotating the DWT model relative to the wind direction aligned at zero degree. During the experiments, the inflow velocity was set at $U_\infty = 32$ m/s corresponding to $Re \approx 4.5 \times 10^5$. Following Igra [1981], the wall interference and wind tunnel blockage can be ignored. The experimental data is reported in terms of the augmentation factor $r = \frac{C_p}{C_{p0}}$, as in equation 2.17.

To assess the validity of the 2D approach, 3D simulations are also performed, also based on URANS equations. The numerical settings for 3D URANS are identical to the one discussed in section 2.2.3. A good agreement between the CFD simulations and the experimental findings is found, see Figure 5.1(b). The deviation between the CFD and the experimental findings increase with increasing values of α , especially for 2D URANS calculations.

The differences in the 2D and 3D CFD results can be explained by looking at the flow-field obtained using 3D URANS simulations. Figure 5.2 shows the time-averaged velocity contours of non-dimensional axial velocity $\frac{u_x}{U_\infty}$ in the $y-z$ plane at the AD location for Model B in non-yawed (left) and yawed (right) inflow conditions. Time averaging is performed after convergence is reached. Because of the yaw angle ($\alpha = 10^\circ$), an asymmetric flow-field is present, thus the velocity at the AD plane changes with the azimuthal angle Φ . Here, the azimuthal angle Φ is defined as positive in the clockwise direction when looking from upwind, with zero when oriented in the positive y direction, see Figure 5.2 (left). The main difference between the CFD results is due to fact that the C_p obtained from 3D URANS simulations uses the azimuthally averaged streamwise velocity component, while the results from 2D simulations do not account for the gradual variation with Φ . However, as shown in the comparison, the three dimensional azimuthal effects are negligible when comparing the global trends of r . Although 3D URANS simulations increase the level of unsteady flow-field description due to the duct-AD interaction, the computational cost of 3D URANS simulation is four times larger than the 2D URANS. It is found that the maximum deviation between 2D URANS results and experimental findings is less than 3.5% for $\alpha = 15^\circ$. Having said that, 2D URANS approach is considered to be acceptable for the initial stages of yawed inflow study. Moreover, the computing cost issued by going from 2D URANS to 3D URANS does not justify the scope of the current investigation, where the effects of distributed AD loading, wake rotation and divergence are totally ignored.

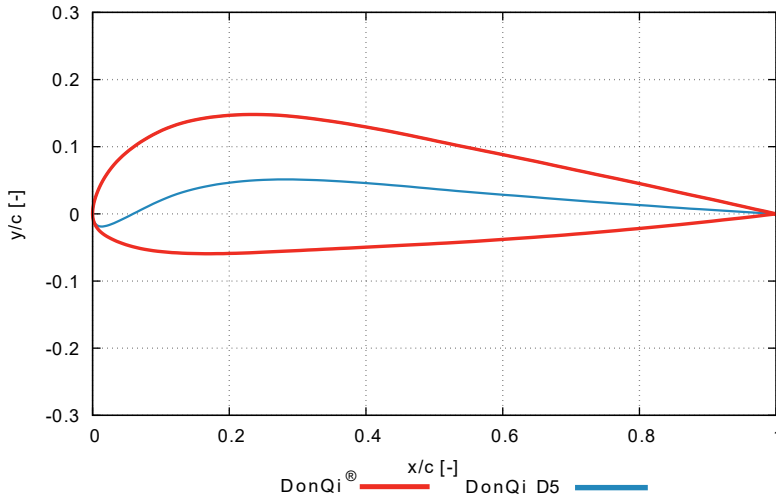


Figure 5.3: Duct geometries (cross-section) used for the numerical study.

5

5.1.2. Aerodynamic performance

Duct force coefficient

In the following sections, the effects of yaw on the aerodynamic performance of the duct-AD model are quantified. Two duct geometries, DonQi® and DonQi D5 are chosen. The selection is based on the duct shape parametrization study conducted in chapter 3. In the study, an optimal $C_{TAD} = 0.7$ was obtained for both the duct geometries (see Figure 3.10 and 3.11). Hence, this value is employed for the rest of the discussion.

Figure 5.4 illustrates the variation of duct force coefficient C_{TD} as a function of yaw angle α obtained for the two duct geometries. C_{TD} trend-lines are obtained using the results from thirteen simulations ranging from $\alpha = 0-30^\circ$ in increment of 2.5° . Starting with the trend-line for DonQi® duct, it can be observed that, C_{TD} decreases with increasing values of α . Conversely, for DonQi D5 duct, C_{TD} increases with increasing values of α . A local C_{TD} maximum at $\alpha = 17.5^\circ$ appears for the DonQi D5 duct. The value of C_{TD} for DonQi D5 duct decreases for α beyond the local maximum.

The differences in the C_{TD} trend-lines for the two duct geometries can be explained by looking at the flow-field. Contours of non-dimensional free-stream velocity $\frac{U_x}{U_\infty}$ for both duct geometries are reported in Figures 5.5 and 5.6. Contours are plotted on a plane close to the surface of the duct thus allowing a better interpretation of the flow field associated with duct-AD interactions. Four yaw angles, i.e. $\alpha = 0^\circ, 10^\circ, 17.5^\circ$ and 20° , are shown. The reason for choosing the specific angles is to allow a better interpretation of the flow field associated with the C_{TD} trend-lines (local maximum) seen in Figure 5.4. The contours of DonQi® model show that, with increasing values of α , the magnitude of velocity on the suction side of the upstream duct decreases and the magnitude of velocity

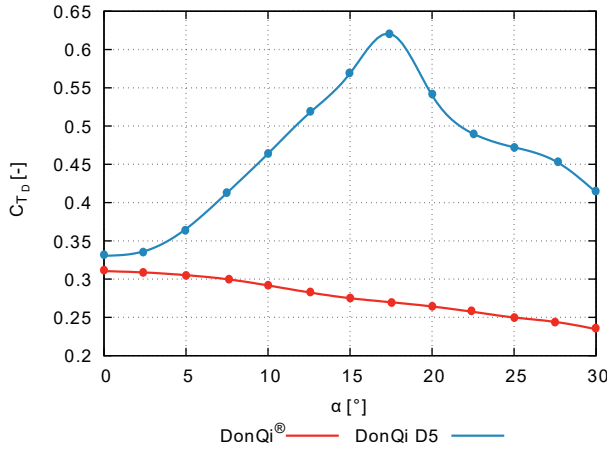


Figure 5.4: Effect of yawed inflow on the duct thrust force coefficient for the two duct geometries. $C_{T,AD} = 0.7$.

on the pressure side of the downstream duct starts to increase significantly. With the reduced velocity, there is insufficient boundary layer momentum for the flow to remain attached on the suction side of the upstream duct. Subsequently, at $\alpha = 20^\circ$, the flow is completely separated from the upstream duct's inner surface, thus indicating duct stall. Inner duct wall flow separation is characterized by a strong reduction of duct wall shear stress, and ultimately the reduction of C_{T_D} with increasing values of α for the DonQi® model in Figure 5.5. For the DonQi D5 model, however, increased yaw returns higher velocity magnitude on the suction side of the duct up to $\alpha = 17.5^\circ$. This is due to the duct profile camber, which promotes flow acceleration due to the reduced pressure on the suction side of the duct. The increased velocity magnitude on the suction side of the duct in this range is always accompanied by flow separation on the pressure side of the duct. As long as the flow separation is limited on the pressure side of the duct, the integral of duct thrust force coefficient C_{T_D} in Figure 5.4 increases up to $\alpha = 17.5^\circ$. At $\alpha = 20^\circ$, the flow separation region traverses from the pressure side to the suction side of the duct indicating duct stalling characterized by the reduction of C_{T_D} in Figure 5.4.

Power Coefficient

Figure 5.7 represents the power coefficient C_p (see equation 2.14), for the two duct-AD models, as a function of yaw angle α . For the sake of completeness, C_{p_o} for a bare AD, as in equation 2.6, is plotted alongside. The figure shows that, C_p is higher than C_{p_o} for all values of α . Comparing Figures 5.4 and 5.7, the C_p trends corresponds with the C_{T_D} trends. The larger the C_{T_D} , the higher the C_p reached, and vice-versa. Similar to the C_{T_D} trend for DonQi D5, a maximum $C_p \approx 0.84$ is obtained at $\alpha = 17.5^\circ$; thereafter any further increase in α results in the reduction of the C_p values.

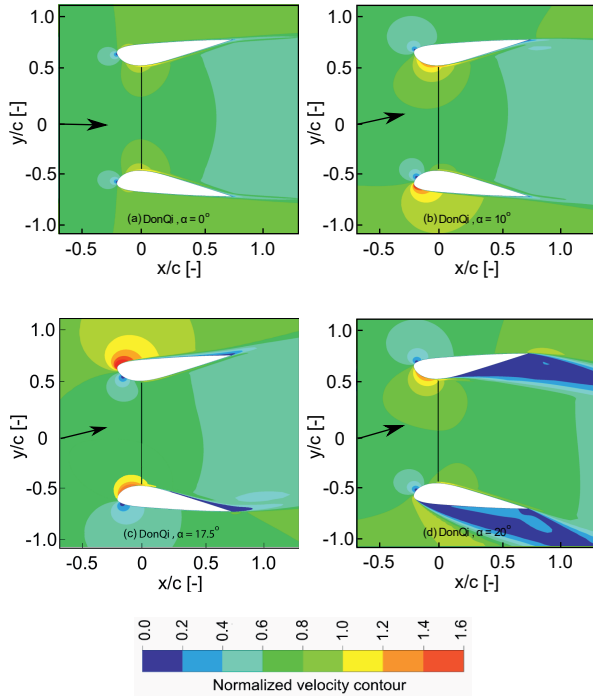


Figure 5.5: Velocity contours colored with streamwise normalized velocity. The results are depicted for DonQi[®] duct-AD model bearing a constant $C_{TAD} = 0.7$. The arrow indicating the inflow direction.

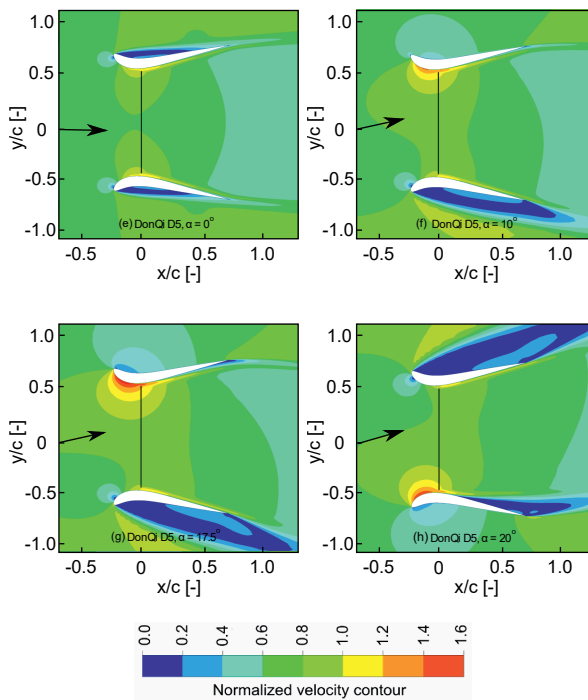


Figure 5.6: Velocity contours colored with streamwise normalized velocity. The results are depicted for DonQi D5 duct-AD model bearing a constant $C_{TAD} = 0.7$. The arrow indicating the inflow direction.

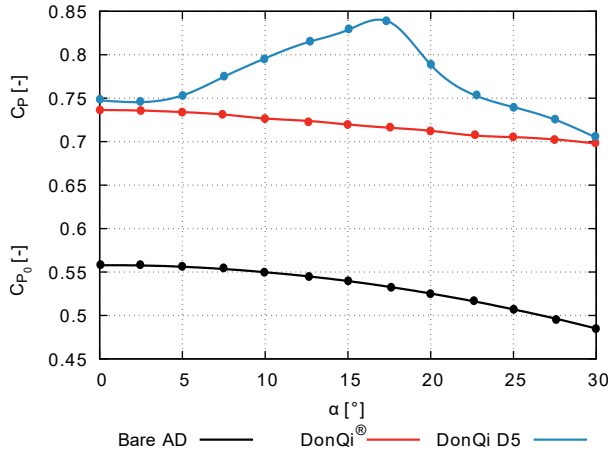


Figure 5.7: Effect of yawed inflow on the power coefficient.

5

5.2. Effects of yawed inflow: LB-VLES study

In the following section, the effects of yaw on the aerodynamic and aeroacoustic performance of the DWT models are studied using full scale three-dimensional simulations. For the current investigation, LB-VLES simulations, described in section 2.2.4, are performed. Section 5.2.1 details the geometric parameters of the DWT models. Flow-field analysis is presented in section 5.2.3. Insights on the aerodynamic and aeroacoustic performance coefficients for the two DWT models, both under non-yawed and yawed inflow conditions, are discussed in sections 5.2.4 and 5.2.5 respectively.

5.2.1. Numerical setup

Based on the URANS study discussed in section 5.1, DonQi[®] and DonQi D5 are chosen for the current investigation, see Figure 5.8. It was found that the DonQi D5 duct-AD model shows improvement in C_p up to at a yaw angle $\alpha = 17.5^\circ$. The duct chord c is 1 m. At the inlet, $R_{inlet} = 0.87$ m, at the outlet $R_{outlet} = 1$ m and at the throat $R_{throat} = 0.77$ m.¹ The tip clearance between the duct and the turbine blade equals 0.02 m.

Based on the previous study [Avalone et al., 2020], the DonQi[®] wind turbine model is used. The wind turbine consists of three blades with a NACA 2207 airfoil of chord length varying from 0.13 m at the root section to 0.105 m at the tip. The blade twist angle varies from 40.5° at the root to 0.3° at the tip section. The wind turbine blades are connected to a hub and there is a streamlined nacelle flush with the outer diameter of the hub. The hub is composed of a cylinder, with diameter and length equal to 0.125 m and 0.1 m, respectively. Similarly, the nacelle has the cylinder length equal to 0.1 m and the diameter equal to 0.075 m.

¹It is important to note that the R_{throat} in URANS and LB-VLES simulations are different in dimension, and therefore not suitable for direct comparison.

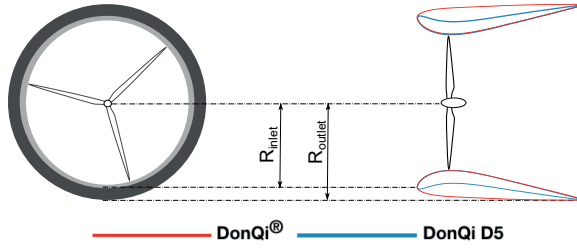


Figure 5.8: Front view of the DWT models (left) with the cross-section view detailing the geometric parameters of the two duct profiles (right).

For the turbine, the rotational speed ω is set at 39.84 rad/sec, the calculated value for a tip-speed ratio $\lambda = 6$; this value is found optimal based on the previous study [Ten Hoopen, 2009]. The free-stream velocity $U_\infty = 5$ m/s, which is a typical value for urban wind turbines, corresponding to Reynolds number $Re = 3.31 \times 10^5$ based on the duct chord length c . To establish yawed inflow conditions, the DWT model is rotated around the center-line axis by yaw angle α . A LB-VLES simulation is run for 9 complete turbine rotations corresponding to a physical time of 1.42 seconds. The simulations are performed using High-performance computing facility available at The Delft University of Technology requiring 7200 CPU hrs/rotation on a Linux Xeon E5-2690 2.9 GHz platform.

5.2.2. Numerical validation

First, a mesh independence study is performed for the two DWT models in non-yawed inflow condition by uniformly increasing the resolution of each VR. Three resolution cases, corresponding to the smallest voxel size equal to 1200 (coarse), 1800 (medium) and 2400 (fine) voxels per duct chord, are studied. The duct thrust force coefficient C_{TD} and the total thrust force coefficient C_T for the DWT models are taken as reference for the convergence analysis. They are defined as:

$$C_{TD} = \frac{T_D}{\frac{1}{2}\rho U_\infty^2 S_{turbine}}, \quad (5.1)$$

$$C_T = \frac{T}{\frac{1}{2}\rho U_\infty^2 S_{exit}}, \quad (5.2)$$

where T_D is the duct thrust force, i.e. the axial force, generated by the duct surface, $S_{turbine}$ is the turbine surface area equal to $\pi R_{turbine}^2$, T is the total thrust force, i.e. the axial force, generated by the DWT model and S_{exit} is the duct exit surface area equal to πR_{exit}^2 .

The results of the mesh independence study are shown in Table 5.1. Solution convergence is reached for the medium VR, when the observed deviations between the converged values are less than 0.5%. The medium VR mesh is adopted for the rest of the discussion.

Table 5.1: Voxels statistics for mesh independence study of the DWT models.

	Coarse	Medium	Fine	Experiments
Number of voxels	1.46×10^6	2.67×10^6	4.33×10^6	
DonQi [®] C_{TD}	0.410	0.417	0.419	
DonQi D5 C_{TD}	0.460	0.471	0.471	
DonQi [®] C_T	0.612	0.703	0.706	0.689
DonQi D5 C_T	0.642	0.723	0.727	

5



Figure 5.9: Front view of the DonQi[®] DWT model used for the experimental study [Ten Hoopen, 2009].

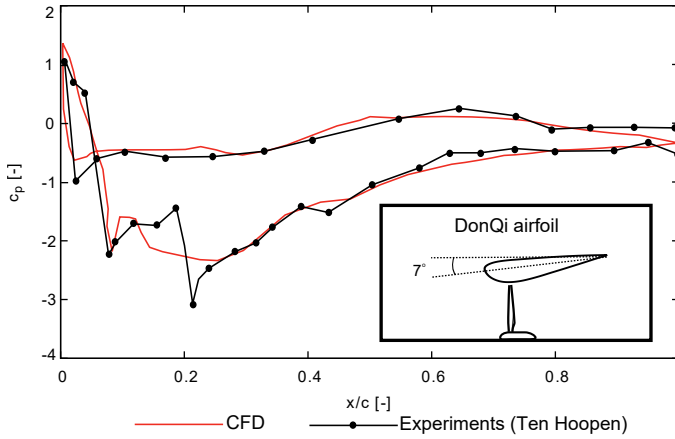


Figure 5.10: Comparison of duct surface pressure coefficient c_p between the experimental data and the CFD findings shown for DonQi® DWT model in non-yawed inflow condition.

5

As further validation of the numerical approach, numerical results are compared with the experimental ones reported by Ten Hoopen [2009] who investigated the DonQi® DWT model in non-yawed inflow condition (see Figure 5.9). Experiments were conducted in the closed-loop open-jet (OJF) wind tunnel facility at the Delft University of Technology. Ten Hoopen [2009] measured the total thrust force exerted by the DonQi® DWT model using an axial force balance system. The C_T calculated from the wind tunnel measurements is 0.689 while by CFD it is 0.703; see Table 5.1. The numerical and experimental results differ by 2%, which is within the experimental uncertainty [Ten Hoopen, 2009].

The duct surface pressure distribution, measured in the experiments using pressure taps arranged along the duct chord length, is compared with the numerical one in Figure 5.10. In the figure, the duct surface pressure coefficient c_p is plotted as a function of normalized duct chord length x/c . Results from CFD are obtained by azimuthally averaging the c_p values over two complete turbine rotations after reaching temporal convergence and the solutions reaching a quasi-steady state. Overall, a very good agreement for the c_p values between the CFD data and the experimental results is found. The noise damper is not flush mounted inside the duct, which is a production inaccuracy (see Figure 5.9). This causes the pressure jump in the measured pressure distribution. The noise damper geometry is not included in the numerical model, hence the deviation in the c_p values at $x/c = 2$ are observed.

5.2.3. Flow-field analysis

The instantaneous flow-fields around the two DWTs, both in non-yawed and yawed inflow conditions, are shown in Figures 5.11 and 5.12 respectively, using the λ_2 criterion for vortex identification [Jeong and Hussain, 1995] color-contoured with the normalized streamwise velocity magnitude.

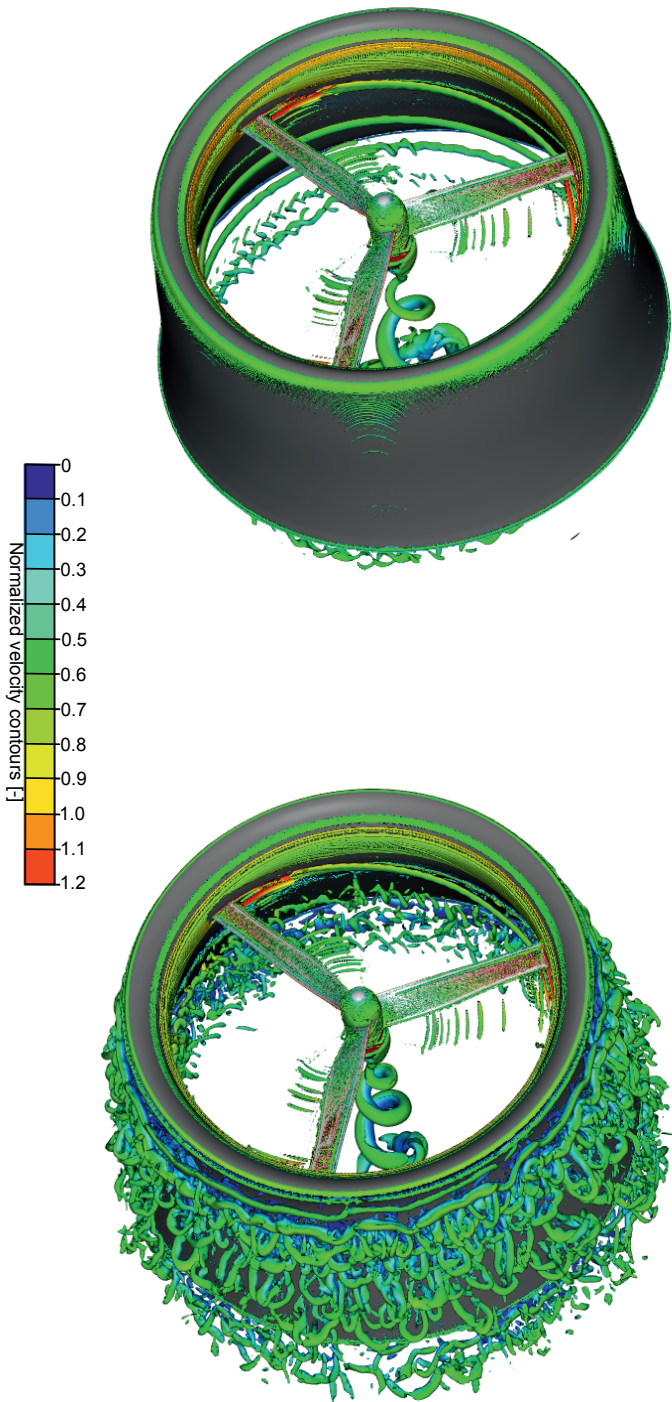


Figure 5.11: Visualization of the instantaneous flow-fields using iso-surface of the λ_2 criterion for vortex identification colored-contoured with normalized streamwise velocity component U_x/U_∞ for (left) DonQi® model at $\alpha = 0^\circ$ and (right) DonQi D5 model at $\alpha = 0^\circ$.

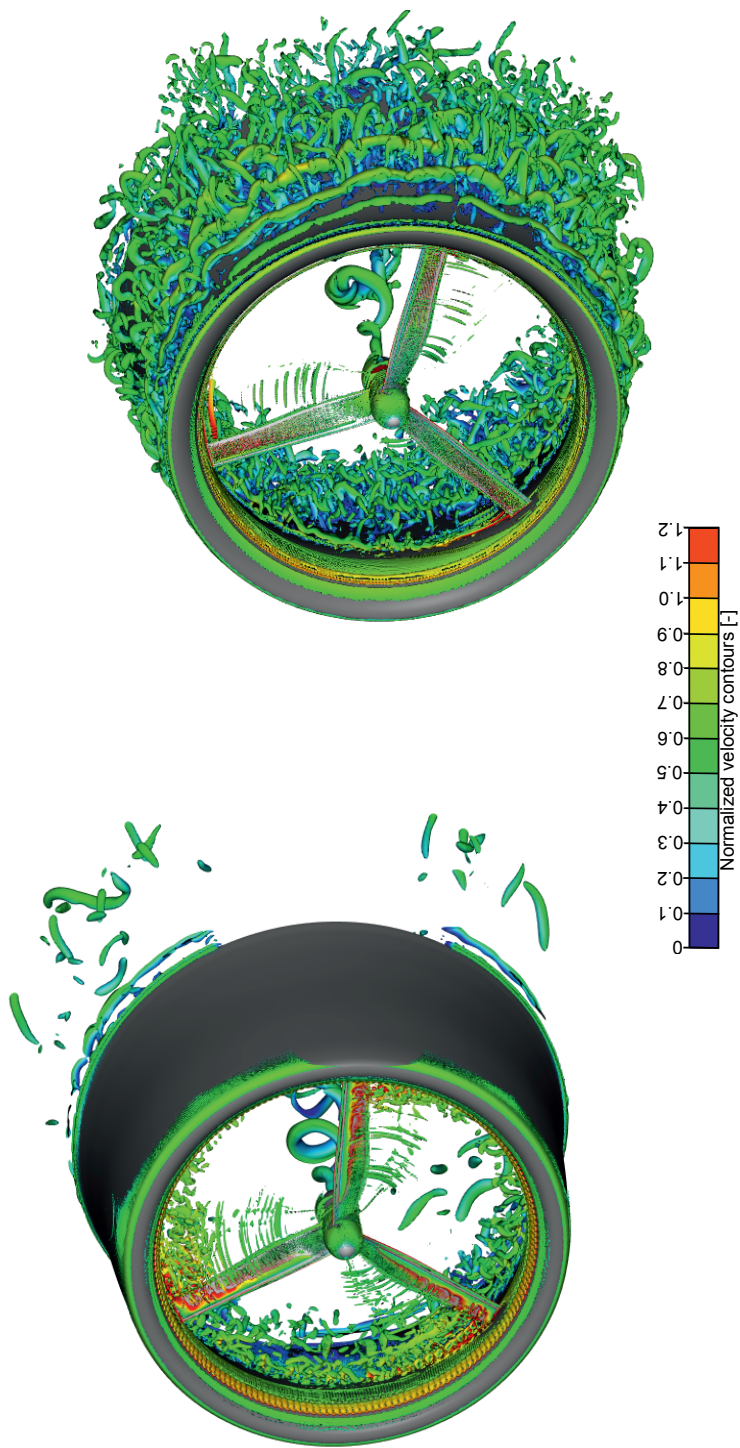


Figure 5.12: Visualization of the instantaneous flow-fields using iso-surface of the λ_2 criterion for vortex identification colored-contoured with normalized streamwise velocity component u_x/U_∞ for (left) DonQi[®] model at $\alpha = 7.5^\circ$ and (right) DonQi D5 model at $\alpha = 7.5^\circ$.

For the DonQi[®] configuration at $\alpha = 0^\circ$, as in Figure 5.11 (left), tip vortices convecting over the inner walls of the duct are clearly visible. These vortices, convect in the duct following a helicoidal pattern, become unstable and break up in smaller structures towards the exit plane of the duct [Avallone et al., 2020]. By increasing the camber of the duct cross section, as in Figure 5.11 (right), a larger flow acceleration is present along the suction side of the duct. This has an effect on the local boundary layer thickness at the turbine plane, thus changing the ratio between the tip-clearance and the boundary layer thickness. In this case, the boundary layer thickness is thicker than that observed for the baseline case, and, as a consequence, the tip vortex breaks at the turbine plane with generation of turbulent flow structures along the duct inner walls. A similar phenomenon was observed in a previous study by Avallone et al. [2020] on the baseline DWT geometry by changing the tip-clearance of the blades. Focusing on the duct pressure side, large coherent structures are formed at the leading edge of the DonQi D5 model, which convect and break into smaller ones at more downstream locations. This is caused by the fact that the curvature of the DonQi D5 duct is larger than the baseline duct and the transition to turbulence is anticipated.

By introducing a yaw angle, as in Figures 5.12, the flow-fields, for both configurations, show differences in the turbulent flow structures convecting over the inner walls of the duct. A major difference between the two configurations is that, for the baseline configuration, the tip vortex is generated at the turbine plane and interact with the duct surface at downstream locations where it breaks in smaller structures. Differently, for the DonQi D5 configuration, as for the case with zero yaw angle, the tip vortex breaks at the turbine plane. For this case, the flow is richer of turbulent flow structures, and it decelerates more just downstream of the turbine plane as visible from the blue contour representing normalized streamwise velocity component. For this particular case, the yawed inflow causes an early breakdown of the main vortex into smaller structures on the pressure side of the duct and, as expected, are subject to larger radial spreading away from the surface of the duct.

To better show the aerodynamic interactions between the near wake of the turbine and the turbulent boundary layer convecting over the duct surface, 2D visualization in the x - y plane of the instantaneous flow-fields are shown in Figures 5.13 and 5.14. As in the previous figures, non-dimensional contours of the streamwise velocity components U_x/U_∞ are plotted.

For all the cases, it can be observed that, as expected, the velocity at the turbine plane is higher than the free-stream velocity. As discussed in chapter 1, this is due to the airfoil-shaped duct, which acts as a convergent-divergent nozzle that accelerates the flow (i.e., increases the mass-flow rate). The velocity in the plane of rotation varies in the radial direction with the maximum velocity observed towards the tip region of the turbine blade [Avallone et al., 2020]. Here, the tip gap between the duct and turbine accelerates the flow via a mechanism similar to boundary layer blowing [Avallone et al., 2020, Kwong and Dowling, 1994].

For the baseline DonQi[®] model at zero degree yaw angle (Figure 5.13 (left)), the flow over the suction side of the duct (i.e., the inner wall) weakly separates at

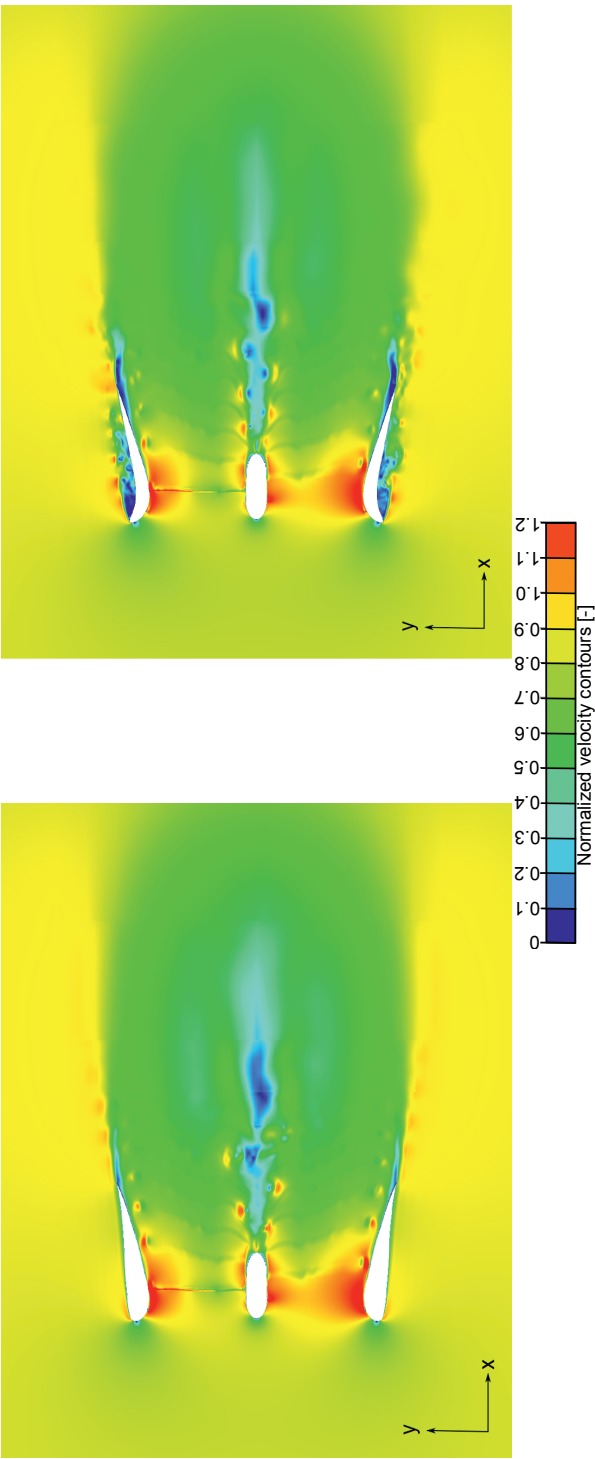


Figure 5.13: Contours of instantaneous streamwise velocity u_x/u_∞ in the $x-y$ plane for (left) DonQi[®] model at $\alpha = 0^\circ$ and (right) DonQi D5 model at $\alpha = 0^\circ$.

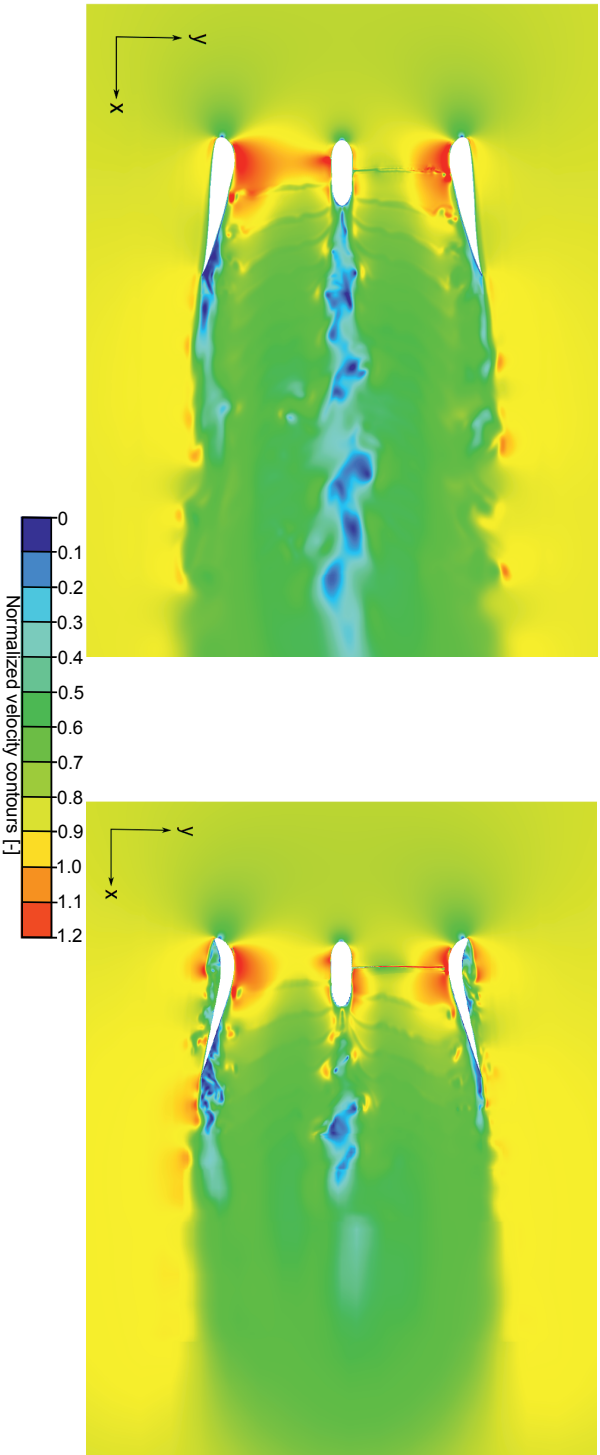


Figure 5.14: Contours of instantaneous streamwise velocity U_x/U_∞ in the $x-y$ plane for (left) DonQi® model at $\alpha = 7.5^\circ$ and (right) DonQi D5 model at $\alpha = 7.5^\circ$.

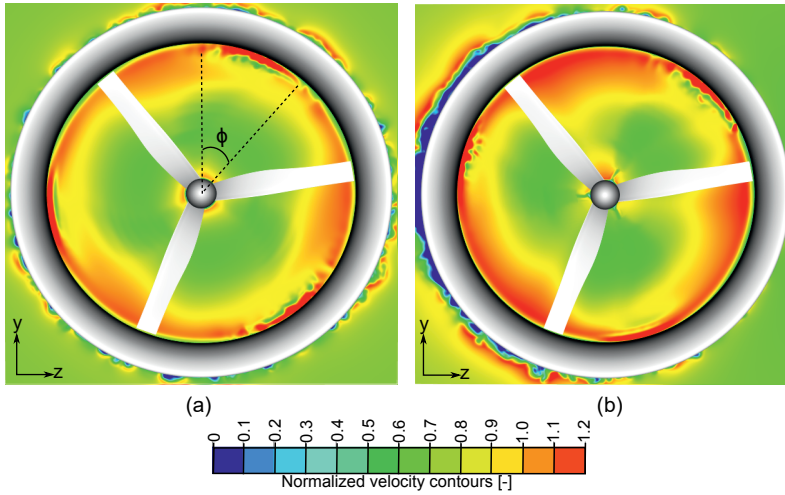


Figure 5.15: Contours of instantaneous streamwise velocity U_x/U_∞ in the $y-z$ plane for DonQi D5 in (a) non-yawed and (b) yawed inflow condition.

5

about the 95% of the duct chord length. This is visualized by the low velocity region close to the trailing edge. For the same inflow condition, DonQi D5 model shows earlier flow separation starting from 85% of the duct chord length over the suction side (Figure 5.13 (right)). For this particular case, the velocity slows down on the pressure side of the duct due to the higher duct curvature. As a result, pressure drops on the suction side of the duct and increased mass flow is swallowed by the turbine as explained in chapter 3. Figures 5.13 (left) and (right) give further insights on the breaking up process of the tip vortex in smaller vortical structures. For the baseline configuration, there is a weak interaction between the boundary layer convecting over the inner walls of the duct and the tip vortex. As a matter of fact, footprints of the tip vortices are clearly visible within the duct. For the DonQi D5 model, the footprints of the vortices are weaker since they interact with the separated boundary layer.

The baseline configuration with yawed inflow (Figure 5.14 (left)) shows that flow separation moves upstream; the resulting thicker boundary layer interacts with the tip vortex thus breaking up in smaller structures. These velocity fluctuations in the near wake resembles the vortex dynamics breakdown for HAWTs in yaw, thus reducing the overall thrust generated by the turbine blades [Jiménez et al., 2010]. For the DonQi D5 model in yawed inflow (Figure 5.14 (right)), the separation location within the duct weakly changes with respect to the zero-yaw configuration.

Figure 5.15 shows instantaneous contours of $\frac{U_x}{U_\infty}$ in the $y-z$ plane at the turbine location for the DonQi D5 model in non-yawed (Figure 5.15 (a)) and yawed (Figure 5.15 (b)) inflow conditions. The presence of a yaw angle causes an asymmetric flow-field, thus the velocity at the turbine plane changes with the azimuthal angle Φ . Similar to Figure 5.2, the azimuthal angle Φ is defined as rotating clockwise when

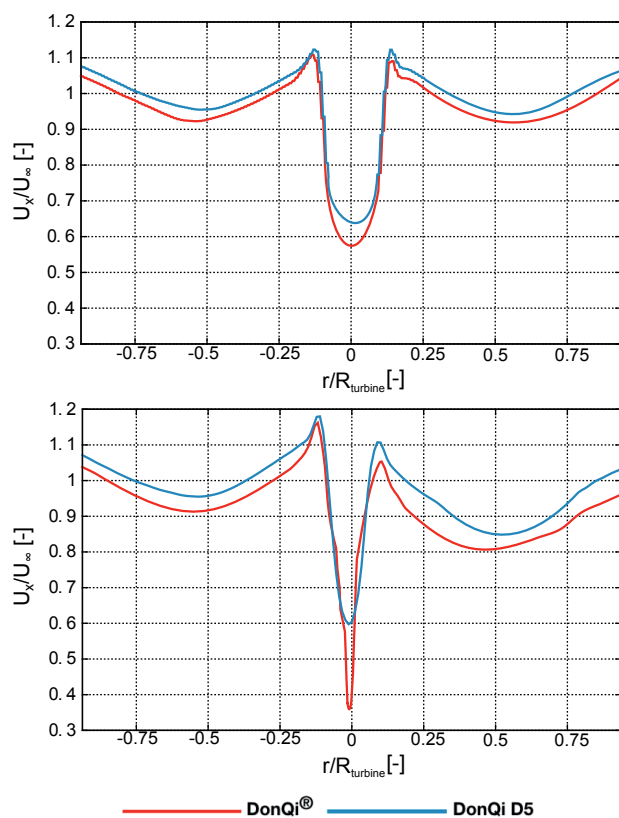


Figure 5.16: Radial distribution of azimuthally averaged streamwise velocity U_x/U_∞ measured at the turbine plane for the non-yawed inflow (top) and yawed inflow (bottom).

looking upwind, with zero aligned in the positive y direction (see Figure 5.15 (a)). The figure highlights the higher velocity at the turbine plane for the yawed inflow configuration. This is quantified by plotting the azimuthally averaged streamwise velocity component in the radial direction ($r/R_{turbine}$) in Figure 5.16. The DWT with larger camber cross-section airfoil, shows an increase of $\frac{U_x}{U_\infty}$ of about 5% along the entire radius for the zero-yaw condition (Figure 5.16 (top)) and of about 10% for the 7.5° yaw angle (Figure 5.16 (bottom)). More interesting, the velocity reduction for the DonQi D5 model is less at yawed inflow than the baseline one. Finally, as expected, because of the yaw angle, the time-averaged velocity distribution is not symmetric. This can cause unsteady loads on the DWT system, thus increasing the possibility of earlier mechanical failures due to increased fatigue loads.

5.2.4. Aerodynamic performance

Table 5.2 summarizes the aerodynamic performance coefficients for the two DWT models calculated under both non-yawed and yawed inflow conditions. The duct thrust force coefficient C_{TD} , turbine thrust force coefficient $C_{T_{turbine}}$ and power coefficient C_P are shown. The values are obtained as time average over two complete turbine rotations after reaching temporal convergence.

The duct thrust force coefficient C_{TD} is defined in equation 5.1. The power coefficient C_P , expressed as a function of turbine thrust force coefficient $C_{T_{turbine}}$ and the azimuthally averaged surface integral of the axial velocity distribution U_x/U_∞ along the turbine's plane of rotation (from Figure 5.16), is given by:

$$C_P = \frac{P}{\frac{1}{2}\rho U_\infty^3 S_{turbine}} = C_{T_{turbine}} \oint_{S_{turbine}} \frac{U_x}{U_\infty}. \quad (5.3)$$

Chapter 3 concluded that for a given AD/turbine configuration, the C_P of a DWT can be increased if and only if C_{TD} is increased. Then, if C_{TD} increases, $C_{T_{turbine}}$ and ultimately C_P also increase, coherently to what is observed in Table 5.2. The comparison of the aerodynamic performance coefficients of the two DWT models in Table 5.2 shows that, for the same duct exit area, the DonQi D5 model outperforms DonQi[®] model, both in non-yawed and yawed inflow conditions. The performance improvement for the DonQi D5 model can be attributed to the duct profile camber, which enhances C_{TD} .

For the DonQi[®] model at $\alpha = 7.5^\circ$, C_{TD} returns a lower value in comparison to the C_{TD} at $\alpha = 0^\circ$. As a consequence, $C_{T_{turbine}}$ and C_P calculated at $\alpha = 7.5^\circ$ is lower by 13.5% and 16.4% respectively than that calculated at $\alpha = 0^\circ$. In contrast, for the DonQi D5 model, C_{TD} at $\alpha = 7.5^\circ$ is higher than that obtained at $\alpha = 0^\circ$. As explained before, this is because the duct camber delays duct wall separation on the suction side in yawed inflow conditions (see Figure 5.14 (right)), thereby increasing the C_{TD} as also noted in 2D simulations (see section 5.1). Then, the $C_{T_{turbine}}$ and C_P calculated at $\alpha = 7.5^\circ$ is higher by 4.4% and 3.2% respectively than that calculated at $\alpha = 0^\circ$ for the DonQi D5 model.

Table 5.2: Aerodynamic performance coefficients for the two DWT models.

	DonQi®		DonQi D5	
	0°	7.5°	0°	7.5°
C_{TD}	0.4238	0.3587	0.4812	0.5014
$C_{T_{turbine}}$	0.8292	0.7170	0.8417	0.8803
C_p	0.7545	0.6309	0.7675	0.7922

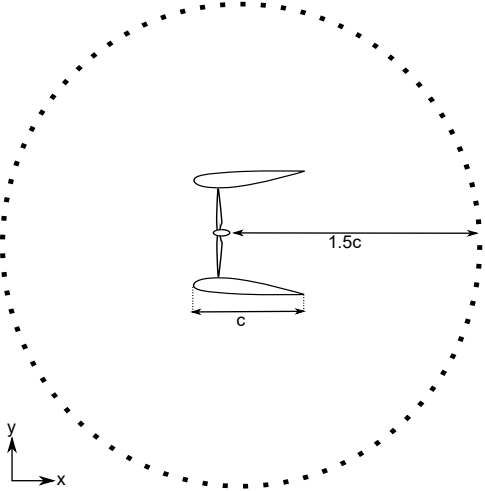


Figure 5.17: Schematic showing 72 microphones positioned at $1.5c$ from the center of the DWT and normal to the plane of turbine rotation

5.2.5. Noise estimation

The effect of the duct geometry and inflow conditions on the acoustic behavior of the two DWT models are investigated in this section. Noise is estimated on a circular array of 72 equally spaced microphones in the $x - y$ plane placed at $1.5c$ from the plane of rotation (Figure 5.17).

Figures 5.18 shows the Overall Sound Pressure Level (OASPL) expressed in decibel (dB) with reference pressure equal to 20×10^{-6} Pa. Results are integrated from 2 Hz to 392.4 Hz, i.e. up to 20 times the Blade Passing Frequency (BPF). It can be observed that the OASPL generated by the DonQi D5 model is higher than that of the DonQi® one, both in non-yawed and yawed inflow conditions. Starting with the non-yawed inflow (Figure 5.18 (top)), differences in the OASPL directivity patterns are observed; they are localized in certain flow directions, i.e. in the axial direction upstream of the DWT and at $\pm 120^\circ$. At these locations, the DonQi D5 model is approximately 15 dB and 20 dB louder than the baseline configuration. For the yawed inflow condition (Figure 5.18 (bottom)), the directivity patterns are almost similar to the zero-yaw angle case but tilted. However, the difference in OASPL between the two configurations is smaller than at zero yaw-angle case, i.e.

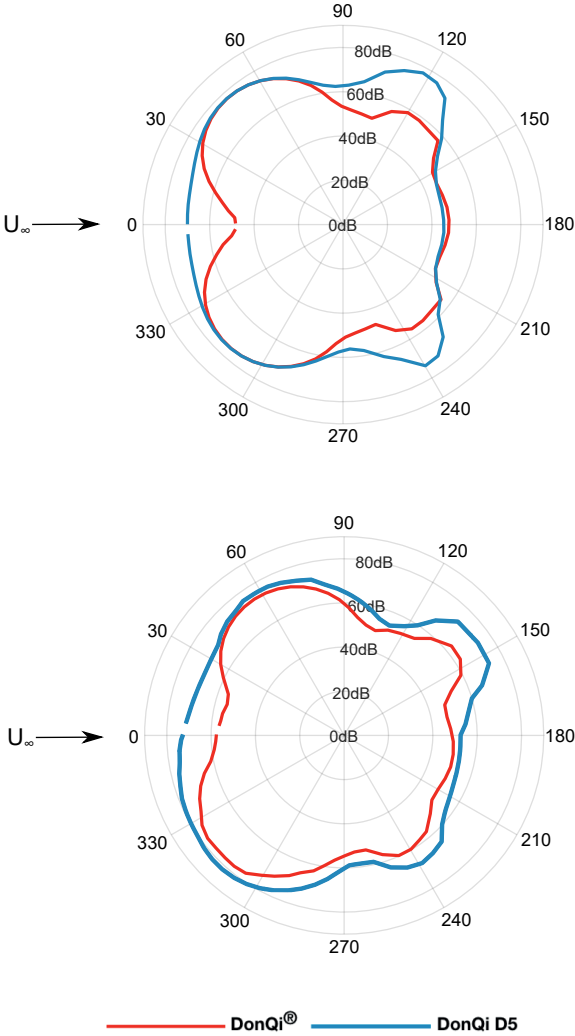


Figure 5.18: Overall Sound Pressure Level (OASPL) obtained for the two DWT models in (top) non-yawed inflow condition and (bottom) yawed inflow condition.

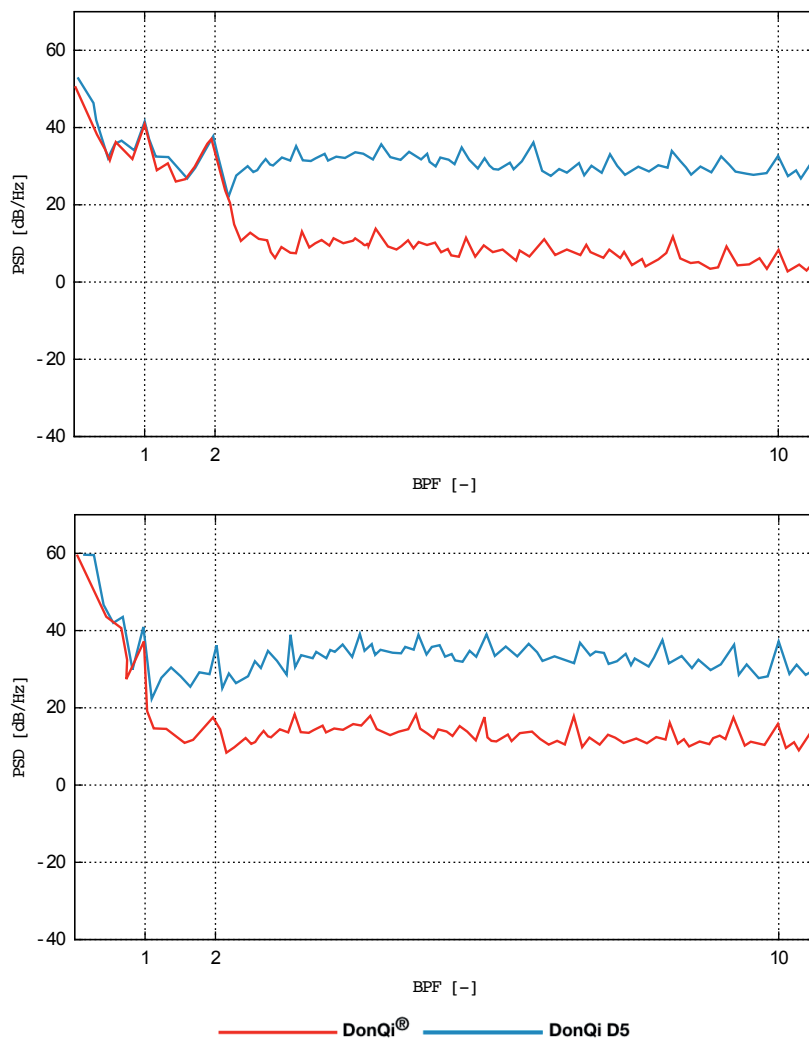


Figure 5.19: Power Spectral Density (PSD) versus the Blade Passing Frequency (BPF) for a microphone located at 90° under (top) non-yawed inflow condition and (bottom) yawed inflow condition.

the highly cambered duct is 8-10 dB louder than the baseline one.

The shape of the directivity plots for the DonQi D5 model, both in non-yawed and yawed inflow conditions, shows the appearance of larger lobes in the downstream direction in comparison to the baseline case. This can be associated to turbulent boundary layer trailing edge noise caused by the turbulent flow structures convecting along the outer surface of the duct [Brooks et al., 1989], as shown previously in Figures 5.11 and 5.12. Noise increase in the axial direction is instead related to the variation of the local boundary layer thickness at the turbine plane, and due to the presence of an additional noise source related to flow instabilities as found by Avallone et al. [2020].

To further explore the presence of an additional source of noise related to turbulent boundary layer trailing edge noise, Power Spectral Density (PSD) plots versus the blade Passing Frequency (BPF), expressed in dB/Hz, are shown for a microphone located at 90° with respect to the free-stream direction in Figure 5.19. For the non-yawed inflow condition (Figure 5.19 (top)), at frequencies higher than 2 BPF, the PSD curves diverges; the DonQi D5 model shows larger broadband noise with amplitude almost equal to the tonal peak at the 2nd BPF. For the yaw angle case (Figure 5.19 (bottom)), the PSD curves are almost identical up to the 1st BPF. Beyond this frequency, broadband noise dominates and becomes comparable to the tonal peak at the 1st BPF. The increase of the broadband noise component also for the baseline configuration at yaw angle confirms that the additional noise is related to turbulent boundary layer trailing edge noise.

5.3. Summary

In this work, the aerodynamic performance of DWT in yawed inflow condition is studied using a simplified duct-AD model. To this aim, first, two-dimensional numerical calculations using URANS simulations are shown. Based on the findings of chapter 3, two DWT models (DonQi[®] and DonQi D5) are chosen. The geometric parameters of the duct-AD models are identical, except for the duct geometry, which have different cross-section camber. To validate the numerical method, comparison of the numerical approach with the experimental data is reported. Of the two duct geometries investigated, DonQi D5 duct-AD model not only demonstrates an insensitivity to yaw but a gain in the overall performance C_p up to at a yaw angle $\alpha = 17.5^\circ$. On the contrary, C_p of DonQi[®] duct configuration drop for $\alpha > 0^\circ$. The C_p gain for the DonQi D5 duct-AD model with increasing α corresponds to the dimensionless duct thrust force coefficient C_{TD} , which increases due to the camber effect until the DWT stall angle is reached. More precisely, inner duct wall flow separation reduces the C_{TD} and ultimately the C_p of the DWT model.

Later, three-dimensional numerical calculations using Lattice-Boltzmann Very-Large-Eddy Simulations (LB-VLES) are carried out to investigate the aerodynamic and aeroacoustic performances of DWTs, both in non-yawed ($\alpha = 0^\circ$) and yawed ($\alpha = 7.5^\circ$) inflow conditions. Comparing the two DWT models, the power coefficient C_p for the DonQi D5 DWT model is approximately 1.7% and 20.4% higher than the DonQi[®] DWT model in non-yawed and yawed inflow conditions, respectively.

As concluded from the URANS calculations, DonQi D5 DWT model is less affected by the yaw inflow angle and a gain in the C_p by approximately 3% is obtained. The aerodynamic performance improvement, in terms of the turbine thrust force coefficient $C_{T_{turbine}}$ and C_p , for a DWT model corresponds to the increase of the duct thrust force coefficient C_{TD} . Flow visualization using velocity contours show that the highly cambered duct profile becomes beneficial for the mass-flow rate increase through the duct, both in non-yawed and yawed inflow conditions.

The duct shape has a strong effect on the noise. The overall sound pressure level (OASPL) is calculated at a circular array of microphones normal to the plane of rotation. The highly cambered configuration (DonQi D5 model) is approximately 10-15 dB louder than the baseline one (DonQi[®] model), both in non-yawed and yawed inflow conditions. Power spectral density (PSD) analysis shows that the broadband noise contribution becomes higher for the DonQi D5 model in comparison to the DonQi[®] model, both in non-yawed and yawed inflow conditions. The additional broadband noise source is due to turbulent boundary layer trailing edge noise due to the turbulent flow structures developing along the surface of the duct.

6

Conclusions



6.1	On the effects of the shape of the duct	103
6.2	On the effects of further augmentation techniques	104
6.3	On the effects of yawed inflow	104
6.4	Recommendations	104
6.5	Final thought	106

The best endings resonate because they echo a word, phrase, or image from earlier in the story, and the reader is prompted to think back to that reference and speculate on a deeper meaning.

James Plath

Computational Fluid Dynamic (CFD) methods described in chapter 2 have been applied in this thesis to study the aerodynamic and aeroacoustic aspects related to DWTs following the current state of the DWT research presented in chapter 1. The research questions placed in the beginning of this thesis were:

Does the concept of DWT in fact increase the power output, and if so, by how much; what geometric form should it take; and finally, how will DWT perform under yawed inflow conditions?

6

Following the story-line of the thesis, the major findings of this research have been grouped into three parts; namely, (1) to study the effects of the duct shape on DWTs aerodynamic performance, (2) to investigate on the augmentation techniques to further improve on the aerodynamic performance of DWT, and (3) to study the effects of yawed inflow condition on DWTs aerodynamic and aeroacoustic performance. Moreover, some recommendations for future research are given.

6.1. On the effects of the shape of the duct

- The aerodynamic mutual interactions between the duct and the turbine are nonlinear (section 3.3.1), which depend on the distinct shape of the duct and the turbine thrust force coefficient.
- The Lanchester-Betz-Joukowski limit, which defines the optimal turbine thrust force coefficient value to $8/9$ for the maximum power coefficient for horizontal axis wind turbines, is no longer applicable for DWTs; the optimal value depends on the duct thrust force coefficient (section 3.3.2).
- The aerodynamic performance of the DWT can be increased by increasing the duct cross-section camber and a correct choice of turbine thrust force coefficient, whilst maintaining the same duct-exit-area ratio (sections 3.3.1 and 3.3.2).

- An upper limit of the duct camber extent for the maximum power coefficient obtainable for DWT exists. Highly cambered duct profiles are prone to duct wall flow separation. The flow separation, when detected inside of the duct, reduces the duct thrust force coefficient and ultimately the power coefficient for the DWT model (section 3.4).

6.2. On the effects of further augmentation techniques

- The aerodynamic performance of an existing DWT model can be improved by using multi-element ducts. The improvement strongly depends on the installation setting of the secondary duct element with respect to the primary DWT geometry (section 4.1).
- A Gurney flap (retrofitted) at the trailing edge of the duct improves the aerodynamic performance of an existing DWT model by delaying inner duct wall flow separation, thus improving the mass flow rate at the turbine (section 4.2). The aerodynamic performance improvement, however, strongly depends on the Gurney Flap size and the existing DWT configuration.

6

6.3. On the effects of yawed inflow

- DWTs can demonstrate yaw insensitivity up to a specific yaw angle. The duct acts like the annular wing that sees the yaw angle as the increased angle of attack; the effect of which is that it increases the duct thrust force coefficient and ultimately the power coefficient for the DWT model until the stall angle of the duct is reached. The yaw insensitivity for the DWT model, however, strongly depends on the aerodynamic mutual interactions between the duct and turbine, which changes with the duct geometry, turbine configuration and yaw angle (section 5.1.2 and 5.2.4).
- The duct shape has a strong effect on the aeroacoustic performance of the DWT. An increase in duct cross-section camber increases the noise generated by the DWT model, both in non-yawed and yawed inflow conditions. The additional noise source is broadband in nature, which results from the turbulent flow structures convecting along the surface of the duct (section 5.2.5).

6.4. Recommendations

Like any other research, there are still many topics and open questions that can be recommended for future studies. The most prominent ones are listed here:

- It is recommended to not use ducts with a very large duct exit-area-ratio in order to improve the power production of DWTs. In doing so, the likelihood

of inner duct wall flow separation increases in real-world operating conditions, thus having a negative impact on the aerodynamic and aeroacoustic performance of DWTs. Note that, it is possible to challenge this recommendation by incorporating flow control devices, however, the performance benefits will be limited due to the cost of the complex system and its installation.

- In this work, the effects of the non-uniform blade loading on the aerodynamic and aeroacoustic performance of DWTs are studied using high-fidelity Very Large Eddy Simulation (VLES) model. These simulations require large computational resources. An actuator line CFD approach, which has been pursued extensively for the study of horizontal axis wind turbines, can be integrated into the computational study of DWTs to provide an initial assessment of the discrete blade effects.
- Despite having made significant advancements into the designs for DWTs, detailed studies investigating (i) the effects of tip gap size between the duct and the turbine blade and (ii) the effects of tip speed ratio on the wake development of DWTs are found to be missing in the existing literature. The tip gap would accelerate the flow via a mechanism similar to boundary layer blowing for airfoils [Avallone et al., 2020], while the tip speed ratio would influence the flow behavior inside of the duct. A detailed parametric study investigating these phenomenon would help improving the aerodynamic and aeroacoustic performance of DWTs.
- The wing-in-ground effect is well understood (see for example Rozhdestvensky [2000]), but never studied in relation to DWTs. DWT installation on building tops can take advantage of the ground effect, where the additional air pressure underneath the annular duct would increase the thrust force generated by the turbine.
- This thesis focuses on evaluating the performance of DWTs in low turbulence intensity flow. An investigation to study the influence of real-world turbulence levels on the aerodynamic and aeroacoustic performance of DWTs will be very useful.
- The DWT support structure, including the tower and the struts, underwent non-stationary vibrations while supporting the heavy duct during the experiments witnessed by the author. Mitigating these vibrations would not only improve the aerodynamic and aeroacoustic performance of DWTs, but also extend the life-cycle of the DWT components. This topic deserves to be investigated further.
- In order to be more commercially viable, the DWT designs should have cost competitiveness. A study highlighting the economic benefits of DWTs over other wind turbine designs would therefore be a logical next step.

6.5. Final thought

The clean energy revolution is booming. The renewable energy sources are displacing the dominance of fossil fuels in the energy market, thus lowering the carbon emissions and pollution levels. The question remains: *Can we put up enough renewable sources to generate the energy we need?* Taking this question into consideration, large amounts of research and finance are being channelled into growing the contribution of renewables. The sun, wind and sea might be free, but converting their power into electricity surely isn't. Of all the renewable sources, wind power is closer to being competitive to coal or gas. It can cost as low as six cents at the ideal onshore sites, but costs twice that offshore. In order to contribute towards the sustainable development goals, small wind turbines can be used for local power applications. Having said that, we will have to get over the NIMBY - *Not In My Backyard* syndrome. Small steps taken now can contribute in big ways towards the global mission of combating climate change. Installing small wind turbines would definitely require an investment, but if shared with neighbours - it could light three to four rooms or power the television for entertainment each night.



Figure 6.1: Artistic impression of Delft with roof-mounted ducted wind turbines. Artist: Marta Lorenzo Xoubanova.

References

- RJ Barthelmie and SC Pryor. Potential contribution of wind energy to climate change mitigation. *Nature Climate Change*, 4(8):684, 2014.
- E Dupont, R Koppelaar, and H Jeanmart. Global available wind energy with physical and energy return on investment constraints. *Applied Energy*, 209:322–338, 2018.
- A Fontaine, F Galmiche, and A Flament. Recommendations for implementation of long term markets (energy and capacity) 2020-2050. *report D6*, 3, 2016.
- MBT Fogaing, H Gordon, CF Lange, DH Wood, and BA Fleck. A review of wind energy resource assessment in the urban environment. In *Advances in Sustainable Energy*, pages 7–36. Springer, 2019.
- GJW van Bussel. The science of making more torque from wind: Diffuser experiments and theory revisited. *Journal of Physics: Conference Series*, 75(1):120–10, 2007.
- GM Lilley and WJ Rainbird. A preliminary report on the design and performance of ducted windmills. Technical report, College of Aeronautics Cranfield, 1956.
- A Kogan and E Nissim. *Design and performance of a shrouded windmill for power generation*. Technion-Israel Institute of Technology, Department of Aeronautical Engineering, 1962.
- A Kogan and A Seginer. *Shrouded Aerogenerator Design Study: II. Axisymmetrical Shroud Performance*. Technion-Israel Institute of Technology, Department of Aeronautical Engineering, 1963.
- O Igra. Shrouds for aerogenerators. *AIAA Journal*, 14(10):1481–1483, 1976.
- O Igra. Compact shrouds for wind turbines. *Energy conversion*, 16(4):149–157, 1977.
- O Igra. Research and development for shrouded wind turbines. *Energy Conversion and Management*, 21(1):13–48, 1981.
- BL Gilbert and KM Foreman. Experiments with a diffuser-augmented model wind turbine. *Journal of Energy Resources Technology*, 105(1):46–53, 1983.
- KM Foreman and BL Gilbert. Diffuser for augmenting a wind turbine, November 13 1984. US Patent 4482290A.

- DG Phillips, RGJ Flay, TA Nash, et al. Aerodynamic analysis and monitoring of the vortex 7 diffuser-augmented wind turbine. *Transactions of the Institution of Professional Engineers New Zealand: Electrical/Mechanical/Chemical Engineering Section*, 26(1):13, 1999.
- DG Phillips, PJ Richards, and RGJ Flay. Diffuser development for a diffuser augmented wind turbine using computational fluid dynamics. *Department of Mechanical, Engineering, the University of Auckland, New Zealand*, 2008.
- MOL Hansen, NN Sørensen, and RGJ Flay. Effect of placing a diffuser around a wind turbine. *Wind Energy: An International Journal for Progress and Applications in Wind Power Conversion Technology*, 3(4):207–213, 2000.
- O de Vries. Fluid dynamic aspects of wind energy conversion. Technical report, Advisory Group for Aerospace Research and Development NEUILLY-SUR-SEINE (France), 1979.
- Peter M Jamieson. Beating betz: energy extraction limits in a constrained flow field. *Journal of Solar Energy Engineering*, 131(3), 2009.
- S Widnall. Potential flow calculations of axisymmetric ducted wind turbines. *MIT*, 09(02):1–12, 2009.
- R Bontempo and M Manna. Solution of the flow over a non-uniform heavily loaded ducted actuator disk. *Journal of Fluid Mechanics*, 728:163–195, 2013.
- AC Aranake, VK Lakshminarayan, and K Duraisamy. Computational analysis of shrouded wind turbine configurations using a 3-dimensional rans solver. *Renewable Energy*, 75:818–832, 2015.
- TA Khamlaj and MP Rumpfkeil. Analysis and optimization of ducted wind turbines. *Energy*, 162:1234–1252, 2018.
- K Abe, M Nishida, A Sakurai, Y Ohya, H Kihara, E Wada, and K Sato. Experimental and numerical investigations of flow fields behind a small wind turbine with a flanged diffuser. *Journal of wind engineering and industrial aerodynamics*, 93(12):951–970, 2005.
- K Toshimitsu, K Nishikawa, W Haruki, S Oono, M Takao, and Y Ohya. Piv measurements of flows around the wind turbines with a flanged-diffuser shroud. *Journal of Thermal Science*, 17(4):375–380, 2008.
- J Tang, F Avallone, R Bontempo, GJW van Bussel, and M Manna. Experimental investigation on the effect of the duct geometrical parameters on the performance of a ducted wind turbine. In *Journal of Physics: Conference Series*, volume 1037, pages 22–34. IOP Publishing, 2018.
- K Abe and Y Ohya. An investigation of flow fields around flanged diffusers using cfd. *Journal of wind engineering and industrial aerodynamics*, 92(3–4):315–330, 2004.

- A Grant, C Johnstone, and N Kelly. Urban wind energy conversion: The potential of ducted turbines. *Renewable Energy*, 33(6):1157–1163, 2008.
- SH Wang and SH Chen. Blade number effect for a ducted wind turbine. *Journal of mechanical science and technology*, 22(10):1984–1992, 2008.
- CD Chaudhari, SA Waghmare, and AP Kotwal. Numerical analysis of venturi ducted horizontal axis wind turbine for efficient power generation. *International Journal of Mechanical Engineering and Computer Applications*, 1(5):90–93, 2013.
- R Bontempo, M Cardone, M Manna, and G Vorraro. Ducted propeller flow analysis by means of a generalized actuator disk model. *Energy Procedia*, 45:1107–1115, 2014.
- SAH Jafari and B Kosasih. Flow analysis of shrouded small wind turbine with a simple frustum diffuser with computational fluid dynamics simulations. *Journal of Wind Engineering and Industrial Aerodynamics*, 125:102–110, 2014.
- SZ Roshan, S Alimirzazadeh, and M Rad. RANS simulations of the stepped duct effect on the performance of ducted wind turbine. *Journal of Wind Engineering and Industrial Aerodynamics*, 145:270–279, 2015.
- GJW van Bussel. Duct4u - ducted wind turbine optimisation and utilisation. Technical report, Open Technology Programme - STW, 2015.
- KM Foreman and BL Gilbert. A free jet wind tunnel investigation of dawt models. *Grumman research and development Center Report to SERI, RE-668 (SERI/TR 01311-1)*, 1983.
- L Anselmi. Computational analysis of ducted wind turbines noise. *TU Delft Repository*, 32:12–49, 2017.
- F Avallone, D Ragni, and D Casalino. On the effect of the tip-clearance ratio on the aeroacoustics of a diffuser-augmented wind turbine. *Renewable Energy*, 152:1317–1327, 2020.
- YC Küçükösman. *Semi-analytical approaches for the prediction of the noise produced by ducted wind turbines*. PhD thesis, Delft University of Technology, 2019.
- B Kanya and K Visser. Experimental validation of a ducted wind turbine design strategy. *Wind Energy Science*, 3(2):919–928, 2018.
- A Betz. Das maximum der theoretisch möglichen ausnutzung des windes durch windmotoren. *Zeitschrift für das gesamte Turbinenwesen*, 20, 1920.
- WJM Rankine. On the mechanical principles of the action of propellers. *Transactions of the Institution of Naval Architects*, 6, 1865.
- RE Froude. On the part played in propulsion by differences of fluid pressure. *Trans. Inst. Naval Architects*, 30:390, 1889.

- GAM van Kuik. The lanchester–betz–joukowsky limit. *Wind Energy: An International Journal for Progress and Applications in Wind Power Conversion Technology*, 10 (3):289–291, 2007.
- H Glauert. *The analysis of experimental results in the windmill brake and vortex ring states of an airscrew*. HM Stationery Office, 1926.
- JD Anderson and J Wendt. *Computational fluid dynamics*, volume 206. Springer, 1995.
- GG Stokes. On the theories of the internal friction of fluids in motion, and of the equilibrium and motion of elastic solids. *Transactions of the Cambridge Philosophical Society*, 8, 1880.
- O de Vries. Fluid dynamic aspects of wind energy conversion. Technical report, Advisory Group for Aerospace Research and Development NEUILLY-SUR-SEINE (France), 1979.
- G De Oliveira Andrade. *Aerodynamic Perspectives on Wind Energy Efficiency*. PhD thesis, Delft University of Technology, 2019.
- EM Greitzer, CS Tan, and MB Graf. *Internal flow: concepts and applications*, volume 3. Cambridge University Press, 2007.
- O Reynolds. On the dynamical theory of incompressible viscous fluids and the determination of the criterion. In *Proceedings of the Royal Society-Mathematical and Physical Sciences*, volume 451, pages 5–47, 1895.
- SB Pope. Turbulent flows. *Reynolds-stress and related models*, 2001.
- DC Wilcox. *Turbulence modeling for CFD*, volume 2. DCW industries La Canada, CA, 1998.
- DD Apsley and MA Leschziner. Advanced turbulence modelling of separated flow in a diffuser. *Flow, Turbulence and Combustion*, 63(1-4):81, 2000.
- M Shives and C Crawford. Developing an empirical model for ducted tidal turbine performance using numerical simulation results. *Proceedings of the Institution of Mechanical Engineers, Part A: Journal of Power and Energy*, 226(1):112–125, 2012.
- ANSYS Fluent 18.0. Release 18.0, ansys. Inc., USA, November, 2018.
- Liangyu Zhao and Shuxing Yang. Influence of thickness variation on the flapping performance of symmetric naca airfoils in plunging motion. *Mathematical Problems in Engineering*, 2010, 2010.
- Chedhli Hafien and Talel Ben Mbarek. Reduced order model for the lift coefficient of an airfoil equipped with extrados and/or trailing edge flexible flaps. *Computers & Fluids*, 180:82–95, 2019.

- J Tang, F Avallone, and GJW van Bussel. Experimental study of flow field of an aerofoil shaped diffuser with a porous screen simulating the rotor. *International Journal of Computational Methods and Experimental Measurements*, 4(4):502–512, 2016.
- PK Kundu, IM Cohen, and HH Hu. Fluid mechanics. 2004. *Google Scholar*, pages 157–158, 2008.
- LF Richardson. *Weather prediction by numerical process*. Cambridge university press, 1992.
- S Chen and GD Doolen. Lattice boltzmann method for fluid flows. *Annual review of fluid mechanics*, 30(1):329–364, 1998a.
- S Succi. *The lattice Boltzmann equation: for fluid dynamics and beyond*. Oxford university press, 2001.
- R Courant, K Friedrichs, and H Lewy. On the partial difference equations of mathematical physics. *IBM Journal of Research and Development*, 11(2):215–234, 1967.
- CM Teixeira. Incorporating turbulence models into the lattice-boltzmann method. *International Journal of Modern Physics C*, 9(08):1159–1175, 1998.
- BE Launder and BI Sharma. Application of the energy-dissipation model of turbulence to the calculation of flow near a spinning disc. *Letters in heat and mass transfer*, 1(2):131–137, 1974.
- S Chen and GD Doolen. Lattice boltzmann method for fluid flows. *Annual review of fluid mechanics*, 30(1):329–364, 1998b.
- F Farassat and GP Succi. A review of propeller discrete frequency noise prediction technology with emphasis on two current methods for time domain calculations. *Journal of Sound and Vibration*, 71(3):399–419, 1980.
- N Curle. The influence of solid boundaries upon aerodynamic sound. *Proceedings of the Royal Society of London. Series A. Mathematical and Physical Sciences*, 231(1187):505–514, 1955.
- G Brès, F Pérot, and D Freed. A fflowcs williams-hawkings solver for lattice-boltzmann based computational aeroacoustics. In *16th AIAA/CEAS aeroacoustics conference*, page 3711, 2010.
- F Perot, MS Kim, and M Meskine. Nrel wind turbine aerodynamics validation and noise predictions using a lattice boltzmann method. In *18th AIAA/CEAS Aeroacoustics Conference (33rd AIAA Aeroacoustics Conference)*, page 2290, 2012.

- LEM Lignarolo, D Mehta, R Stevens, AE Yilmaz, G van Kuik, J Andersen, Søren, C Meneveau, CJ Ferreira, D Ragni, and J Meyers. Validation of four LES and a vortex model against stereo-PIV measurements in the near wake of an actuator disc and a wind turbine. *Renewable energy*, 94:510–523, 2016.
- RM Hicks and PA Henne. Wing design by numerical optimization. *Journal of Aircraft*, 15(7), 1977.
- H Sobieczky. Parametric airfoils and wings. *Notes on Numerical Fluid Mechanics, Vieweg Verlag*, 68:71–88, 1988.
- B Kulfan and J Bussioletti. Fundamental parameteric geometry representations for aircraft component shapes. *11th AIAA/ISSMO multidisciplinary analysis and optimization conference*, 15(6948), 2006.
- L Xiaoqiang, H Jun, S Lei, and L Jing. An improved geometric parameter airfoil parameterization method. *Aerospace Science and Technology*, 78, 2018.
- MK Brenda and JE Bussioletti. Fundamental parametric geometry representations for aircraft component shapes. In *11th AIAA/ISSMO Multidisciplinary Analysis and Optimization Conference*, number 2006-6948, 2006.
- MK Brenda. A universal parametric geometry representation method - cst. *45th AIAA Aerospace Sciences Meeting and Exhibit*, 2007.
- D Masters, NJ Taylor, T Rendall, C Allen, and D Poole. A geometric comparison of aerofoil shape parameterisation methods. *AIAA Journal*, 2017.
- G de Oliveira. Wind turbine airfoils with boundary layer suction, a novel design approach. *Msc Thesis, Delft University of Technology*, 2011.
- P Fuglsang, C Bak, M Gaunaa, and I Antoniou. Design and verification of the risob1 airfoil family for wind turbines. *Journal of Solar Energy Engineering*, 126: 1002–1010, 2004.
- VV Dighe, G de Oliveira, F Avallone, and GJW Van Bussel. On the effects of the shape of the duct for ducted wind turbines. In *2018 Wind Energy Symposium*, page 0997, 2018.
- JJ More. The levenberg-marquardt algorithm: implementation and theory. *Springer Lecture Notes in Mathematics*, 630:105–116, 1977.
- B Ernst, H Schmitt, and JR Seume. Effect of geometric uncertainties on the aerodynamic characteristic of offshore wind turbine blades. *Journal of Physics: Conference Series*, 555(012033), 2012.
- R Bontempo and M Manna. Effects of duct cross section camber and thickness on the performance of ducted propulsion systems for aeronautical applications. *International Journal of Aerospace Engineering*, 16, 2016.

- P Ten Hoopen. An experimental and computational investigation of a diffuser augmented wind turbine. *TU Delft Repository*, 32:22–67, 2009.
- J Jeong and F Hussain. On the identification of a vortex. *Journal of fluid mechanics*, 285:69–94, 1995.
- AHM Kwong and AP Dowling. Active boundary-layer control in diffusers. *AIAA journal*, 32(12):2409–2414, 1994.
- Á Jiménez, A Crespo, and E Migoya. Application of a les technique to characterize the wake deflection of a wind turbine in yaw. *Wind energy*, 13(6):559–572, 2010.
- TF Brooks, D S Pope, and MA Marcolini. Airfoil self-noise and prediction. *National Aeronautics and Space Administration report*, 16, 1989.
- KV Rozhdestvensky. *Aerodynamics of a lifting system in extreme ground effect*. Springer Science & Business Media, 2000.
- L Boltzmann. *Lectures on gas theory*. Courier Corporation, 2012.
- PL Bhatnagar, EP Gross, and M Krook. A model for collision processes in gases. i. small amplitude processes in charged and neutral one-component systems. *Physical review*, 94(3):511, 1954.

Appendix A

Derivation of Navier Stokes from Lattice Boltzmann equations

Lattice Boltzmann method (LBM) originated from the lattice gas automata (LGA) or lattice gas cellular automata (LGCA), which can be considered as a simplified molecular dynamics model to simulate the behavior and interaction of individual particles in a fluid system. The method uses ensemble averaging, the so called particle distribution function. In two-dimensional space, each lattice node move from their current node to the neighboring node in the direction of the velocity vector. If two particles meet head on in a node, as in Figure 2.10, their outgoing velocities are changed from their incoming velocities.

Starting with the particle distribution function $f(\chi, U, t)$, which is a function of physical space χ , velocity space U and time t . The total derivative of $f(\chi, U, t)$ with respect to t yields:

$$\frac{Df}{Dt} = \left(\frac{df}{d\chi}\right)\frac{d\chi}{dt} + \left(\frac{df}{dU}\right)\frac{dU}{dt} + \left(\frac{df}{dt}\right)\frac{dt}{dt}. \quad (\text{A1})$$

Alternatively, $\frac{d\chi}{dt}$ can be expressed as the particle velocity U . $\frac{dU}{dt}$ is the acceleration, which by Newton's second law is written as the body force density $\frac{dU}{dt} = \frac{F}{\rho}$. Having said that, equation A1 is rewritten as:

$$\frac{Df}{Dt} = \left(\frac{df}{d\chi}\right)U + \left(\frac{df}{dU}\right)\frac{F}{\rho} + \frac{df}{dt}. \quad (\text{A2})$$

If the left hand side of equation A2 returns zero, the equation becomes a sort of advection¹ equation, describing collision-less propagation of $f(\chi, U, t)$. Since, collisions between two particles happen at the same χ , U and t , $\frac{Df}{Dt}$ as the collision operator Ω can be written as:

Boltzmann equation

$$\Omega(f) = U \cdot \nabla f + \frac{F}{\rho} \cdot \nabla_U f + \frac{df}{dt}. \quad (\text{A3})$$

Equation A3 is called the Boltzmann equation after Boltzmann [2012], who devised it in the late 19th century. Three conditions are conserved in a collision:

¹In fluid dynamics, advection is the transport of a substance by the velocity of the fluid.

$$\text{Mass conservation : } \int \Omega(f) dU = 0, \quad (\text{A4})$$

$$\text{Momentum conservation : } \int U \Omega(f) dU = 0, \quad (\text{A5})$$

$$\text{Energy conservation : } \int |U|^2 \Omega(f) dU = 0, \quad (\text{A6})$$

The collision operator proposed by [Bhatnagar, Gross, and Krook \[1954\]](#) is applied. The BGK operator captures the collision behavior by directly modelling the relaxation process instead of tracking the details of collisions.

$$\Omega = -\frac{1}{\iota} \left(f - f^0 \right), \quad (\text{A7})$$

where ι is called the relaxation time and f^0 is the particle distribution function in equilibrium state. The BGK operator can be shown to satisfy conservation of mass, momentum, and energy [[Chen and Doolen, 1998a](#)].

By taking the appropriate moments of the Boltzmann equation [A3](#), conservation equations of continuity, momentum and energy for the three collision invariants can be found. For notational convenience, it is imperative to define the moment tensors of f :

$$\begin{aligned} \Pi_0 &= \int f dU = \rho, & \Pi_x &= \int U_x f dU = \rho u, \\ \Pi_{xy} &= \int U_x U_y f dU, & \Pi_{xyz} &= \int U_x U_y U_z f dU, \end{aligned} \quad (\text{A8})$$

and so forth. For convenience, the moments of $\frac{df}{dU_x}$ using multidimensional integration by parts can be given by:

$$\int \frac{df}{dU_x} dU = 0 \quad \& \quad \int U_x \frac{df}{dU_x} dU = - \int \frac{dU_x}{dU_y} f dU = -\rho dxy. \quad (\text{A9})$$

Taking the zeroth moment of all the terms in the Boltzmann equation [A3](#) using spatial coordinate for velocity U_x , returns:

$$\int \Omega(f) dU = \frac{d}{dx} \int f U_x dU + \frac{F}{\rho} \int \frac{df}{dU_x} dU + \frac{d}{dt} \int f dU, \quad (\text{A10})$$

where $\int f(\chi, U, t) dU$ is the spatial density $\rho(\chi, t)$ of the particle and $\int f(\chi, U, t) U_x dU$ is the momentum density $\rho U(\chi, t)$ of the particle within a given velocity range. Having said that, and inserting equations [A4](#) and [A8](#) in equation [A10](#), the zeroth moment of Boltzmann equation becomes:

Continuity equation

$$\frac{d\rho}{dt} + \rho \frac{dU_x}{d\chi_x} = 0, \quad (\text{A11})$$

which is identical to the equation 2.27, but written in differential form.

Taking the first moment of the Boltzmann equation A3 and using similar assumptions as for the zeroth moment, returns:

$$\int U_x \Omega(f) dU = \frac{d}{dx} \int U_x U_y f dU + \frac{F}{\rho} \int U_x \frac{df}{dU_y} dU + \frac{d}{dt} \int U_x f dU. \quad (A12)$$

Using equations A5, A8 and A9, the first moment of the Boltzmann equation A12 becomes:

$$\frac{d\rho U_x}{dt} + \frac{d\Pi_{xy}}{d\chi_y} = F_x. \quad (A13)$$

$\Pi_{xy} = \int U_x U_y f dU$ can be interpreted as the flow in the x direction with the momentum component in the y direction. It can be resolved into two parts using $U_x U_y = (U_x + U'_x)(U_y + U'_y)$, where U' indicates the fluctuating velocity component. The fact that moments of U' are zero, leads to:

$$\Pi_{xy} = \int (U_x U_y + U_x U'_y + U'_x U_y + U'_x U'_y) f dU = \rho U_x U_y - \sigma_{xy}, \quad (A14)$$

where $\rho U_x U_y$ represents the macroscopic flow of momentum and

$$\sigma_{xy} = - \int U'_x U'_y f dU, \quad (A15)$$

can be identified as the Cauchy stress tensor, which defines the state of stress at any point in the fluid particle. Thus, the first moment of the Boltzmann equation A3 returns:

Momentum equation

$$\frac{d\rho U_x}{dt} = - \frac{d\rho U_x U_y}{d\chi_y} + \frac{d\sigma_{xy}}{d\chi_y} + F_x, \quad (A16)$$

which is identical to the equation 2.28, but written in differential form.

Appendix B

Variables for aeroacoustic calculations

Sound waves or acoustic waves can be defined as fluctuations build up from pressure, velocity and/or density in a compressible fluid, which can travel in all direction. In the context of this research, the local pressure deviation, further denoted as sound pressure, is measured using a microphone array. The sound intensity (W/m^2), i.e. the energy flux transmitted per unit area by the propagation of sound, is given by:

$$I = p_a u_a. \quad (A22)$$

The sign of the intensity depends on the direction of sound propagation. The sound intensity is related to the pressure through its specific acoustic impedance $\rho_0 c_0$. The sound intensity for pure plane harmonic waves can be re-written as:

$$I = \frac{p_e^2}{\rho_0 c_0}, \quad (A23)$$

where, p_e is the effective amplitude, i.e. the root-mean-square of p_a . To extract the sound power P (W) from a given source, the intensity is integrated over the surface area S with the direction vector outward normal n as:

$$P = \int_S I \cdot n dS. \quad (A24)$$

It is difficult to plot this parameter due to wide range of pressure variations; for e.g. very soft sounds near the threshold of hearing until the deafening of hearing. Since the difference can be several orders of magnitude, a logarithmic scale expressed in decibel (dB) is used to define the Sound Pressure Level (SPL), given by:

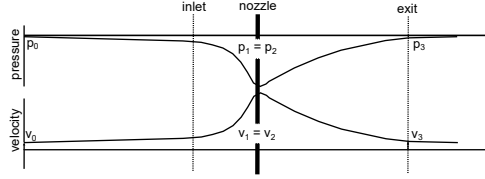
$$SPL = 20 \log_{10} \left(\frac{p_e}{p_{ref}} \right), \quad (A25)$$

where $p_{ref} = 20 \mu Pa$ corresponding to the threshold of human hearing. SPL is usually defined per chosen frequency band, for e.g. one-third octave or one-tenth decade bands. The Overall Sound Pressure Level (OASPL) is effectively an integration of all bands contained in the sound spectrum.

A Power Spectral Density (PSD) shows the strength of the energy variation as a function of frequency, expressed in dB/Hz . It is computed from the time diagram of the pressure variations over its frequency range by using the well known Fast Fourier Transform (FFT).

Appendix C

r_{max} calculation using axial momentum theory



Pressure and velocity relations in a DWT using AMT

Based on the geometry under consideration, the duct expansion ratio $\beta = 2.25$ is established and the the AD inside the duct operates at $a = \frac{1}{3}$. $V_0 = 6$ m/s corresponding to the numerical study reported above. Having said that, the velocity at the duct exit equals:

$$V_3 = (1 - a)V_0 = 4 \text{ m/s.} \quad (\text{A17})$$

Using the diffuser area ratio β , the velocity at the AD location equals:

$$V_1 = \beta(1 - a)V_0 = 9 \text{ m/s,} \quad (\text{A18})$$

and the value of back pressure velocity ratio γ yields:

$$\gamma = \frac{V_3}{V_0} = 0.67. \quad (\text{A19})$$

Finally, the power coefficient considering AD surface area returns:

$$C_P = \beta \gamma \frac{16}{27} = 0.89, \quad (\text{A20})$$

where $\frac{16}{27}$ is the theoretical limit for maximum achievable performance for a bare wind turbine, most commonly addressed as the Betz limit. Then, the maximum power augmentation factor r_{max} equals:

$$r_{max} = \frac{C_P}{C_{P_{Betz}}} = 1.50. \quad (\text{A21})$$

Curriculum Vitae



Vinit Dighe was born on 6 November 1990 and grew up in Mumbai, India. He had an amazing childhood with his parents and his grandma, who were super supportive and encouraged him to pursue his dreams. He attended the following institutions before starting his PhD in 2015:

2009–2011	Diploma in Aircraft Maintenance Engineering Mumbai, India
2011–2013	B.Eng (Honours) Aerospace Systems Engineering Coventry University, England
Thesis Supervisors	Investigations into the aeronautical designs of Frederick Lanchester Dr. Caroline Lambert and Chris Clark
2014–2015	M.Res (Honours) Engineering Science The University of Auckland, New Zealand
Thesis Supervisor	Modelling smart wind turbine blades Dr. John Cater

Vinit loves to explore new places and different cultures. He spends his free time exercising and competes in triathlon races. In January 2020, Vinit started working at CWI Amsterdam, where he investigates the subject of uncertainty quantification and calibration of aeroelastic wind turbine models.

List of Publications

Journal articles

- **V. V. Dighe.**, Avallone, F., and van Bussel, G.J.W. *Effects of yawed inflow on the aerodynamic and aeroacoustic performance of ducted wind turbines*. Journal of Wind Engineering and Industrial Aerodynamics, 2020.
- **V. V. Dighe.**, Suri. D., Avallone, F., and van Bussel, G.J.W. *Ducted wind turbines in yawed flow: A numerical study*. Wind Energy Science (submitted).
- **V. V. Dighe.**, de Oliveira, G., Avallone, F., and van Bussel, G.J.W. *Characterization of aerodynamic performance of ducted wind turbines: A numerical study*. Wind Energy, 2019.
- **V. V. Dighe.**, Avallone, F., Igra, O., and van Bussel, G.J.W. *Multi-element ducts for ducted wind turbines: a numerical study*. Wind Energy Science 4.3: 439-449, 2019.
- **V. V. Dighe.**, de Oliveira, G., Avallone, F., and van Bussel, G.J.W. *Towards improving the aerodynamic performance of a ducted wind turbine: A numerical study*. Journal of Physics: Conference Series. Vol. 1037. No. 2. IOP Publishing, 2018.
- S, Overeem., L. Alen., Y. Brouwer., A. Dam., G. Dekken., G. Garrett., S. Geboers., J. Poland., H. Aldridge., **V. V. Dighe.**, and N.C. Antsos. *Wind assessment for micro wind turbines in an urban environment*. International Journal of Energy Production and Management 2.4:327-338, 2016
- **V. V. Dighe.**, F. Avallone, and G. J. W. van Bussel. *Computational study of diffuser augmented wind turbine using actuator disc force method*. International Journal of Computational Methods and Experimental Measurements 4.4:522-531, 2016.

Conference proceedings

- **V. V. Dighe.**, Suri, D., Avallone, F., and van Bussel, G.J.W. *How does yawed inflow affect the performance of ducted wind turbines?* 38th Wind Energy Symposium - AIAA Scitech, 2020.
- **V. V. Dighe.**, de Oliveira, G., Avallone, F., and van Bussel, G.J.W. *On the effects of the shape of the duct for ducted wind turbines*. 36th Wind Energy Symposium - AIAA Scitech, 2018.

- **V. V. Dighe.**, Yu, W., and van Bussel, G.J.W. *Benchmark prediction of the actuator disc experiment using the CFD code Fluent*. 13th EAWC PhD Seminar, 2017.
- **V. V. Dighe.**, Tang, J., Avallone, F., and van Bussel, G.J.W. *Effects of Gurney Flaps on the Performance of Diffuser Augmented Wind Turbine*. 35th Wind Energy Symposium - AIAA Scitech, 2017.
- **V. V. Dighe.**, and J. E. Cater. *Numerical investigation of distributed trailing edge suction for wind turbine aerofoils using CFD*. 17th Australasian Wind Engineering Society Workshop, 2015.

Other

- Sammy, J., **V. V. Dighe.**, and Desai, S. *Carbix Corp*. Accelerator grant, Spring 2020 (SOSV-Indiebio).
- **V. V. Dighe.** *Let's duct the wind!* Hague Innovators Challenge, 2020 (In top 3 finalists).
- **V. V. Dighe.**, Avallone, F., and G. J. W. van Bussel. *Ducted wind turbines in urban environment*. Demonstration at TU Delft, 2019 (First prize awarded).
- **V. V. Dighe.**, Avallone, F., and G. J. W. van Bussel. *Increase drag for improved performance: A ducted wind turbine study*. Poster presentation at TU Delft PhD Seminar, 2018.
- **V. V. Dighe.** *Ducted wind turbines: A potential energy shaper*. VSV Leonardo Times, 2016.
- **V. V. Dighe.**, and G. J. W. van Bussel. *Computational study of diffuser augmented wind turbine using actuator disc force method*. Poster presentation at EAWC PhD Seminar, 2016.
- **V. V. Dighe.**, N.C. Antsos., and J. Tang. *Investigation into ducted wind turbines for urban environment*. Oral presentation at 7th Small Wind Summit, Husum, Germany, 2016.
- **V. V. Dighe.**, and J. Cater. *Modelling smart wind turbine blades*. Oral presentation at FINZ 2015, New Zealand, 2015.

Acknowledgements

My doctoral work definitely results from the collective effort of people and places that have supported and influenced my journey. I wish to thank:

- For the PhD research...
 - Gerard van Bussel, my promoter and supervisor, for offering me a chance to pursue doctoral research at TU Delft. This journey would have not been so much enlightening without your unprecedented academic freedom. It is amazing to receive guidance from someone who has spent so much time and understands so much about the evolution of DWT concept, over its first decades. Your high-spirited personality made our conference travels and dinners so much fun.
 - Francesco Avallone, who acted as daily supervisor, led me through this research with his exceptional scientific skills and unimpeachable work ethics. All I can say, I would not have made it to the end of this PhD, had you not been around to convert my research questions to 'our' research questions.
 - Dhruv Suri, I think getting the overabundant number of things in place during your research visit would have been utterly impossible without your enthusiasm. Remember, you are cut out for something big!
 - Juan Tang for reinforcing my simulation results with your experiments. Those wind tunnel hours, conference travels, and of-course the sports session with you will be treasured.
 - Gael De Oliveira for the steady-state vortex code. Without your help and the numerous brainstorming sessions, this work would have been back breaking.
 - Ozer Igra for providing me with experimental data, support with paper revisions and the nice email conversations.
 - The students I worked with: Simon, Louis, Yair, Andre, Glenn, Geoffrey, Sven, Jelle and Harry. I wish you all a great future.
 - Nikolaos Chrysochoidis-Antsos for striking the right chord in the Duct4U project. Remember my friend, we did manage to light the bulb.
 - Sylvia Willems for providing all that is needed for a good research environment, helping me organise my travels, nice conversations and for being so terrifically efficient.

- Colleagues at TU Delft...
 - Sebastian Sanchez, it is wonderful to have a friend like you around talking work, life and beyond.
 - Carlos Baptista and Mikko for being such nice office-mates. Thanks for keeping the hubbub of CFD alive in our office.
 - Christopher for helping me whenever I had questions on aeroacoustics. Also, the questions you threw at us during our lunch hour kept the brains churning.
 - Lunch and card gang: Sebastian R., Julia, Mark, Bedassa, Ashwin, Navneeth, Zi and Mihir for the lunch-time conversations and the card game tradition.
 - Dyna-night boys: Rene, Daniel, Sebastian, Ashim and Bruce for the beers and the conversations we knocked.
 - Delphine, Tom, Wei, Daniele, Livia, Jaco, Laurent, Jing, Yunusi, Chihoon, Sharif, Edoardo, Ming, Jingna, Carlos Simao Ferreira, Simon, Wim, Michiel and Erik for the nice interactions we had. I wish you all a life full of happiness and surprises.
- Outside office...
 - It would have been impossible to complete this PhD without the distraction and all the crazy moments shared with Bharat, Nitish and Akash; let's continue being this way.
 - All the friends I made during my PhD years. Special thanks go to my friends Marta, Karinoa and León; I truly value the time that we spent.
 - Astrid and Ronald for all the beautiful moments and the smiles that we shared together.
 - The Netherlands, for being a home away from home. You gave me amazing bike routes to ride on and variety of cheese to hog on.
 - India, for all the excitement, noise and diversity that I haven't found elsewhere.
- The pillars of my life...
 - Lotte for all the magical moments that we spent together and for always showing how proud you are of me. Let's write more beautiful life chapters together.
 - My parents, Vini and Vijay for their infinite love and infinite support throughout my life; words fail me to thank you enough.
 - The last word goes to my AaJi, who has been the light of my life always. This thesis is dedicated to you.



ISBN 978-94-6380-816-3



978-94-6380-816-3